


FACULTY
OF MATHEMATICS
AND PHYSICS
Charles University

**DOCTORAL THESIS**

Burak Aygün

# Modeling tidal deformation of planetary bodies with subsurface oceans

Department of Geophysics

Supervisor of the doctoral thesis: Prof. RNDr. Ondřej Čadek, CSc.
Study programme: Physics
Study branch: Physics of the Earth and Planets

Prague 2025

I declare that I carried out this doctoral thesis independently, and only with the cited sources, literature and other professional sources. It has not been used to obtain another or the same degree.

I understand that my work relates to the rights and obligations under the Act No. 121/2000 Sb., the Copyright Act, as amended, in particular the fact that the Charles University has the right to conclude a license agreement on the use of this work as a school work pursuant to Section 60 subsection 1 of the Copyright Act.

In ..... date .....  .....

Author's signature

I would like to express my deepest gratitude to Ondřej Čadek for his invaluable guidance and support throughout my doctoral studies. His insights have shaped my research and greatly contributed to my development as a scientist.

I am also thankful to Gabriel Tobie and Gaël Choblet for hosting me in Nantes during my short-term stay under the Barrande Fellowship Programme. I appreciate our scientific discussions and the collaborative project presented in the final chapter of this thesis.

I am grateful to my office mates, Martin and Jakub K., for the endless scientific conversations and unwavering moral support—even in an office with temperatures that remind me of my home.

Many thanks to Hana Čížková, Marie Běhounková, Jiří Zahradník, Ondřej Souček, Vojtěch Patočka, Jakub Pokorný, František Čejka, Jan Premus, and everyone in the Department of Geophysics for creating such a friendly, vibrant, and supportive environment.

I want to give special thanks to my dearest Kristýna and Oxik for enduring and supporting me during the final stages of this journey. Perhaps the deepest thanks go to my parents for supporting me unconditionally, even from thousands of kilometers away.

This research was supported by the Charles University projects SVV 260709, SVV 260581, the Czech Science Foundation project No. 25-16801S, and the Barrande Fellowship programme.

Title: Modeling tidal deformation of planetary bodies with subsurface oceans

Author: Burak Aygün

Department: Department of Geophysics

Supervisor: Prof. RNDr. Ondřej Čadek, CSc., Department of Geophysics

Abstract: The Jovian and Saturnian systems are home to intriguing satellites from volcanically active Io to icy moons with subsurface oceans, such as Enceladus, Titan, Europa, and Ganymede. Since the late 60s, our understanding of these moons has immensely improved by data from the missions like Voyager, Galileo, Cassini-Huygens, and Juno. These missions have revealed that these moons exhibit complex internal dynamics and surface features, with some of the icy moons showing potential to sustain a habitable environment. A key tool for probing their internal structure is modeling tidal response. However, existing models often rely on solid-body tide theory (neglecting ocean dynamics), two-dimensional tidal flow models, or simplified three-dimensional incompressible frameworks. This thesis introduces a novel time-domain approach that couples solid deformation with oceanic flow in a compressible, multilayered planetary body. Our results highlight the limitations of 2D shallow-water models, which are only valid for thin oceans. By applying our model to Enceladus and Io, we demonstrate how tidal dynamics are shaped by ocean thickness, viscosity, and the coupling between solid and liquid layers. In the case of Io, we show that a thin viscous magma ocean can significantly enhance the tidal response. However, the observed Love number from Juno suggests that such an ocean is unlikely to exist near the surface, though a deep magma layer remains a possibility. Looking ahead to ESA's Juice mission, which will explore Ganymede with unprecedented precision, our work underscores the need to incorporate the full complexity of tidal dynamics. Our results show that including compressibility in the tidal response can shift the ice shell thickness estimates by 20-30 km. Although the dynamics of the ocean may have a modest effect, their influence can be detectable by the Juice/3GM experiment, offering additional constraints on Ganymede's internal structure.

Keywords: tidal response, icy moons, Galilean moons, numerical modeling, subsurface oceans

# Contents

**Introduction** **3**

**1 Tidal response of a planetary body** **7**
1.1 Characteristics of the tidal response . . . . . 7
1.2 Internal structure of the moons of the outer Solar System . . . . . 10
1.3 Tidal response of subsurface oceans: Shallow water approximation 15

**2 A three-dimensional approach to tidal response of a subsurface ocean** **19**
2.1 Governing equations of Oceanus . . . . . 19
2.2 Numerical implementation . . . . . 22

**3 Impact of the core deformation on the tidal heating and flow in Enceladus' subsurface ocean** **31**
3.1 Introduction . . . . . 31
3.2 Method . . . . . 34
3.3 Tidal Dissipation in the Ocean and the Core . . . . . 38
3.4 Velocity Field in the Ocean . . . . . 41
3.5 Comparison with the LTE approach . . . . . 44
3.6 Conclusion . . . . . 47

**4 Tidal heating in a subsurface magma ocean on Io revisited** **51**
4.1 Introduction . . . . . 51
4.2 Method . . . . . 52
4.3 Results . . . . . 54
4.4 Discussion and conclusions . . . . . 58

**5 Love numbers for Io with a magma ocean** **61**
5.1 Introduction . . . . . 61
5.2 Method . . . . . 63
5.3 Results . . . . . 65
5.4 Conclusions . . . . . 68

**6 Compressible Love numbers of Ganymede** **71**
6.1 Introduction . . . . . 71
6.2 Method . . . . . 72
6.3 Results . . . . . 73
6.4 Discussion and Conclusion . . . . . 75

**Conclusion** **77**

**Bibliography** **81**

**List of publications** **97**

**A Appendix** **99**
A.1 Spherical harmonics . . . . . 99
A.2 Mathematical operations in the spectral domain . . . . . 99
A.3 Governing equations in the spectral domain . . . . . 101

**B Appendix** **103**
B.1 Supporting information for Chapter 3 . . . . . 103
B.2 Supporting information of Chapter 4 . . . . . 104

# Introduction

The mysteries of the outer Solar System have been continuously revealed since the close-up observations by the Voyager missions, followed by the Galileo and Cassini-Huygens missions. The formation of gas giants beyond the snow line is closely linked to the simultaneous development of icy satellites of varying sizes and masses (Figure 1). Observations of Voyager 1 and 2 led to groundbreaking discoveries about both Jovian and Saturnian systems during their flybys in the late 1970s and the 1980s. These observations revealed the diversity and complexity of the moons of the gas giants. Their diameter ranges from hundreds of kilometers to thousands of kilometers, and they exhibit complex tectonic features indicating either current or past geological activity. These observations include, among

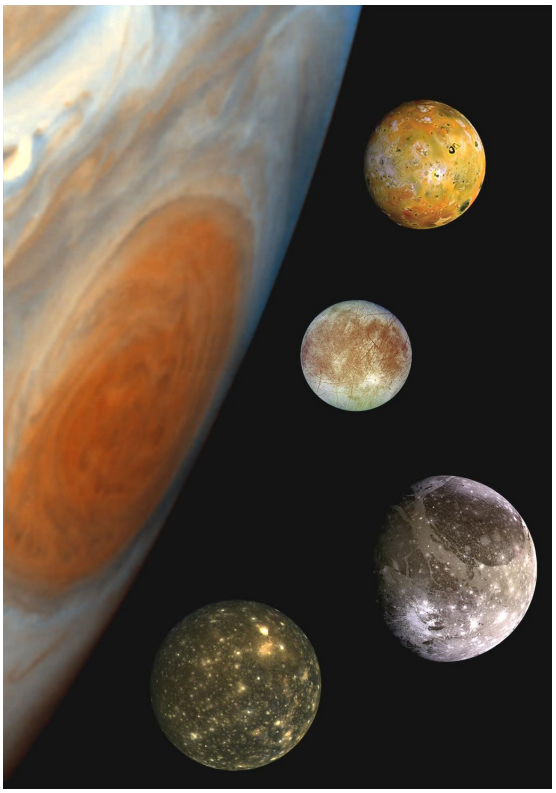


Figure 1: Artistic representation of the Galilean moons. Jupiter on the left, and top to bottom: Io, Europa, Ganymede, and Callisto (Image credit: NASA/JPL/DLR).

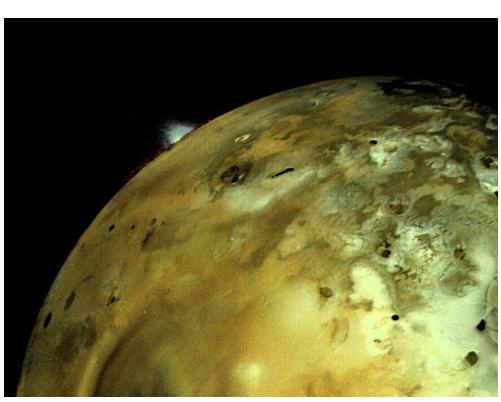
many more, the intense volcanic activity on Io (Figure 2a)(Matson et al., 1981), the complex surface features of Europa and Ganymede (Pappalardo et al., 1998; Squyres et al., 1983), the dense atmosphere covering Titan (Lunine et al., 1989), and a bright surface of Enceladus (Kargel and Pozio, 1996). The exploration of the Jovian system is followed by the Galileo mission (1996–2003). Within its lifetime, the Galileo mission helped map the hot spots and volcanoes of Io (McEwen et al., 1998; Keszthelyi et al., 2001), detected the chaos terrains, faulting, and an induced magnetic field on Europa, supporting the subsurface ocean hypothesis (Khurana et al., 1998). For Ganymede, the mission discovered its intrinsic magnetic field (Kivelson et al., 1996) and provided observations that indicated

the presence of a subsurface ocean through magnetic and gravity data (Kivelson et al., 2002). As the Galileo mission was coming to an end, the Cassini-Huygens (2004–2017) mission was set on a journey to the Saturnian system. During its orbit around Saturn, its observations mapped lakes and rivers of methane on Titan (Stofan et al., 2007). One of the major outcomes of the Cassini mission was the prediction of the potential Love number of Titan, which suggested the possible existence of a subsurface ocean (Iess et al., 2012). As for the tiny moon of Saturn, Enceladus, the Cassini mission provided direct evidence of a liquid layer beneath the south polar region by analyzing the burst of material coming out of its tiger stripes (Porco et al., 2006). Going back to the Jovian system, flybys of the Juno mission (2016–present) provided additional images of Ganymede (Ravine et al., 2022) and constraints on its gravitational moments (Gomez Casajus et al., 2022). More importantly, the latest flybys of Io led to estimations of the tidal potential Love numbers and imposed significant constraints on Io's interiors (Park et al., 2024a). All these, and many more, observations revealed crucial information on the Jovian and Saturnian systems. While our understanding of these systems has been considerably improved, the discoveries by the space missions have brought many more questions yet to be answered.

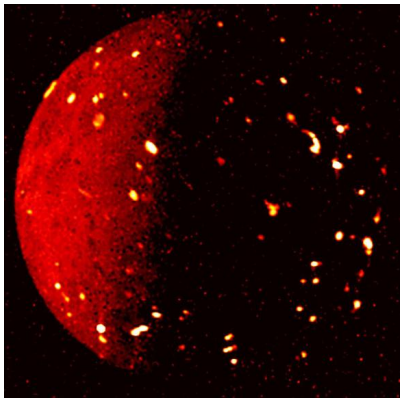
Tidal forces play a foundational role in understanding the thermal and orbital evolution, geological processes, and potential habitability of planetary bodies. They arise from the gravitational interactions between a satellite and its central body. In the simplest scenario, where the satellite has a circular orbit and is in a 1:1 spin-orbit resonance, tidal forces remain relatively constant. However, the actual dynamics are often more complex, where, for example, moons in the Jovian and Saturnian systems have eccentric orbits, resulting in time-varying tidal forces that continually deform these bodies. In addition to the eccentricity tides, the complexity of the gravitational interactions is increased by the moons' mutual interactions. The eccentricities of the three Galilean moons – Io, Europa, and Ganymede – (Figure 1) have evolved through mutual and Jupiter's gravitational interactions (Hussmann and Spohn, 2004). As they have reached the Laplace resonance, their orbital periods are close to the ratio of 1:2:4, and their eccentricities can be maintained over long periods of time. The tidal forces on Io are the primary driver for its intense volcanic activity (Peale et al., 1979), with heat output reaching up to 100 TW (Veeder et al., 1994). While Io has been a highly dissipative and volcanically active moon, its interactions with Europa have led to eccentricity variations (Hussmann and Spohn, 2004). As a consequence of these complex tidal interactions and the eccentricity variations, the ice shell of Europa has been changing its thickness and exhibits geological processes such as faulting (Howell and Pappalardo, 2019) and subduction-like processes (Kihoulou et al., 2025). Although the tidal forces acting on Ganymede weaken as its distance from Jupiter grows, their role in understanding Ganymede's interior remains significant. European Space Agency's (ESA) Juice mission (JUpiter ICy moons Explorer) will be orbiting Ganymede in the 2030s, and measure its gravitational perturbations with high accuracy (Cappuccio et al., 2020). Gravitational perturbations due to periodic tidal deformation of Ganymede will bring important new constraints on its internal structure.

As we move further into the Saturnian system, we encounter a similar picture. The eccentric orbit of Enceladus, maintained by a 2:1 orbital resonance

with Dione, leads to tidal heating and geological activity. Tides are potentially responsible for cryovolcanism, water-rich plumes at its south polar region, and heating in its porous core (Porco et al., 2006; Spencer et al., 2006; Choblet et al., 2017). Moving on to the largest moon of Saturn, the big tidal response of Titan suggested the presence of a subsurface ocean decoupling its ice shell from its interior (Durante et al., 2019). Later on, the tidal response is reported to be smaller than the original estimate (Goossens et al., 2024), but with a much larger dissipation (Downey and Nimmo, 2025). Understanding the tidal response is crucial in assessing the internal structure and dynamics of the planetary bodies, and as we uncover increasing complexity in Solar System objects, the need for sophisticated modeling approaches grows accordingly.



(a) A volcanic explosion on Io captured by Voyager 1.



(b) Infrared view of Io captured by the Juno mission.

Figure 2: Io: from Voyager 1 to Juno. (Image credit: NASA/JPL-Caltech/SwRI/ASI/INAF/JIRAM)

In the planetary applications, the tidal response is usually computed through solid body tides, assuming that the effects of liquid reservoirs are negligible (e.g., Takeuchi and Saito, 1972; Tobie et al., 2005; Kamata et al., 2016). Later, it was shown that the dynamic flow in a subsurface ocean can produce dissipative waves and might have non-negligible effects in heating the planetary bodies (Tyler, 2008). The tidal flow in a subsurface ocean was investigated thoroughly by using a two-dimensional shallow water equations (e.g., Matsuyama, 2014; Matsuyama et al., 2018; Beuthe, 2016; Hay and Matsuyama, 2017, 2019a; Rovira-Navarro et al., 2023). The 2D models were followed by more general three-dimensional approaches that were able to show that the shallow water approximation cannot capture inertial waves, which can generate significant dissipation in the ocean (Rovira-Navarro et al., 2019; Rekier et al., 2019). Although these models were more sophisticated than the shallow water approximation, they neglected the simultaneous coupling between the ocean and the solid layers. Moreover, the models of the subsurface oceans have neglected the effect of the tidal flow on the induced gravitational potential and the tidal deformation. This effect could be particularly important in light of the upcoming missions of Juice and Europa Clipper. In order to interpret the accurate measurements of these missions (Hussmann et al., 2025; Grasset et al., 2013; Pappalardo et al., 2024), we require models that can consider most of the constituents that can affect the tidal response.

In this thesis, we investigate the tidal response of the moons of the Saturnian and Jovian systems. We focus specifically on the response to the eccentricity tides, study how the moons deform over their orbital period, and quantify how a potential subsurface liquid layer affects this response.

This thesis is composed of six chapters. Chapter 1 provides a brief summary of the quantitative and qualitative analysis of a planetary body's tidal response. It also gives a brief summary of the necessary tools to study the tidal response and its connection with the planetary body's internal structure. After establishing a working theory framework, albeit not complete, we give an overview of how the internal structure of a planetary body is determined by means of remote observations. We finalize this chapter by summarizing the two-dimensional shallow water approximation that is commonly used to calculate the tidal response of a subsurface ocean.

In Chapter 2, we derive the linearized three-dimensional equations, which are used in the rest of the thesis. We present the numerical implementations of these equations and three benchmarks that test Oceanus's correctness.

Chapter 3 applies the developed method to Enceladus to evaluate the tidal heating in its subsurface ocean. Specifically, the impact of the core deformation on the tidal dissipation is investigated. Moreover, we provide a comparison of the Laplace tidal equations and the three-dimensional approach.

Chapter 4 studies the tidal heating patterns of a hypothetical magma ocean on Io. In this chapter, we study the connection between the tidal response of a magma ocean and Io's surface features, such as the distribution of volcanoes and hot spots, and the heat flux from the volcanic eruptions. Additionally, we present, for the first time, the influence of dynamical flow due to eccentricity tides on the tidal Love numbers.

Chapter 5 extends the previous chapter by investigating the sensitivity of the Love numbers to ocean thickness and depth and comparing them with Juno's recent measurements.

In Chapter 6, we apply Oceanus to investigate the effects of compressibility in the tidal response of Ganymede. In addition, we also introduce the moon-moon tidal potential and study its effects in the time domain.

The main results and their implications are given in the Conclusion. The details of the spherical harmonics for the numerical implementation are summarized in the Appendix.

# 1. Tidal response of a planetary body

The internal structure of a planetary body and its orbital elements are inherently tied together. Over its long-term evolution, the internal structure of the planetary body will evolve in response to tidal interactions. On shorter time scales, during its tidal cycle, a planetary body responds to tides in accordance with its internal structure. The planetary body deforms and dissipates energy depending on the internal structure and orbital characteristics. This response provides constraints on the body's internal structure and gives insight into its evolution. In this chapter, we present the fundamental aspects of the tidal deformation and the standard methods used to compute the tidal response. Furthermore, we introduce a novel approach to compute the tidal response of a planetary body with a compressible liquid layer.

## 1.1 Characteristics of the tidal response

The gravitational interactions between a primary body (tide-raising body) and its satellite (tide-raised body) result in tidal deformation and dissipation in both bodies. These interactions are given by a tidal potential that depends on the distance between two bodies. In terms of the distance between the two bodies $r_d$ and the angle between the point in the tide-raised body and the line connecting the centers of the two bodies $\psi$, the tidal force is given in terms of (Murray and Dermott, 2000)

$$V_t = \frac{GM_p}{r_d}\left(\frac{r}{r_d}\right)^2 P_2\left(\cos\psi\right) = \frac{GM_p}{r_d}\left(\frac{r}{r_d}\right)^2 \frac{1}{2}\left(3\cos^2\psi - 1\right), \tag{1.1}$$

where $G$ is the universal gravitational constant, $M_p$ is the mass of the tide-raising body, $r$ is the radius of the tide-raised body, and $P_2$ is the degree 2 Legendre function. We assume that the satellite is in 1:1 spin-orbit resonance, rotates around the primary planet in an orbit with a small eccentricity $e \ll 1$, and has negligible obliquity. The time-dependent tidal potential of such a satellite takes the form (Kaula, 1964; Murray and Dermott, 2000)

$$V_t = \frac{GM_p}{a^3} r^2 e\left[3\sin\omega t\sin^2\vartheta\sin 2\varphi + \frac{3}{2}\cos\omega t\left(3\sin^2\vartheta\cos^2\varphi - 1\right)\right], \tag{1.2}$$

where $\vartheta$ is the co-latitude, $\varphi$ is the longitude, $\omega = 2\pi/T$ is the rotation rate with $T$ being the rotation period. As the satellite experiences the periodic tidal force, it deforms and, depending on its structure, dissipates energy, which can be calculated over a tidal cycle as follows

$$h_{tide}\left(r,\vartheta,\varphi\right) = \frac{1}{T}\int_{t_0}^{t_0+T} \boldsymbol{\sigma} : \dot{\boldsymbol{e}}\,\mathrm{d}t, \tag{1.3}$$

where $\boldsymbol{\sigma}$ and $\dot{\boldsymbol{e}}$ are the stress and strain-rate tensors induced by the deformation, respectively. The tidal response can be represented by the tidal potential Love number computed at the surface (Love, 1912)

$$V_g = k_2 V_t, \tag{1.4}$$

where $V_g$ is the gravitational potential induced by the tidal deformation. Traditionally, the Love number, $\bar{k}_2(\omega) = \mathrm{Re}\left(\bar{k}_2(\omega)\right) + i\mathrm{Im}\left(\bar{k}_2(\omega)\right) = |\bar{k}_2|e^{-i\epsilon(\omega)}$, is defined in the frequency domain, where the real and imaginary parts characterize the instantaneous and dissipative response, respectively. The global dissipation in a planetary body that undergoes a periodic tidal deformation can be written as (e.g., Tobie et al., 2005)

$$H_{tide} = -\frac{21}{2}\mathrm{Im}\left(\bar{k}_2\right)\frac{\left(\omega R_s\right)^5}{G}e^2, \tag{1.5}$$

where $R_s$ radius of the planetary body. The tidal Love number of an incompressible, homogeneous body with density $\rho$, surface gravity $g$, radius $R_s$, and complex rigidity $\bar{\mu}$ is (e.g., Castillo-Rogez et al., 2011)

$$\bar{k}_2 = \frac{3/2}{1 + \frac{19\bar{\mu}}{2\rho g R_s}}. \tag{1.6}$$

The dissipation due to the tidal deformation is related to the phase lag of the deformation

$$\tan\epsilon = -\frac{\mathrm{Im}\left(\bar{k}_2\right)}{\mathrm{Re}\left(\bar{k}_2\right)}, \tag{1.7}$$

and it characterizes the tidal dissipation with the tidal quality factor

$$Q^{-1} = \sin|\epsilon| = \frac{\mathrm{Im}\left(\bar{k}_2\right)}{|\bar{k}_2|}. \tag{1.8}$$

The tidal response of the planetary body, as established above, is a function of its density, radius, and complex rigidity. While for a planetary interior, the density and radius can be well constrained, the rigidity of the body can add complications to the problem. The complex rigidity of the body is directly connected to the rheology of the body; in other words, it determines how the body reacts when stress is applied. In general form, the rheology can be written in terms of complex compliance $J$

$$2\boldsymbol{e} = \int_{-\infty}^{t} \dot{\boldsymbol{\sigma}}^d J\left(t - t'\right)\mathrm{d}t, \tag{1.9}$$

where $\dot{\boldsymbol{\sigma}}^d$ is the time derivative of the deviatoric part of the stress, and $t$ is time. The complex rigidity is then defined in the frequency domain by the relation $\bar{\mu} = 1/\bar{J}$, where $\bar{J}$ is the Fourier transform of $J$. For an incompressible elastic body, the compliance function is given as $J = 1/\mu$, where $\mu$ is the shear modulus. By substituting this into the Equation 1.9, we obtain Hooke's law. However, as we move on to the planetary body applications, the material composing the bodies usually responds to the stress in a more complicated way than an elastic body. One of the commonly used rheologies is the Maxwell rheology, and it is simply obtained from the compliance function as

$$J = \frac{1}{\mu} + \frac{t - t'}{\eta}, \tag{1.10}$$

where $\eta$ is the viscosity. In an analog model, it is described as an elastic spring and a viscous damper connected in series. The elastic spring represents the instantaneous elastic deformation, whereas the damper represents the viscous flow

that relaxes the stress over time. The Maxwell rheology is usually characterized by the relaxation time $\tau = \eta/\mu$. While the Maxwell rheology has been widely used in planetary applications to calculate the tidal heating (Hussmann and Spohn, 2004; Tobie et al., 2005; Ojakangas and Stevenson, 1989), it is a poor approximation for the processes that are happening at the tidal frequencies (Castillo-Rogez et al., 2011; Efroimsky, 2012). It was shown that the Maxwell rheology underestimates the tidal dissipation (e.g., Tobie et al., 2025). More recently, it was demonstrated that the Andrade rheology is more suitable for investigating the tidal dissipation and deformation of the planetary bodies due to the fact that it can capture the transient properties of ice and rocky materials (Efroimsky and Lainey, 2007; Běhounková et al., 2015; Walterová and Běhounková, 2017; Walterová and Běhounková, 2020). The compliance function for Andrade rheology is given as

$$J = \frac{1}{\mu} + \mu^{\alpha-1} \left( \frac{t - t'}{\zeta \eta} \right)^{\alpha} + \frac{t - t'}{\eta}, \tag{1.11}$$

where $\alpha$ and $\zeta$ are the Andrade parameters. In this particular rheology, the tidal response also depends on the parameters $\alpha$ and $\zeta$. Based on the experimental data, the Andrade model is a better fit to study the tidal response because it can capture some attenuation properties of the planetary materials (e.g., Bierson, 2024). While the Andrade models still failed to explain lower frequency attenuation properties, the Sundberg-Cooper model was able to account for some features (Sundberg and Cooper, 2010). Each rheology has its own advantages and, in reality, the planetary bodies behave in different rheological regimes depending on material shear modulus and viscosity throughout their internal structure.

Although we acknowledge that the Andrade model, in general, is better suited for studying the tidal response, in this study, the most complicated rheology we are using is the Maxwell model. The reason for this simplification is that we focus on the tidal response of a dynamic subsurface ocean. Including the Andrade rheology (or a more complicated rheology) with a tidal flow in one model is computationally rather expensive; nevertheless, it is an issue to be addressed in the future.

While the above set of equations well defines the tidal response of a body as a whole, the reality is slightly different, and most of the outer Solar System moons are differentiated into several layers. The modeling of the tidal response of such bodies with multiple layers requires a little bit more sophisticated methods, which calculate the tidal response based on the solution of the equations of motion. The models that rely on the solid body tides are well established and widely used in literature to compute the tidal response of a layered body (Takeuchi and Saito, 1972; Spada, 2008; Melini et al., 2022; Kamata et al., 2016).

As described above, the tidal response is characterized by a single Love number $k_2$, while in more complicated scenarios, this definition may be insufficient. For a planetary body with lateral heterogeneities, the response of a planetary body can vary with respect to degree and order (e.g., Běhounková et al., 2017; Berne et al., 2023; Rovira-Navarro et al., 2024, 2025). A similar effect has been observed as it was shown that the moon-moon tides can excite the response at higher frequencies, resulting in a dynamic response of the ocean (Hay and Matsuyama, 2019b; Hay et al., 2020, 2022). In this work, we will show that this effect can be induced by eccentricity tides in the presence of a subsurface ocean (Chapters 4,

5, and 6).

## 1.2 Internal structure of the moons of the outer Solar System

Earth's internal structure is well constrained through ground-based observations and seismic measurements. However, in the outer Solar System, we lose the advantage of direct observations and have to rely on indirect evidence. Through observations of telescopes and satellite measurements, we can have constraints on the radius, mass, gravity, magnetic field, surface temperature, heat flow, surface composition, and ongoing geological processes at the surface (Hussmann et al., 2015). Combinations of these characteristics of a planetary body give us a picture of what the body's interior looks like. At the first step, the interior models are based on the observation of the body's radius $R$ and total mass $M$ (or equivalently, mean density), which can provide rough estimates of the mass fraction of individual constituents. Before introducing any radial structure to the moons, the internal structure of the outer Solar System moons can be modeled as two-layer or three-layer bodies. For example, based on the mean value of the density and the radius of the Saturnian and Jovian moons, we estimate the ice mass of the icy moons. While the total mass and radius of the bodies are well known and they can provide a first estimate of the body's interior, there is still a great ambiguity about the details of the structure. This ambiguity can be reduced by investigating the gravitational moments, $J_2$ and $C_{22}$, of the planetary body. The coefficient $J_2$ represents the polar flattening caused by the rotation, and the coefficient $C_{22}$ represents the equatorial bulge caused by the tides due to a primary body. If the planetary body is assumed to be in a hydrostatic equilibrium, in the first-order potential theory, these two coefficients completely determine its moment of inertia about the rotational axis. In addition to the mass and radius, the identity for the moment of inertia factor (MoI) (e.g., Hussmann et al., 2015)

$$\mathrm{MoI} = \frac{8\pi}{3MR_s^2} \int_0^{R_s} \rho\,(r)\, r^4 \,\mathrm{d}r, \tag{1.12}$$

provides an extra equation to be solved along with the mass-balance equations. The value of the MoI defines how the mass is distributed in a planetary body. The lower values of the MoI indicate that the planetary body is differentiated and the mass is concentrated towards the center, while the MoI of a homogeneous body (i.e., $\rho$ = const.) is 0.4. The values of the MoI of the selected icy moons and Io are given in Table 1.1. With observations of the gravitational moments, one can determine whether the body is in hydrostatic equilibrium. Specifically, a close polar flyby can determine the coefficient $J_2$ and a close equatorial flyby can determine $C_{22}$. If the body is in the equilibrium state, then we have the relation between the gravitational moments as $J_2 = (10/3)C_{22}$. For Jupiter's moon Io, the constraint $J_2 = (10/3)C_{22}$ is well satisfied, and Io is most likely to be in hydrostatic equilibrium (Anderson et al., 2001). Together with the mass, radius, and MoI information, we can get a rough picture of a planetary body and its layered structure. At the state of equilibrium, the pressure $p$ and density $\rho$ are

| | Radius (km) | Density ($\mathrm{kg\,m^{-3}}$) | Mass ($\times 10^{22}$ kg) | MoI factor |
|---|---|---|---|---|
| Io | 1821.6 | 3528 | 8.938 | 0.3778 |
| Europa | 1560.8 | 3013 | 4.805 | 0.3477 |
| Ganymede | 2631.2 | 1942 | 14.820 | 0.3115 |
| Enceladus | 252.1 | 1610 | 0.0108 | 0.3305 |
| Titan | 2574.7 | 1880 | 13.453 | 0.3414 |

Table 1.1: Radius, mean density, total mass, and MoI factor of selected icy moons and Io. The values are taken from Schubert et al. (2004) for Galilean moons, Iess et al. (2010) for Titan, and Iess et al. (2014) for Enceladus.

related by

$$\frac{\mathrm{d}p}{\mathrm{d}r} = -\rho\,(r)\,g\,(r)\,, \tag{1.13}$$

$$\frac{\mathrm{d}g}{\mathrm{d}r} = 4\pi G\rho\,(r) - \frac{2g\,(r)}{r}, \tag{1.14}$$

where $g$ is the gravitational acceleration. In the case of large icy satellites, such as Ganymede and Titan, increasing pressure in the $H_2O$ layer allows for the existence of ice-III, ice-V, and ice-VI (Figure 1.1b). Moreover, this increase in pressure results in a lower melting temperature of ice and could generate suitable pressure-temperature conditions for the presence of liquid-water oceans (Figure 1.1a). Once the approximate structure of the layers has been determined, further constraints follow from the temperature profile and heat transport mechanisms. In particular, the thickness of the outer ice shell for the icy moons of the outer Solar System can be inferred based on the heat transport regime. The small or mid-sized moons are potentially having a conductive ice shell, whereas in larger satellites thermal convection can be the dominant process (Hussmann et al., 2015). In the following three sections, we briefly explain the internal structure of the moons that are subjects of this work: Enceladus, Io, and Ganymede.

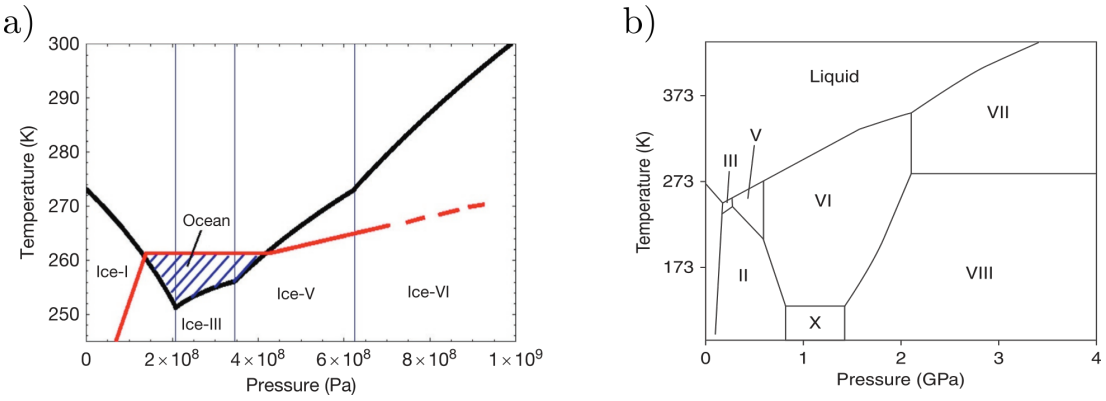



Figure 1.1: a) The favorable pressure and temperature conditions for an ocean to be present. b) Phase diagram of water. Both figures are taken from Hussmann et al. (2015).

## Enceladus

Enceladus, the tiny moon of Saturn, is one of the most complicated planetary body in our Solar System. It was discovered by William Herschel in 1789, and later observed by Voyager missions as it was the brightest of the moons of Saturn (Kargel and Pozio, 1996). It was not until the Cassini mission collected samples from its outbursting plumes at its south polar region (Porco et al., 2006; Hansen et al., 2011) that Enceladus became the focus point for the scientists. The analysis of the water ejecting from the geysers showed that Enceladus, beneath its bright ice shell, contains the necessary ingredients for life to emerge.

The small size of Enceladus and its mass suggest that it is composed of almost 40% of ice material (Schubert et al., 2007). The MoI of Enceladus suggests that it is differentiated into two layers: a low-density core and a hydrosphere (Iess et al., 2014). While the observations of the plumes, the heat flux, and the analysis of the gravity suggested that Enceladus has a hydrosphere around 60 km, the detailed structure of the hydrosphere remained puzzling. The observations of its plumes suggested that the plumes were fed by at least a regional liquid reservoir at the south pole (e.g., Běhounková et al., 2013). The reinterpretation of the Cassini data indicated the possible existence of a global subsurface ocean (McKinnon, 2015), and it was then followed from the large magnitude of libration that the ice shell and core are decoupled (Thomas et al., 2016). The initial estimates showed that the ice shell thickness of Enceladus is around 20 km on average (Thomas et al., 2016; Hoolst et al., 2016), where the thickness varies from a few kilometers to 30 km from the south polar region to the equator (Thomas et al., 2016; Čadek et al., 2016; Beuthe et al., 2016; Čadek et al., 2019a), and the estimated ocean thickness is around $\sim$ 38 km on average (Beuthe, 2016).

The estimated core density is around 2500 kg $m^{-3}$, indicating the core is unconsolidated (Roberts, 2015). Based on the gravity, topographic, and libration data, the estimated core size is between 180 and 195 km (Čadek et al., 2016; Beuthe et al., 2016; Hemingway and Mittal, 2019). Choblet et al. (2017) further estimated the porosity of the core to be between 20% and 30%. A core with such high porosity can generate sufficient tidal heating (Rovira-Navarro et al., 2022), and play a crucial role in maintaining a liquid subsurface ocean.

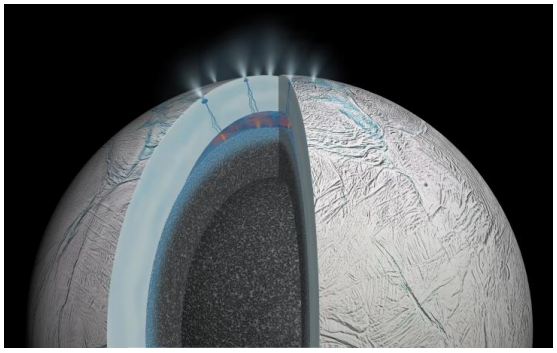


Figure 1.2: Artist representation of the internal structure of Enceladus (NASA/JPL-Caltech).

A recent study by Park et al. (2024b) has reanalyzed the data acquired by the Cassini spacecraft. Based on this analysis, they estimated a thicker ice shell, 27–33 km on average, a thinner ocean, 21–26 km, and core density in the range of 2270–2330 kg/$m^3$.

## Io

Io, the innermost moon of the Galilean system, is known for its intense volcanism. Prior to the confirmation of the volcanic activity, Peale et al. (1979) has predicted that the volcanism on Io is the result of the tidal heating. The Laplace resonance between Io, Europa, and Ganymede (in a 4:2:1 ratio) maintains Io's orbital eccentricity at approximately $e \approx 0.004$, causing it to undergo periodic tidal deformation with a period of 1.77 days. The average endogenous heat production of Io is estimated to be 100 TW (Lainey et al., 2009; Spencer et al., 2000). As a result of the intense heating, Io is the host to more than 400 volcanoes, some of which are erupting at any given time (e.g., Radebaugh et al., 2001; Schenk et al., 2001).

The initial suggested models consider an increasing density towards the center of the moon based on the MoI factor ($\approx 0.3776$ Anderson et al., 2001). These models depicted Io as a three-layer body with a liquid core, solid mantle, and a lithosphere. The core radius can vary between 650 and 950 km, corresponding to the composition of dense Fe-rich and lighter Fe-S, respectively (Breuer et al., 2022). The presence of tall mountains and volcanoes indicates the presence of a cold elastic lithosphere that is capable of supporting these features (O'Reilly and Davies, 1981). On the other hand, the structure of Io's mantle remained uncertain. While the high tidal dissipation would lead to large melt fractions in Io's interior, the distribution of the melt within the mantle was unclear. The surface geological features suggested the potential existence of a magma ocean beneath its lithosphere (Keszthelyi, 1999), while some argued that the extraction of the melt would lead to cooling of the mantle and prevent the magma ocean from being formed (e.g., Moore, 2001). The magma ocean hypothesis was later supported by Khurana et al. (2011), who investigated the magnetic data acquired from the Galileo spacecraft and inferred the presence of a potential conductive layer. Such a conductive layer was interpreted as the magma ocean 50 km beneath the surface. However, there were studies that argued that the data could be interpreted as interactions between the Jovian magnetosphere and Io's plasma environment (e.g., Roth et al., 2017; Blöcker et al., 2018).

A recent study showed that a steady state solid with high melt fractions would rapidly separate into two layers, forming a thin magma ocean ($\sim$ 1 km) in the upper mantle (Miyazaki and Stevenson, 2022). The tidal heating patterns of a magma ocean concentrate at lower latitudes, and depending on the ocean thickness and viscosity (Tyler et al., 2015; Matsuyama et al., 2022). Compared to the solid body tides, which concentrate the tidal heating at the poles, the magma ocean models were favorable since they were able to explain the distribution of the volcanoes and hot spots (Aygün and Čadek, 2024; Davies et al., 2024), and the observed eastward shift of the hot spot clusters (Tyler et al., 2015). While thermal and geological models give us constraints on the upper mantle structure, the investigation of the tidal response of Io can confirm or refute the presence of a magma ocean.

A study by Bierson and Nimmo (2016) showed that in the presence of a magma ocean, the tidal Love number $k_2$ should be around 0.5, while a solid body tide model would give $k_2 \sim 0.1$. Later, we have shown that the tidal response of Io with a liquid magma ocean, which produces 100 TW of heat, divides into two branches (Aygün and Čadek, 2024). If the ocean is thinner than 2 km, then

$k_2 < 0.1$, while if the ocean is greater than 2 km, $k_2 > 0.7$. While theoretical models of Io were being investigated, the Juno spacecraft made two flybys during late 2023 and early 2024 in order to retrieve the tidal response of Io. Park et al. (2024a) analyzed the data acquired by the Juno and provided $k_2 \approx 0.125$ and time lag approximately 2129.6 s. These values are inconsistent with the presence of a shallow magma ocean 50 km beneath the surface. However, Aygün and Čadek (2025) showed that a magma ocean at a depth of 200 km could still explain the measured Love numbers. The same study showed that even the dynamics of a thin magma ocean in a deeper mantle could alter the tidal response of Io. Thus, the question of whether there could be a deep magma ocean of Io could be answered by reinterpretation of the data using a more complex rheological model and/or by new observations addressing the order dependence of the $k_2$ Love number.

## Ganymede

Ganymede, the third Galilean satellite, is the largest moon in the Solar System, with a radius of 2631.6 km. Like the other two Galilean satellites, Io and Europa, its eccentricity is maintained by the Laplace resonance. Its current small eccentricity ($e = 0.0013$) and its distance from Jupiter result in moderate tidal deformation compared to Io and Europa (Showman et al., 1997; Hussmann and Spohn, 2004), yet tides can still play an important role in determining the internal structure of Ganymede.

The analysis of Ganymede's mean density ($\approx 1942\ \mathrm{kg\,m^{-3}}$) and radius suggests that it is composed of a significant amount of ice material (Hussmann et al., 2015). Its great size allows the pressure within its hydrosphere to exceed the point where ice I is no longer stable, resulting in the formation of the liquid phase or solid high-pressure ice phases. The Galileo mission provided data that show that there is a global subsurface ocean in Ganymede (Kivelson et al., 2002). The existence of a global subsurface ocean was further supported by the oscillations of auroral ovals (Saur et al., 2015).

The low value of the MoI factor (0.3115) indicates that Ganymede is differentiated into a core, mantle, and a hydrosphere (Anderson et al., 1996a). The Galileo mission also showed that Ganymede has its own intrinsic magnetic field, a feature unique among moons (Kivelson et al., 1996, 2002). Based on the high differentiation of its interior and the presence of an intrinsic magnetic field, the core is estimated to be liquid iron-rich with a radius between 600 and 800 km (Sohl et al., 2002). Moreover, combining the magnetic and gravitational data constrained the thickness of the hydrosphere between 800 and 900 km, and showed that it consists of an ice I outer shell, a liquid layer, and a solid high-pressure ice (Anderson et al., 1996a; Sohl et al., 2002; Kivelson et al., 2002; Vance et al., 2014, 2018). Based on the analysis of the surface material, it was suggested that the subsurface ocean should be rich in $MgSO_4$ (McCord et al., 2001), which is consistent with the global electrically conductive layer (Kivelson et al., 1996). While the composition of the ocean is uncertain, Vance et al. (2018) has estimated the ice shell thickness in the range of 5 to 157 km, and the ocean thickness in the range of 20 to 500 km. However, the thinner ice shell is less likely due to the high heat flux requirement and the lack of tidal heating. This is also supported by the magnetometer data, which estimates the outer ice shell thickness of $\sim 150$

km (Kivelson et al., 2002).

Despite the insights provided by gravity and magnetic data, significant uncertainties remain regarding Ganymede's internal structure. The Juice mission is sent to the Jovian system to close the gap with new important measurements (Grasset et al., 2013). Measurements that will be made by the Juice spacecraft will allow the Love numbers to be determined with unprecedented accuracy (Cappuccio et al., 2020), thus providing a unique constraint on the hydrosphere structure of the largest icy moon in the Solar System. Additional constraints will come from the magnetic measurements, where, together with the gravitational measurements, the thickness of the ice shell and ocean can be further constrained (e.g., Jia et al., 2025).

## 1.3 Tidal response of subsurface oceans: Shallow water approximation

The modeling of the tidal response of the solid bodies is well established. The methods have been verified by the observations of the Love numbers of the Earth. Classically, the tidal response of a planetary body is investigated through solid body tides, where the liquid layers are treated as an inviscid rheology (e.g., Dahlen, 1974; Takeuchi and Saito, 1972; Tobie et al., 2005). These models were developed to investigate the viscoelastic response of a layered body. There are also models which can treat the liquid layers as a viscous rheology, but these models neglect the rotational effects and inertial forces (e.g., Spada, 2008; Melini et al., 2022). These models were able to successfully estimate the Earth's Love number and were used in many applications for the moons of the outer Solar System, despite the abundance of subsurface liquid oceans.

Inspired by the oceanic models of Earth, there have been studies to investigate whether the tidal flow in a subsurface ocean could generate enough heat. Tyler (2008) has proposed that the resonantly excited waves due to the tidal flow in a subsurface ocean can generate strong dissipation. Including the effects of the Coriolis force can generate Rossby waves that cannot be restored by gravity waves, and enhance the energy dissipated in the ocean. To study the tidal dissipation in the subsurface ocean of Europa, Tyler (2008) used the Laplace tidal equations (LTEs), which are a system of equations that are obtained by vertically averaging the Navier-Stokes equations. The applicability of the LTEs is based on the fact that the thickness of the subsurface ocean is thin compared to the radius of the body. As it was shown that the ocean could potentially play a role in heating the oceans, many studies have followed to investigate the various moons (e.g., Tyler, 2009, 2014; Matsuyama, 2014; Matsuyama et al., 2018; Hay and Matsuyama, 2017, 2019a; Chen et al., 2014; Beuthe, 2016; Rovira-Navarro et al., 2020, 2023).

In this section, we show how the LTEs are connected to the 3D Navier-Stokes equations for a subsurface ocean beneath an elastic ice shell and above a rigid core, a model domain similar to the internal structure of Enceladus. In this particular model description, we assume that the ice shell and ocean are coupled and experience the tidal deformation, whereas the core is assumed to be rigid (this is a similar setting to models by Beuthe (2016) and Matsuyama et al. (2018)). We restrict ourselves to the governing equations that describe the flow in a viscous

liquid layer. The LTEs are obtained by radially (or vertically) averaging the 3D Navier-Stokes equations of an incompressible liquid ocean that are given as

$$\nabla \cdot \boldsymbol{v} = 0, \tag{1.15}$$

$$\rho_o \frac{\partial \boldsymbol{v}}{\partial t} = -\nabla p + \eta_o \Delta \boldsymbol{v} - 2\rho_o \boldsymbol{\omega} \times \boldsymbol{v} - \rho_o \nabla V_t + \rho_o \boldsymbol{g}, \tag{1.16}$$

where $\boldsymbol{v}$ is the velocity, $\rho_o$ is the density of the ocean, $p$ is the pressure, $\eta_o$ is the dynamic viscosity of the ocean, $\boldsymbol{\omega}$ is the angular velocity, $V_t$ is the tidal potential as in Equation 1.2, and $\boldsymbol{g} = -\nabla V_g$ is the gravitational acceleration computed from the induced potential $V_g$.

The boundary conditions for the ocean are written as a weighted free-slip condition

$$[v_r]^+_- = 0, \tag{1.17}$$

$$(\boldsymbol{\sigma} \cdot \boldsymbol{e}_r)_\tau = -\alpha \boldsymbol{v}_\tau + C_D \boldsymbol{v} |\boldsymbol{v}_\tau|, \tag{1.18}$$

where the subscript $\tau$ denotes the tangential component, $\alpha$ and $C_D$ are the linear and non-linear drag coefficients, respectively, and $[]^+_-$ denotes the jump of the enclosed quantity. The condition 1.17 ensures the continuity of the radial component of the velocity between the ocean and the ice shell. In the case of $\alpha \to \infty$ and $C_D \to \infty$, these boundary conditions correspond to the no-slip condition, and they correspond to the free-slip condition if $\alpha = 0$ and $C_D = 0$.

To obtain the LTEs, we assume that the tidal displacement is small, the ocean has constant density, and the radial flow is negligible. Then, the radially averaged balance of mass (Equation 1.15) is given as

$$\frac{\partial u_r}{\partial t} + d \nabla_s \cdot \overline{\boldsymbol{v}} = 0, \tag{1.19}$$

where $\overline{\boldsymbol{v}} = \overline{\boldsymbol{v}}(\vartheta, \varphi)$ is the radially averaged velocity, $d$ is the ocean thickness, $\nabla_s$ is the surface gradient, and $u_r$ is the radial displacement at ocean-ice boundary (e.g., Beuthe, 2016; Matsuyama et al., 2018). The pressure at the bottom of the ice shell is then written in the form

$$p = (\rho_o - \rho_i) g u_r - \rho_o (V_t + V_g) - \sigma_{rr}, \tag{1.20}$$

where $\rho_i$ is the density of ice, $\sigma_{rr}$ is the radial component of traction at the bottom of the ice shell. Lastly, the radially averaged balance of momentum is

$$\rho_o \frac{\partial \overline{\boldsymbol{v}}}{\partial t} = -\nabla_s p - 2\rho_o (\boldsymbol{\omega} \times \overline{\boldsymbol{v}})_\tau + \boldsymbol{F}(\overline{\boldsymbol{v}}), \tag{1.21}$$

where $\Delta_s$ is the horizontal Laplace operator, and $\boldsymbol{F}(\overline{\boldsymbol{v}})$ represents the dissipative term,

$$\boldsymbol{F}(\overline{\boldsymbol{v}}) = \eta_o \Delta_s \overline{\boldsymbol{v}} - \alpha \overline{\boldsymbol{v}} + C_D \bar{\boldsymbol{v}} |\bar{\boldsymbol{v}}|. \tag{1.22}$$

Equations 1.19, 1.20, and 1.21 are referred to as the LTEs. Note that the second term in Equation 1.22 is the result of the boundary friction term. The friction term in the 3D model characterizes solely the dissipative process at the interfaces, whereas in the 2D model, it is no longer a purely dissipative process at the boundary but in the whole ocean. Although the dissipation in the context of the LTEs

is often computed in the frequency domain (e.g., Matsuyama, 2014; Matsuyama et al., 2018; Hay and Matsuyama, 2017), we give an equivalent formula in the time domain (Beuthe, 2016)

$$H_s = \frac{2\eta_o d}{T} \int_{t_0}^{t_0+T} \int_S \dot{\bar{\boldsymbol{e}}} : \dot{\bar{\boldsymbol{e}}} \, \mathrm{d}S \, \mathrm{d}t, \tag{1.23}$$

where $S$ is the surface of the sphere of radius of the ocean, $t_0$ is an arbitrary time, and the strain-rate tensor is

$$\dot{\bar{\boldsymbol{e}}} = \frac{1}{2} \left( \nabla_s \overline{\boldsymbol{v}} + \nabla_s \overline{\boldsymbol{v}}^{\mathrm{T}} \right). \tag{1.24}$$

We have given the formula just for the viscous dissipation, because in this work, whenever LTEs are used, the friction terms are neglected.

While LTEs have become the standard approach for computing the tidal response of subsurface oceans, they are inherently limited to a two-dimensional approximation. The LTEs restrict the ocean flow in the horizontal directions, and the flow in the radial direction is neglected, although it may have importance (e.g., Ogilvie and Lin, 2004; Rovira-Navarro et al., 2019; Rekier et al., 2019). The comparison of the 2D and 3D approaches is given in Chapter 3.

# 2. A three-dimensional approach to tidal response of a subsurface ocean

In the previous chapter, we briefly introduced the tidal response of a solid body, and we presented the LTEs that are commonly used to calculate the tidal response of a subsurface ocean. The main assumption is that the horizontal scale of the flow is much larger than the vertical scale, which makes them suitable for studying the subsurface oceans in the outer Solar System. When assumptions of LTEs are relaxed to allow the radial flow in the ocean, a different class of waves, called inertial waves, start to emerge (e.g., Bretherton, 1964; Maas, 2001). These waves are shown to have importance in tidal dissipation in stars and giant planets (e.g., Rieutord et al., 2001; Ogilvie and Lin, 2004).

Recent studies by Rovira-Navarro et al. (2019) and Rekier et al. (2019) have developed three-dimensional models to investigate the subsurface oceans of Europa and Enceladus. They showed that the tidal flow can be resonantly excited and can lead to significant dissipation compared to dissipation computed by LTEs. In these approaches, the linearized equations of motion are solved in the frequency domain. In the former study, the deformation of the solid layers is neglected, while in the latter, the solid deformation is calculated without accounting for the effects of the ocean and is imposed as a boundary condition for the ocean.

## 2.1 Governing equations of Oceanus

Based on these studies, this chapter introduces a new model, Oceanus, which incorporates additional effects. Oceanus differs from the models of Rovira-Navarro et al. (2019) and Rekier et al. (2019) in three ways: (i) the viscoelastic deformation of the solid layers and the tidal flow in the ocean are coupled and solved simultaneously, (ii) we solve the problem in the time domain, and (iii) we include the effects of compressibility. We derive the linearized governing equations that are solved in Oceanus by following a similar method that is outlined in Chapter 9 by Martinec (2019). Unlike the previous section, we present the equations that are solved in the whole body and not just in the ocean. We assume that the planetary body is in a pre-stressed state, the tidal deformation is small, the domain of the problem is spherical (i.e., we neglect the thickness variations in the layers (e.g., Rovira-Navarro et al., 2020)), and we neglect the lateral variations in the physical parameters (e.g., Rovira-Navarro et al., 2024). We write the equations in the Eulerian formulation in differential form. In the most general form, the balance of mass is

$$\frac{\partial \tilde{\rho}}{\partial t} + \boldsymbol{v} \cdot \nabla \tilde{\rho} + \tilde{\rho} \nabla \cdot \boldsymbol{v} = 0, \tag{2.1}$$

and the balance of linear momentum is

$$\tilde{\rho} \left( \frac{\partial \boldsymbol{v}}{\partial t} + \boldsymbol{v} \cdot \nabla \boldsymbol{v} \right) = \nabla \cdot \boldsymbol{\tau} - \tilde{\rho} \boldsymbol{f} + \tilde{\rho} \boldsymbol{g} - 2 \tilde{\rho} \boldsymbol{\omega} \times \boldsymbol{v}, \tag{2.2}$$

where $\boldsymbol{f}$ is the body force, and density $\tilde{\rho}$ and Cauchy stress tensor $\boldsymbol{\tau}$ is defined as

$$\tilde{\rho} = \rho_0 (r) + \rho (t, r, \vartheta, \varphi), \tag{2.3}$$
$$\boldsymbol{\tau} = \boldsymbol{\tau}_0 (r) + \boldsymbol{\sigma} (t, r, \vartheta, \varphi). \tag{2.4}$$

Here, $r$, $\vartheta$, and $\varphi$ are the spherical coordinates, $\rho_0$ is the reference density, $\boldsymbol{\tau}_0$ is the reference Cauchy stress tensor, and $\boldsymbol{\sigma}$ and $\rho$ are the incremental Eulerian Cauchy stress tensor and density, respectively. By substituting the Equations 2.3 and 2.4 into 2.1 and 2.2, using the pre-stress condition $\nabla \cdot \boldsymbol{\tau}_0 = \rho_0 \boldsymbol{g}_0$, and neglecting the second order terms, we obtain the linearized balance of mass as

$$\frac{\partial \rho}{\partial t} + \boldsymbol{v} \cdot \nabla \rho_0 + \rho_0 \nabla \cdot \boldsymbol{v} = 0, \tag{2.5}$$

and the linearized balance of momentum as

$$\rho_0 \frac{\partial \boldsymbol{v}}{\partial t} = \nabla \cdot \boldsymbol{\sigma} + \rho_0 \boldsymbol{f} + \rho_0 \boldsymbol{g} + \rho \boldsymbol{g}_0 - 2\rho_0 \boldsymbol{\omega} \times \boldsymbol{v}, \tag{2.6}$$

where $\boldsymbol{g}_0$ is the reference gravitational acceleration, and $\boldsymbol{g} = -\nabla V_g$ the self-gravity induced by the deformation of the body

$$V_g (t, \boldsymbol{r}) = G \int_{V'} \frac{\rho (t, \boldsymbol{r}')}{|\boldsymbol{r} - \boldsymbol{r}'|} \mathrm{d}\, V'. \tag{2.7}$$

Here $\boldsymbol{r}$ is the position vector, and $V$ is the volume. The body force in the case of Oceanus is the eccentricity tidal potential (e.g., Kaula, 1964), $\boldsymbol{f} = -\nabla V_t$, where

$$\begin{aligned} V_t (t, r, \vartheta, \varphi) = V_{t,20} (t, r)\, P_{20} (\cos\vartheta) &+ V^c_{t,22} (t, r)\, P_{22} (\cos\vartheta) \cos 2\varphi \\ &+ V^s_{t,22} (t, r)\, P_{22} (\cos\vartheta) \sin 2\varphi, \end{aligned} \tag{2.8}$$

where and $P_{20}$ and $P_{22}$ are the associated Legendre functions of degree 2, order 0 and 2, respectively. In Equation 3.4, the coefficients are given as

$$\begin{aligned} V_{t,20} (t, r) &= \frac{3}{2} r^2 \omega^2 e \cos\omega t, \\ V^c_{t,22} (t, r) &= -\frac{3}{4} r^2 \omega^2 e \cos\omega t, \\ V^s_{t,22} (t, r) &= -r^2 \omega^2 e \sin\omega t. \end{aligned} \tag{2.9}$$

We assume that the planetary body is composed of distinct spherical layers (see Figure 2.1), and Equations 2.5 and 2.6 are solved in each layers simultaneously, where, at each layer, they are complemented by a constitutive equation. The deviatoric part of the constitutive equation for the whole body is written as (e.g., Čadek et al., 2017; Souček et al., 2019)

$$\frac{1}{\eta} \boldsymbol{\sigma}^d + \frac{1}{\mu} \frac{\partial \boldsymbol{\sigma}^d}{\partial t} = \nabla \boldsymbol{v} + \nabla \boldsymbol{v}^{\mathrm{T}} - \frac{2}{3} \nabla \cdot \boldsymbol{v} \mathbb{I}, \tag{2.10}$$

where $\eta$ is the dynamic viscosity, $\mu$ is the shear modulus, $\boldsymbol{\sigma}^d$ is the deviatoric part of $\boldsymbol{\sigma}$, and $\mathbb{I}$ is the identity tensor. The choice of $\eta$ and $\mu$ determine whether a layer is elastic ($\eta \to \infty$), Newtonian fluid ($\mu \to \infty$), or Maxwell viscoelastic solid.

In the first-order approximation, we assume that the volume changes occur instantaneously (i.e., bulk viscosity is neglected), and we derive the isotropic part of the constitutive equation by integrating and linearizing the identity for bulk modulus $K = \rho\,(\mathrm{d}p/\mathrm{d}\rho)$. This linearization results in the following relation that is valid in both the Eulerian and Lagrangian formulations

$$p^* = K\frac{\rho^*}{\rho_0}, \tag{2.11}$$

where $\bullet^*$ corresponds to $L$ for Lagrangian quantity and $E$ for the Eulerian quantity. Since the constitutive equation for a liquid layer is naturally written in the Eulerian formulation, Equation 2.11 simplifies to

$$p = K\frac{\rho}{\rho_0}, \tag{2.12}$$

where we used $p = p^E$ and $\rho = \rho^E$. In contrast to the liquid layers, the constitutive equation for a solid layer is naturally written in the Lagrangian formulation, in the context of small deformation. To derive the isotropic part of the constitutive equation for solid layers, first, we write 2.11 in terms of Lagrangian quantities $p^L$ and $\rho^L$ as

$$p^L = K\frac{\rho^L}{\rho_0}. \tag{2.13}$$

Then to obtain the Eulerian counterpart of the Equation 2.13, we use the identities $p^L = p + \boldsymbol{u}\cdot\nabla p_0$ and $\rho^L = \rho + \boldsymbol{u}\cdot\nabla\rho_0$, and Equation 2.5 (for details, see Martinec, 2019)

$$\frac{1}{K}\left(\frac{\partial p}{\partial t} - v_r\rho_0 g_0\right) = -\nabla\cdot\boldsymbol{v}, \tag{2.14}$$

where $\boldsymbol{u}$ is the displacement, and $v_r$ is the radial component of the velocity. The use of Equation 2.12 along with setting $\partial\rho/\partial t = 0$ in the viscous liquid layers allows us to avoid the unstable behavior due to the acoustic wave. If a layer is assumed to be incompressible, then Equations 2.12 and 2.14 are replaced by

$$\nabla\cdot\boldsymbol{v} = 0. \tag{2.15}$$

We assume that the surface of the body is free to deform, and the velocity and traction vectors are continuous at the internal boundaries. The boundary conditions are imposed at the reference spheres. The free-surface condition reads (Souček et al., 2019)

$$\boldsymbol{\sigma}\cdot\boldsymbol{e}_r = -\rho_0 g_0 u_r\boldsymbol{e}_r = -\rho_0 g_0\int_0^t v_r\boldsymbol{e}_r\,\mathrm{d}t', \tag{2.16}$$

where $\boldsymbol{e}_r$ is the radial unit vector. At the internal boundaries, the condition takes the form

$$[\boldsymbol{v}]^+_- = \boldsymbol{0}, \tag{2.17}$$

$$[\boldsymbol{\sigma}\cdot\boldsymbol{e}_r]^+_- = \Delta\rho_0 g_0 u_r\boldsymbol{e}_r = \Delta\rho_0 g_0\int_0^t v_r\,\mathrm{d}t', \tag{2.18}$$

where $\Delta\rho_0$ is the density difference between the layers at the internal boundaries. We enforce the no-slip condition in the liquid-solid boundaries by prescribing Equations 2.17 and 2.18.

Similar to its 2D counterpart (Equation 1.23), tidal dissipation in the planetary body is calculated over a tidal cycle by

$$H = \frac{1}{T}\int_{t_0}^{t_0+T}\int_V \frac{\boldsymbol{\sigma}^d : \boldsymbol{\sigma}^d}{2\eta}\,\mathrm{d}V\,\mathrm{d}t = \frac{2\eta}{T}\int_{t_0}^{t_0+T}\int_V \dot{\boldsymbol{e}} : \dot{\boldsymbol{e}}\,\mathrm{d}V\,\mathrm{d}t, \tag{2.19}$$

where $V$ is the volume of the planetary body. In Table 2.1, the linearized equations are summarized.

| | |
|---|---|
| Balance of mass: | $\frac{\partial \rho}{\partial t} + \boldsymbol{v}\cdot\nabla\rho_0 + \rho_0\nabla\cdot\boldsymbol{v} = 0$ |
| Balance of momentum: | $\rho_0\frac{\partial \boldsymbol{v}}{\partial t} = \nabla\cdot\boldsymbol{\sigma} - \rho_0\nabla V_t + \rho_0\boldsymbol{g} + \rho\boldsymbol{g}_0 - 2\rho_0\boldsymbol{\omega}\times\boldsymbol{v}$ |
| Constitutive equations | |
| Deviatoric part: | $\frac{1}{\eta}\boldsymbol{\sigma}^d + \frac{1}{\mu}\frac{\partial \boldsymbol{\sigma}^d}{\partial t} = \nabla\boldsymbol{v} + \nabla\boldsymbol{v}^{\mathrm{T}} - \frac{2}{3}\nabla\cdot\boldsymbol{v}\mathbb{I}$ |
| Isotropic part – Compressible – Liquid: | $p = K\frac{\rho}{\rho_0}$ |
| Isotropic part – Compressible – Solid: | $\frac{1}{K}\left(\frac{\partial p}{\partial t} - v_r\rho_0 g_0\right) = -\nabla\cdot\boldsymbol{v}$ |
| Isotropic part – Incompressible: | $\nabla\cdot\boldsymbol{v} = 0$ |

Table 2.1: Summary of the governing equations that are implemented in Oceanus. The equations are written in Eulerian configuration. They are solved simultaneously in all layers of the planetary body together with the boundary conditions 2.16, 2.17, and 2.18.

Finally, Oceanus outputs the tidal response of the body in terms of the Love numbers. In this work, we define the Love numbers in a way that incorporates the effects of the dynamic flow in a liquid subsurface ocean. We introduce the Love number separately for degree and order as $k_{20}$, $k_{22}^c$, and $k_{22}^s$, and define them by using the coefficients given in Equation 2.9

$$\begin{aligned} V_{g,20}(t,a) &= k_{20}V_{t,20}(t-\Delta t_{20},a),\\ V_{g,22}^c(t,a) &= k_{22}^c V_{t,22}^c(t-\Delta t_{22}^c,a),\\ V_{g,22}^s(t,a) &= k_{22}^s V_{t,22}^s(t-\Delta t_{22}^s,a), \end{aligned} \tag{2.20}$$

where $a$ is the radius of the body, $V_{g,\bullet}$ is the gravitational potential coefficient induced by the tides, and $\Delta t_{\bullet}^{\bullet}$ is the corresponding time lag of the tidal deformation. If the satellite is a solid body or the ocean dynamics are neglected, the Love numbers equal to each other can be represented by a single number, $k_{20} = k_{22}^c = k_{22}^s = k_2$.

## 2.2 Numerical implementation

The computation domain is assumed to be the full sphere, and it is separated into distinct layers, $DL_k$. Figure 2.1a shows the $DL_k$ for the case Ganymede. The governing equations, given in Table 2.1, are solved by a semi-spectral method in

the lateral variables and a finite difference scheme in the radius. The unknown variables, $\boldsymbol{v}$, $\boldsymbol{\sigma}$, and $\rho$ are expanded in terms of normalized spherical harmonics in colatitude and longitude (for details, see Appendix A.1). The resultant spherical harmonic coefficients are discretized in radius by using a staggered grid (Figure 2.1c). In the staggered grid, the stress $\boldsymbol{\sigma}$, pressure $p$ and density $\rho$ co-

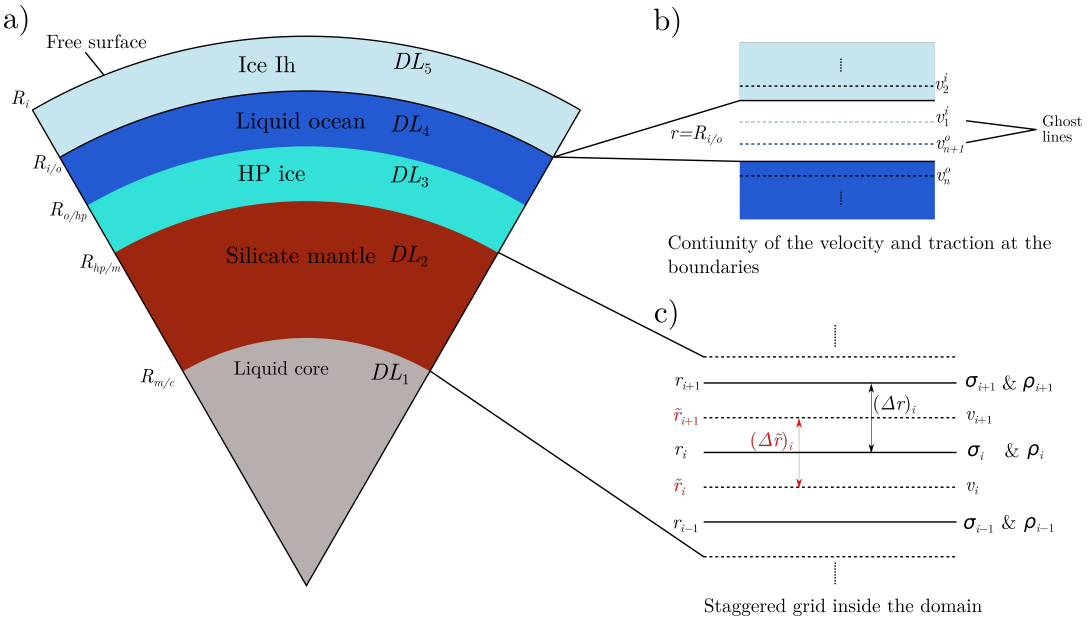



Figure 2.1: An example of a computational domain used for Ganymede. Equations given in Table 2.1 are solved in a spherical domain that has distinct layers – Ganymede is assumed to have 5 layers (a). In each layer, the domain is discretized in radius with a (in)homogeneous staggered grid (c), and the layers are coupled through boundary conditions (b).

efficients are represented at each interface lines within the domain (solid lines in Figure 2.1c), while the velocity $\boldsymbol{v}$ coefficients are represented at the middle of the interfaces, hereinafter mid-interface lines (dashed lines in Figure 2.1c). Each $DL_k$ has its own number of interface points $N_{DLk}$, and can either has a homogeneous or inhomogeneous radial step. The mid-interface line at $i$th line corresponds to the center of two adjacent interface lines (i.e., $\tilde{r}_i = 0.5\,(r_{i+1} + r_i)$). The radial steps are computed for each layer $(\Delta\tilde{r})_i = \tilde{r}_{i+1} - \tilde{r}_i$ and $(\Delta r)_i = r_{i+1} - r_i$ for $i = 1, ..., N_{DLk}$. The inhomogeneous grid is constructed by Chebyshev nodes in order to resolve the boundary layers in the viscous liquid domain.

The radial derivatives of the respective coefficients are approximated by a central finite difference scheme as

$$\begin{aligned} \frac{\partial v^l_{jm}\,(t, r_i)}{\partial r} &\approx \frac{v^l_{jm}\,(t, \tilde{r}_{i+1}) - v^l_{jm}\,(t, \tilde{r}_i)}{(\Delta\tilde{r})_i}, \\ \frac{\partial \rho_{jm}\,(t, \tilde{r}_i)}{\partial r} &\approx \frac{\rho_{jm}\,(t, r_{i+1}) - \rho_{jm}\,(t, r_i)}{(\Delta r)_i}, \end{aligned} \tag{2.21}$$

where $j$ and $m$ are the spherical harmonic degree and order (for details, see Appendix A.1), $r_i$ and $\tilde{r}_i$ are the $i$th position of the radius at the interface line and mid-interface line, respectively.

Each $DL_k$ in the computational domain is coupled by Equations 2.17 and 2.18. The top interface line of $DL_k$ and the bottom interface line of $DL_{k+1}$ have the same radius. At the boundary interface line, the material parameters of each interface are set according to the corresponding distinct layer. Each $DL_k$ is extended by a ghost line on the top and bottom of the layer (Figure 2.1b). These ghost lines enable us to keep the central difference in the radial discretization, and they are used in computing the velocity and traction at the interface boundary lines. At the innermost layer, the ghost line at the bottom corresponds to $\tilde{r} = 0$, and the boundary conditions are set such that the velocities are zero.

We solve the linearized equations of motion, but in the spectral domain, the advantage of linearity is lost due to the Coriolis force term. In the absence of the Coriolis force, the problem is separated by degree and order, and the solution for each degree and order can be obtained independently. However, the Coriolis force couples the adjacent degrees, resulting in higher-degree components. In principle, the Coriolis term can be treated implicitly, but this approach introduces additional complexity to the problem. We do not know beforehand the required number of spherical harmonic degrees (i.e., the cut-off degree). The cut-off depends on the vigor of the flow in the fluid layer, which in turn depends on the viscosity and the thickness of the liquid layer. If treated implicitly, depending on the parameters of the viscous liquid layer, the coefficient matrix can get very large, making the problem computationally infeasible. Therefore, we separate the momentum equation (Equation 2.6) into an implicit $\boldsymbol{I}(t)$ and an explicit part $\boldsymbol{E}(t)$

$$-\rho_0 \frac{\partial \boldsymbol{v}}{\partial t} + \boldsymbol{I}(t) = \boldsymbol{E}(t), \tag{2.22}$$

where

$$\begin{aligned} \boldsymbol{I}(t) &= \nabla \cdot \boldsymbol{\sigma} + \rho \boldsymbol{g}_0 - \rho_0 \nabla V_t, \\ \boldsymbol{E}(t) &= -(\rho_0 \boldsymbol{g} - 2\rho_0 \boldsymbol{\omega} \times \boldsymbol{v}). \end{aligned} \tag{2.23}$$

While the self-gravity term $\rho_0 \boldsymbol{g}$ is taken from the previous time step, the Coriolis term is implemented by using a second-order Adams-Bashforth method. The final form of the time-discretized momentum equations is

$$-\rho_0 \frac{\boldsymbol{v}^{k+1}}{\Delta t} = -\rho_0 \frac{\boldsymbol{v}^{k}}{\Delta t} + \theta \boldsymbol{I}(t^{k+1}) + (1-\theta)\, \boldsymbol{I}(t^k) + \left( \frac{3}{2} \boldsymbol{E}(t^k) - \frac{1}{2} \boldsymbol{E}(t^{k-1}) \right), \tag{2.24}$$

where $\Delta t$ is the time step, and $\theta$ is between 0.5 and 1, with the bounds corresponding to Crank-Nicolson and implicit Euler method, respectively. The time step is chosen according to the CFL condition to ensure the viscous flow in the liquid layer is accurately captured. During the computation, the cut-off degree $j_{\max}$ is self-consistently computed such that the condition $V(j_{\max})/V(2) < 10^{-4}$ is satisfied, where the $V(\bullet)$ is the $\mathrm{L}^2$ norm of the velocity at a given degree.

The numerical model described above was carefully tested against various models that are used in the literature. In the following three sections, we present three benchmarks that validate the correctness of Oceanus.

## Benchmark – 1: Tidal dissipation in Enceladus' subsurface ocean

This benchmark is composed of two parts, where in the first part, we calculate the dissipation in the ocean due to the tidal flow in the 3D setting. The results are compared with the results of Rekier et al. (2019)[1]. In the second part, we compare the results of the LTEs with the 3D method. For this benchmark, we assume a computational domain that is similar to Enceladus' interior: an elastic ice shell, a viscous liquid ocean, and a rigid core. The subsurface ocean is assumed to be a viscous incompressible liquid. In both parts of this benchmark, the tidal deformation of the core is neglected, and the deformation of the ice shell is calculated by solving the system

$$\begin{aligned} \nabla \cdot \boldsymbol{u} &= 0, \\ \nabla \cdot \boldsymbol{\sigma} &= \rho_i \left( \nabla V_t + \nabla V_g \right), \\ \boldsymbol{\sigma}^d &= \mu \left( \nabla \boldsymbol{u} + \nabla \boldsymbol{u}^{\mathrm{T}} \right), \end{aligned} \tag{2.25}$$

where $\boldsymbol{u}$ is the displacement, $\rho_i$ is the density, and $\mu$ is the shear modulus of the ice. In the first part of the benchmark, this deformation is imposed as a boundary condition at the ice-ocean boundary, while in the second part of the benchmark, the ice shell deformation is coupled with oceanic flow.

In the first part of the benchmark, we are solving the tidal dissipation in an incompressible subsurface ocean, where we include the effects of the Coriolis force. The governing equations of the subsurface ocean are given by Equations 2.6, 2.15 and 2.10 with $\mu \to \infty$. The boundary condition at the ice-ocean interface is given as

$$\boldsymbol{v} = \frac{\partial \boldsymbol{u}}{\partial t}, \tag{2.26}$$

where $\boldsymbol{u}$ is computed beforehand for an incompressible elastic ice shell with parameters $\mu = 3.5$ GPa and $\rho_i = 920\ \mathrm{kg\,m^{-3}}$. The radius of the core is set to $R_{o/c} = 192$ km. The set of Equations 2.25 is solved over a tidal cycle for different ice shell thicknesses, which corresponds to the ratio $R_{o/c}$ to $R_{i/o}$ in the range of 0.8 and 0.97.

For the analysis of the problem and the comparison with the results of Rekier et al. (2019), we introduce the Ekman number

$$\mathrm{Ek} = \frac{\eta}{2\rho_o \omega R_o^2}, \tag{2.27}$$

where $R_o$ is the radius of the ice-ocean boundary. The Ekman number, defined as the ratio of the viscous forces to the Coriolis force, characterizes the flow in a rotating body, and it is defined as the ratio of the viscous forces to the rotational forces. In the planetary bodies with liquid subsurface oceans, the typical value of the Ekman number is in the range of $10^{-13}$–$10^{-15}$, with the dynamic viscosity of $\eta = 10^{-3}$ Pa s. However, reaching these values is computationally challenging, and we restrict the value of viscosity to around 10–100 Pa s.

We solve the problem for viscosities that corresponds to the following three values Ekman number, $\mathrm{Ek} = 10^{-6}$, $10^{-7}$ and $10^{-8}$, and we compute the dissipation

[1]We would like to thank Jérémy Rekier for providing us with the results of his 3D simulations.

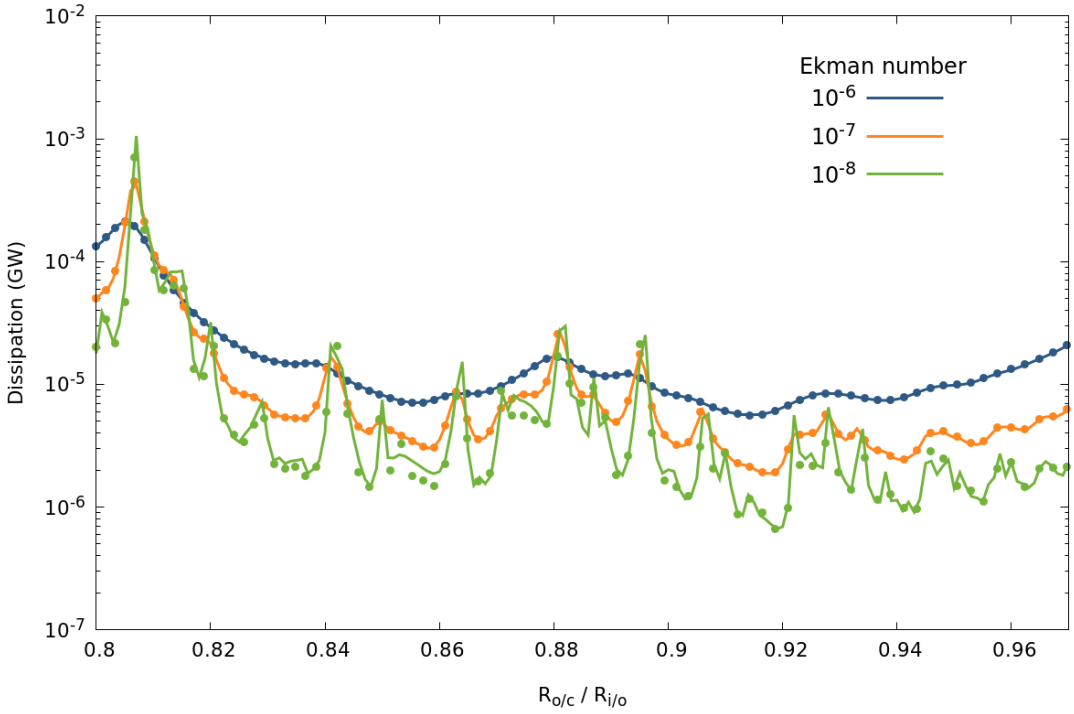



Figure 2.2: Tidal dissipation in Enceladus' subsurface ocean, computed for the Ekman number of $10^{-6}$, $10^{-7}$, and $10^{-8}$. The solid lines are the dissipation provided by Rekier et al. (2019), and the dots are current simulations. Note that the results of Rekier et al. (2019) are multiplied by 2, where the factor 2 is likely caused by a different definition of the Ekman number.

using Equation 2.19. The corresponding ocean thickness and the viscosity range from 5 to 50 km and from 20 Pa s to 3000 Pa s, respectively. The comparison with the results of Rekier et al. (2019) is given in Figure 2.2. Though we note that the results of Rekier et al. (2019) are multiplied by a factor of 2, which we believe is a factor due to a different definition of the Ekman number, we show that the results of the two models are in good agreement. The results of the two models are consistent within the range of ocean thickness and viscosity. We finally note that as the Ekman number decreases, the required computational power increases such that for $\mathrm{Ek} = 10^{-8}$ simulations, some of the calculations require thousands of periods to stabilize.

In the second part of the benchmark, we compare the results of the 3D model to the solution of LTEs. Unlike the first part, here, for both 3D and LTE models, the tidal deformation of the ice shell and the flow in the ocean are coupled through radial velocity. The solution of LTEs is obtained by solving the Equations 1.19, 1.20, and 1.21, while the solution of the 3D model is obtained by solving the Equations 2.6, 2.15 and 2.10 with $\mu \to \infty$. However, in the 3D model, unlike the default boundary conditions of Oceanus (which are no-slip), here, we prescribe a free-slip condition as given in Equations 1.17 and 1.18 with $\alpha = 0$ and $C_D = 0$. The reason for this change is that LTEs are naturally derived a weighted friction conditions (see Section 1.3). Because we prescribe the free-slip condition for the 3D model, in the dissipative term in LTEs (Equation 1.22, we only consider the viscous mechanism (i.e., $\boldsymbol{F} = \eta \Delta_s \bar{\boldsymbol{v}}$).

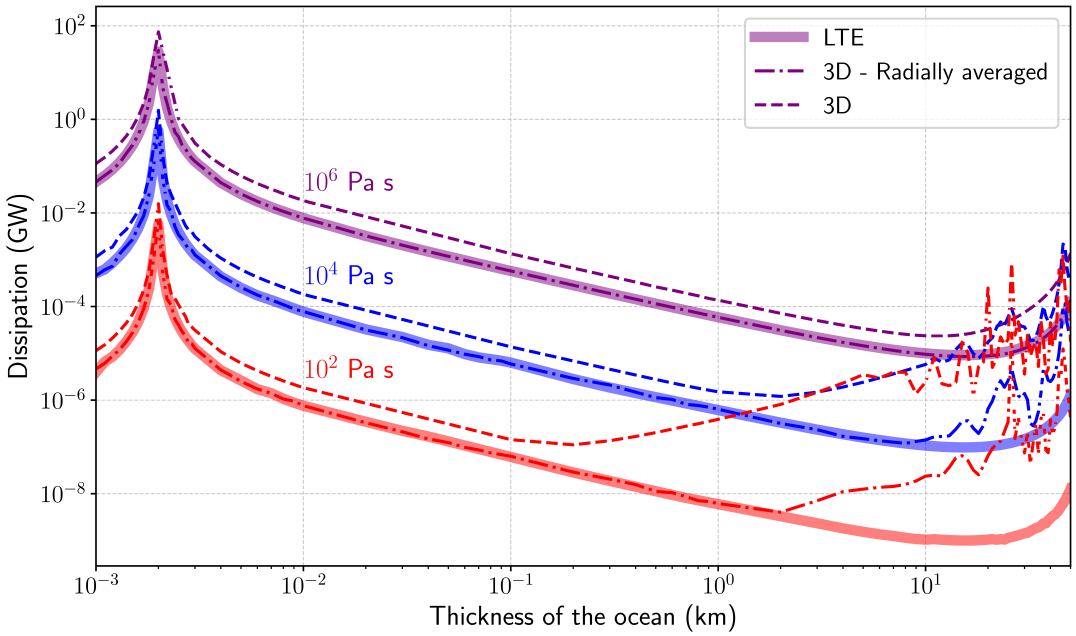



Figure 2.3: Comparison of the Laplace tidal equations and the three-dimensional approach with a free-slip condition. The thick solid lines represent the LTE solution, the dashed lines represent the 3D dissipation computed without radially averaging the velocity, and the dashed-dotted lines represent the dissipation computed from the radially averaged velocity.

The core radius is set to 194.1. We solve both models for the ocean thickness ranging from $10^{-3}$ to 50 km, where the corresponding ice shell thickness is computed from the core radius and radius of the body (252.1 km). The ice shell parameters are given as $\mu = 3.3$ GPa and $\rho_i = 925$ kg m$^{-3}$. We run the simulations for three viscosities, $\eta_o = 10^2$, $10^4$, and $10^6$ Pa s. In the LTE model, the tidal dissipation is calculated by Equation 1.23, while for the 3D model, the dissipation is calculated by Equation 3.8.

Figure 2.3 shows that the results of our 3D model are in good agreement for the thin ocean case when the dissipation is computed by radially averaged velocity. The agreement between the two models starts to diverge around 2 km ocean for low viscosity. However, if the 3D dissipation computed by Equation 3.8, i.e., without the radially averaged velocity, the two models lose the agreement, even more so the 3D model starts diverging already at an ocean thickness of 100 m. This indicates that the applicability of the LTEs is restricted to rather thin oceans ($< 100$ m).

## Benchmark – 2: Love numbers of an incompressible non-rotating spherically symmetric body

One of the commonly used codes for computing the viscoelastic Love numbers of a planetary body is ALMA$^3$, developed by Melini et al. (2022). This code is an extension of ALMA, originally developed by Spada (2008), which is developed based on the normal mode theory (e.g., Takeuchi and Saito, 1972). ALMA$^3$ has been designed to compute the tidal response of spherically symmetric, in-

compressible, viscoelastic layered planet bodies. The code solves the governing equations for viscoelastic deformation in the frequency domain, allowing for the calculation of tidal Love numbers. The code has been used to compute the tidal response of various planetary bodies, including, but not limited to, the Moon, Venus, and Mars (e.g., Briaud et al., 2023; Saliby et al., 2023; Petricca et al., 2022). In this benchmark, we compare the tidal Love numbers of Ganymede that are computed by ALMA$^3$ and Oceanus.

We set the model domain to be similar to Ganymede's internal structure: an inviscid liquid core, a silicate mantle, high-pressure ice, a viscous liquid ocean, and an ice I shell (Figure 2.1). The internal structure of Ganymede is defined by the ice shell thickness, which ranges from 80 to 150 km. For each ice shell thickness, the structure of the hydrosphere is calculated from the pressure-temperature conditions by using the SeaFreeze thermodynamic representation (Journaux et al., 2020). The densities of the mantle and core are fixed to 3500 and 8000 kg m$^{-3}$, respectively, and their radii are set to match the observed mass and MoI factor of Ganymede. The subsurface ocean has a Newtonian viscous rheology, and the solid layers are described as a Maxwell body. The viscosity of the ice shell is determined by the temperature profile by using the Arrhenius equation. The viscosities of the ocean, the high-pressure ice, and the mantle are set to $10^4$, $10^{15}$, and $10^{20}$ Pa s, respectively.

In this setting, the inertial terms, the Coriolis force, and the tidal flow in the core are neglected. The incompressibility condition is given by Equation 2.15, and the Equation 2.6 is simplified to

$$\nabla \cdot \boldsymbol{\sigma} = \rho_0 \left( \nabla V_t + \nabla V_g \right). \tag{2.28}$$

The constitutive equation is given by Equation 2.10, and the viscous rheology in the ocean part is obtained by using $\mu \to \infty$.

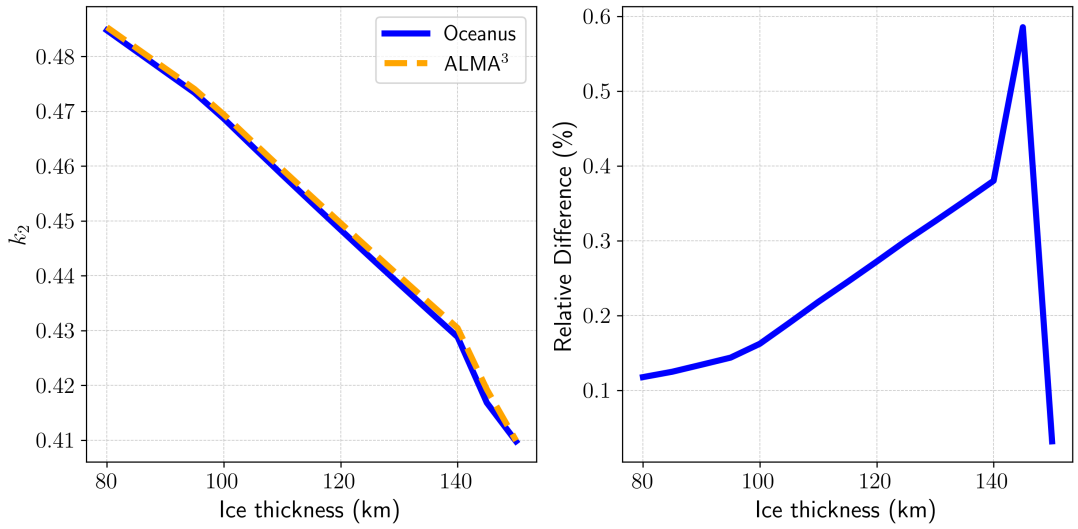



Figure 2.4: Comparison of $k_2$ computed by Oceanus and ALMA$^3$ for the incompressible model of Ganymede (left panel) and the relative error between the two solutions (right panel). On the left panel, the squares and crosses represent the results of ALMA$^3$ and Oceanus, respectively.

We compute Ganymede's Love numbers in response to the eccentricity tides (Equation 2.8), and the results of the benchmark are shown in the left panel of Figure 2.4. The Love numbers computed by the two codes are nearly indistinguishable throughout the entire ice shell thickness range. The agreement for the $k_2$ ranges from values that are less than 0.1%, for thin ice shells, to only up to 0.6% for thicker ice shells (left panel of Figure 2.4).

## Benchmark – 3: Love numbers of a compressible planetary body

The final benchmark is performed to test the implementation of the compressibility. Here, we compare the Love numbers of Ganymede computed by Oceanus and by the approach developed by Takeuchi and Saito (1972) (TS approach)[2], an approach that is commonly used in studying the spheroidal oscillation of a self-gravitating interior. Since the TS approach is also easily applicable for computing the compressible viscoelastic deformation of a layered body, it has been used in many planetary applications (e.g., Tobie et al., 2005; Kamata et al., 2015, 2016).

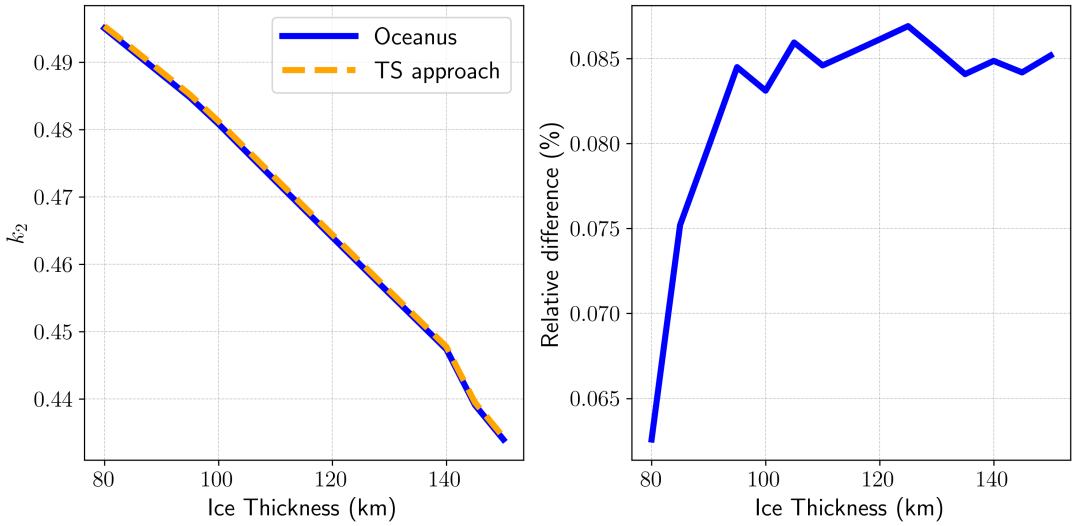



Figure 2.5: Comparison of $k_2$ computed by Oceanus and the method of Takeuchi and Saito (1972) (TS approach) for the compressible model of Ganymede (left panel) and the relative error between the two solutions (right panel). On the left panel, the squares and crosses represent the results of the TS approach and Oceanus, respectively.

We compute the compressible Love numbers of Ganymede both using the TS approach and Oceanus. We use the same internal structure as described in the previous benchmark, except here, ice shell thickness ranges from 80 to 150. We assume that the hydrosphere is compressible, and the silicate mantle and the core are assumed to be incompressible. We prescribe Maxwell rheology in the solid layers. In contrast with the previous benchmark, here, the subsurface ocean is treated in a hydrostatic approximation; in other words, we neglect the viscous

[2]We would like to thank Gabriel Tobie for providing us with the results of the TS approach.

flow in the ocean. Finally, we neglect the Coriolis force, but the inertial terms are included. The balance of mass and momentum equations for this benchmark are given as

$$\begin{aligned} \frac{\partial \rho}{\partial t} + \boldsymbol{v} \cdot \nabla \rho_0 + \rho_0 \nabla \cdot \boldsymbol{v} &= 0, \\ \rho_0 \frac{\partial \boldsymbol{v}}{\partial t} &= \nabla \cdot \boldsymbol{\sigma} - \rho_0 \left( \nabla V_t + \nabla V_g \right) + \rho \boldsymbol{g}_0, \end{aligned} \tag{2.29}$$

where for the solid parts, the constitutive relation is given by the Equations 2.10 and 2.14 for deviatoric and isotropic parts, respectively. The constitutive relation for the liquid subsurface ocean is given by the isotropic part, Equation 2.12.

The tidal Love numbers of Ganymede in response to the eccentricity tides computed by Oceanus and the TS approach are shown in the left panel of Figure 2.5. The left panel of Figure 2.5 shows that Oceanus can consistently reproduce the results of the TS approach when the ocean dynamics are neglected. We finalize the benchmarks by showing that we are able to reproduce the compressible Love numbers of Ganymede with a relative error that is less than 0.1% (right panel of Figure 2.5).

# 3. Impact of the core deformation on the tidal heating and flow in Enceladus' subsurface ocean

This chapter was published as Aygün and Čadek (2023) in *Journal of Geophysical Research: Planets*.

## 3.1 Introduction

Enceladus is a small icy moon with a global subsurface ocean. The ocean is likely to be maintained by tidal dissipation but the data tell us little about how and where the dissipation takes place. The total internal power of Enceladus is estimated to be between 10 and 50 GW (for a review, see Nimmo et al., 2018). Analysis of the stability of the ice shell suggests that the viscosity of ice at the contact with the ocean is higher than $3 \times 10^{14}$ Pa s (Čadek et al., 2019a). If this estimate is correct, then the heating rate due to tidal dissipation in the ice shell is $\sim$ 1 GW (Souček et al., 2019), which is much less than the heat loss due to conduction ($\approx$ 40GW, Čadek et al., 2019a). This indicates that the heat necessary to maintain the ocean at the melting temperature is produced in the core or the ocean itself.

Since the interior of Enceladus is likely to have never been exposed to high temperatures and pressures, the core may be made of unconsolidated, easily deformable, porous rock (Travis and Schubert, 2015; Roberts, 2015). Tidal deformation of such a material is associated with rearrangements of rock fragments, producing frictional heat that may explain Enceladus' heat budget (Choblet et al., 2017; Rovira-Navarro et al., 2022).

The amount of tidal heat generated within the ocean is still debated. The prevailing view is that heating caused by ocean tides is negligible at present but may have been significant in the past when dissipation could have been enhanced by resonance effects and/or the thickness of the ocean was strongly reduced (e.g., Matsuyama et al., 2018; Hay and Matsuyama, 2019a). In addition to tides, dissipation in the ocean can be caused by the turbulent flow response to the longitudinal libration of the ice shell. Whether this mechanism can provide enough heat to explain Enceladus' heat production, as suggested by, e.g., Lemasquerier et al. (2017) and Wilson and Kerswell (2018), will require further examination.

The first models of tidal dissipation in a subsurface ocean were based on the solution of the Laplace tidal equations (LTE). The studies pointed out the possible role of inertial waves in the thermal evolution of icy moons (Tyler, 2008, 2009, 2014, 2020) and provided the first estimates of the dissipative heat generated by oceans on Enceladus, Europa and other icy satellites (Chen et al., 2014; Matsuyama, 2014; Hay and Matsuyama, 2017). The limitation of this approach was that it was based on two simplifying assumptions: First, the thickness of the ocean, $D$, was assumed to be small compared to the outer radius of the ocean,

$R_{i/o}$, and second, the upper surface of the ocean was assumed to be free to move. In reality, neither of these assumptions is true: The ocean on Enceladus is not shallow ($D/R_{i/o} \approx 0.15$, see, e.g., (Čadek et al., 2016), (Beuthe et al., 2016) or (Hemingway and Mittal, 2019)) and its surface is covered with a $20-25$ km thick layer of solid ice (Thomas et al., 2016). Beuthe (2016) showed that the ice shell has a strong stabilizing effect on the tidal flow in the ocean, leading to a significant reduction of tidal dissipation. In the years that followed, the approach based on the solution of LTE, but including the dampening effect of the ice shell, was used to obtain more accurate estimates of dissipative power generated by subsurface oceans (Matsuyama et al., 2018; Hay et al., 2020) and to study the impact of non-linear bottom drag and ocean thickness variations on tidal dissipation (Hay and Matsuyama, 2019a; Rovira-Navarro et al., 2020).

To date, there are only two studies (Rovira-Navarro et al., 2019; Rekier et al., 2019) that have examined the tidal dissipation in a subsurface ocean by solving the three-dimensional Navier-Stokes equation (NSE). In both studies, the non-linear term in NSE ($\boldsymbol{v} \cdot \nabla \boldsymbol{v}$ where $\boldsymbol{v}$ is the flow velocity) is neglected and the problem is transformed into the frequency domain. The deformation of the ice shell is assumed not to be affected by the flow of water and is imposed as a boundary condition at the surface of the ocean. The latter study also takes into account the deformation of the core and includes the effects of self-gravitation and libration. The studies carefully analyze the role of inertial modes and agree that the heat production in Enceladus' present-day ocean is much smaller than the heat flux observed by Cassini (Spencer et al., 2018).

This paper offers an alternative approach to modeling the tidal response of a planetary body with a subsurface ocean. The approach is different from that used by Rovira-Navarro et al. (2019) and Rekier et al. (2019) in two respects: First, the tidal response is evaluated not only in the ocean but also in the crust and the core. In our approach, the equations governing the deformation in different parts of the body are linked by the boundary conditions guaranteeing the continuity of the velocity and traction vectors. This allows us to assess the effect of mechanical and gravitational coupling between the layers on the tidal dissipation process and specifically to investigate the interaction between the ocean and Enceladus' weak core. Second, the problem of tidal deformation is solved directly in the time domain as an initial value problem, similarly as in the case of thermal convection (except that the buoyancy force is replaced by the tidal force, see, e.g., Appendix A in (Kvorka and Čadek, 2022)). Although this approach is computationally more demanding than the solution in the frequency domain, it makes it possible to assess, at least in principle, the relative importance of non-linear effects and resonant interactions. These effects cannot be investigated by standard frequency domain methods because the response of a non-linear system to a periodic loading is not necessarily periodic in time. Our approach is also more general than that of Beuthe (2016) and Matsuyama et al. (2018) who coupled the flow in the ocean with the deformation of the ice shell and the core but used the LTE to calculate the tidal response of the ocean.

Modeling the coupled tidal deformation of an icy moon with a subsurface ocean and a plastic core is challenging and, therefore, several simplifying assumptions have been made to make the problem more amenable to solution. The most important one is the assumption that the lower boundary of the ice

shell is spherical. This assumption is motivated by numerical convenience and is widely used in studies of subsurface ocean dynamics that employ numerical tools based on the spectral decomposition of the governing equations. While the assumption of a constant ice shell thickness may be approximately satisfied in the case of large, slowly rotating icy moons, such as Titan, it is not valid for Enceladus where the thickness of ice varies laterally by tens of kilometers (e.g., Hoolst et al., 2016; Beuthe et al., 2016; Hemingway and Mittal, 2019; Čadek et al., 2016, 2019b). Although these variations are likely to affect the flow in the ocean (Rovira-Navarro et al., 2020, 2023; Soderlund et al., 2020; Kang et al., 2022), most studies addressing Enceladus' ocean dynamics do not include them because of the numerical difficulties arising from the implementation of irregular boundaries in spectral methods (e.g., Beuthe, 2016; Matsuyama et al., 2018; Rovira-Navarro et al., 2019; Rekier et al., 2019; Soderlund, 2019). One way to solve problems with complex geometry is to use the finite element method. However, even though this method has proven to be effective in modeling the tidal deformation and viscous flow in Enceladus' ice shell (Souček et al., 2016, 2019; Běhounková et al., 2017; Čadek et al., 2019a,b; Berne et al., 2023), its application to the tides in the ocean is still prohibitively expensive due to the fact that the thickness of the boundary layers in the ocean is much smaller than the characteristic length scale in the ice shell and, therefore, simulations have to be performed with a spatial resolution that is significantly higher than that usually considered in the ice shell.

Another limitation of our approach is that the viscosity of water used in our model is likely to be higher than the effective viscosity in the real ocean. The lowest value of the dynamic viscosity, $\eta$, that can be achieved in our numerical simulations is 100 Pa s, which is five orders of magnitude more than the molecular viscosity of water. Time-domain simulations with $\eta < 100$ Pa s place extreme demands on the numerical resolution needed to represent the velocity field and will require algorithms that achieve a higher level of parallelization and memory management. The lowest viscosity used in the 3D frequency-domain simulations by Rovira-Navarro et al. (2019) and Rekier et al. (2019) is about 70 Pa s and 0.2 Pa s, respectively. The effective viscosity of water may be significantly higher than the molecular viscosity due to the effect of turbulence (e.g., Pope, 2000). On Enceladus, the turbulent flow may occur because of the convective heat transfer in the ocean driven by the tidal heating in the core. The effect of turbulence on the effective viscosity of the water may be further enhanced in the bottom boundary layer as a result of the hydrothermal circulation in the core (Choblet et al., 2017) and the friction at the interface. In any case, the effective viscosity is likely to vary in space and time depending on the flow conditions and the degree of turbulence. The model with a constant viscosity should therefore be viewed as a first-order approximation of the tidal flow in the ocean.

While, for the reasons outlined above, the values of the dissipation rate predicted by our simulations should be interpreted with caution, the trends inferred here are generally valid and provide context for further studies in this area. In particular, we focus on the following questions: How much is the dissipation in the ocean affected by the deformation of the core? Does the deformation of the core depend on the thickness and viscosity of the ocean? How does the velocity field in the ocean change as a function of model parameters? Is the radial com-

ponent of the flow velocity significant? What are the validity limits of the LTE approach, which has been widely used to estimate heat production in subsurface oceans?

Based on the previous studies (e.g., Beuthe, 2016; Čadek et al., 2019a), we assume that the radius of Enceladus' core is about 190 km, and we vary the thickness of the ocean to investigate its role in different stages of Enceladus' evolution. Particular attention is paid to thin (≈1 km thick) ocean models that may be important for understanding the early stage of ocean formation. The results presented here may also help to clarify the role of tidal heating in the hypothetical oceans on Mimas (Tajeddine et al., 2014) and Dione (Beuthe et al., 2016; Zannoni et al., 2020) where the core may have material properties similar to those expected on Enceladus.

## 3.2 Method

We investigate the tidal deformation of an icy moon whose size and internal structure are similar to those of Enceladus. We assume that the moon consists of three layers: a solid ice shell, a liquid water ocean, and a solid core. The tidal deformation is solved simultaneously for all three layers, while the mechanical coupling between the layers is achieved by imposing continuity of traction and velocity at the boundaries. For simplicity, we assume that the boundaries are spherical, the material forming the moon is incompressible, and the tidal flow in the ocean is not affected by convective heat transport. The effect of tidal dissipation on material parameters is neglected. Under these conditions, the governing equations take the form

$$\nabla \cdot \boldsymbol{v} = 0, \tag{3.1}$$

$$\rho \left( \frac{\partial \boldsymbol{v}}{\partial t} + \boldsymbol{v} \cdot \nabla \boldsymbol{v} \right) = \nabla \cdot \boldsymbol{\sigma} - 2\rho \boldsymbol{\omega} \times \boldsymbol{v} - \rho \left( \nabla V_t + \nabla V_g \right). \tag{3.2}$$

Here, $\boldsymbol{v}$ is the velocity, $\rho$ is the density, $t$ is time, $\boldsymbol{\sigma}$ is the incremental Cauchy stress tensor, $\boldsymbol{\omega}$ is the angular velocity and $V_g$ is the gravitational potential due to tidal deformation (for details of the calculation, see Appendix A in Čadek et al., 2021),

$$\begin{aligned} V_g\left(t, r, \vartheta, \varphi\right) = G \int_{\vartheta'} \int_{\varphi'} \Bigg( & \int_{R_t}^{R_t + u_t} \frac{\rho_i}{|\boldsymbol{r} - \boldsymbol{r}'|} r'^2 dr' + \int_{R_{i/o}}^{R_{i/o} + u_{i/o}} \frac{\rho_o - \rho_i}{|\boldsymbol{r} - \boldsymbol{r}'|} r'^2 dr' \\ & + \int_{R_{o/c}}^{R_{o/c} + u_{o/c}} \frac{\rho_c - \rho_o}{|\boldsymbol{r} - \boldsymbol{r}'|} r'^2 dr' \Bigg) \sin\vartheta' d\vartheta' d\varphi', \end{aligned} \tag{3.3}$$

where $G$ is the gravitational constant, $r, \vartheta$, and $\varphi$ are the spherical coordinates, $R_t$, $R_{i/o}$ and $R_{o/c}$ are the radii of the density interfaces (see Figure 3.1) and $u_t$, $u_{i/o}$ and $u_{o/c}$ represent the shape changes of the boundaries. Finally, $V_t$ is the eccentricity tidal potential valid to first order in eccentricity (Kaula, 1964),

$$\begin{aligned} & V_t\left(t, r, \vartheta, \varphi\right) = r^2 \omega^2 e \\ & \left\{ \frac{3}{2} P_2^0\left(\cos\vartheta\right) \cos\omega t - \frac{1}{4} P_2^2\left(\cos\vartheta\right) \left[ 3\cos\omega t \cos 2\varphi + 4 \sin\omega t \sin 2\varphi \right] \right\}, \end{aligned} \tag{3.4}$$

where $e$ is the eccentricity, and $P_2^0$ and $P_2^2$ are the associated Legendre functions. The effect of obliquity tides on the deformation of Enceladus' ocean is likely to be small Baland et al. (2016) and is neglected. The dimensional analysis of Equation

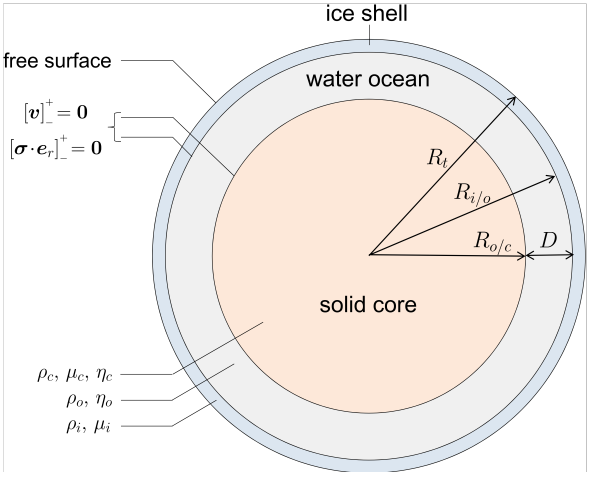



Figure 3.1: A sketch of the computational domain. Equations (3.1)–(3.5) are solved in a spherical domain made of three shells representing the solid ice crust, the liquid water ocean, and the solid silicate core. The radius of the core, $R_{o/c}$, is fixed at 194.1 km and the thickness of the ocean, $D$, is varied from 10 m to 50 km. We assume that the ice shell behaves as an elastic solid, while three different constitutive models of the core are considered (A–rigid, B–elastic, and C–viscoelastic). For details regarding the material parameters and the boundary conditions, see Table 3.1 and Equations (3.6) and (3.7), respectively.

(3.2) shows that the Coriolis ($2\rho\boldsymbol{\omega}\times\boldsymbol{v}$) and inertial ($\rho\partial\boldsymbol{v}/\partial t + \rho\boldsymbol{v}\cdot\nabla\boldsymbol{v}$) forces can be neglected in the ice shell and the core. In the ocean, Equation (3.2) can be simplified by neglecting the nonlinear term ($\rho\boldsymbol{v}\cdot\nabla\boldsymbol{v}$). The momentum equation is then linear in $\boldsymbol{v}$, and since the tidal potential is periodic, the problem can be solved in the frequency domain (Rovira-Navarro et al., 2019; Rekier et al., 2019). The simplification is usually justified by the long wavelength of the tidal forcing, or it is argued that the effect of turbulence can be included in the model by using the effective (eddy) viscosity. In the present study, the tidal deformation is modeled in the time domain, which will allow us to assess the relative importance of the nonlinear effects and quantify the error due to the linearization of the momentum equation.

The mechanical behavior of all three layers is described by a single constitutive equation (e.g., Čadek et al., 2017),

$$\frac{1}{\mu}\frac{\partial\boldsymbol{\sigma}^d}{\partial t} + \frac{1}{\eta}\boldsymbol{\sigma}^d = \nabla\boldsymbol{v} + (\nabla\boldsymbol{v})^T, \tag{3.5}$$

where $\boldsymbol{\sigma}^d$ is the deviatoric part of tensor $\boldsymbol{\sigma}$. Depending on the choice of the shear modulus $\mu$ and the viscosity $\eta$, Equation (3.5) describes either an elastic solid ($\eta\to\infty$), a Newtonian fluid ($\mu\to\infty$) or a Maxwell viscoelastic body. Note that since the conservation laws, Equations (3.1) and (3.2), are formulated in terms of the velocity, Hooke's law, and the Maxwell constitutive equation must be expressed in terms of the strain-rate tensor.

Table 3.1: Parameters of the model.

| Symbol | Parameter | Value | Unit |
|---|---|---|---|
| $R_t$ | Radius of the moon | 252.1 | km |
| $R_{i/o}$ | Radius of the ice/ocean interface | $194.11 - 244.1$ | km |
| $R_{o/c}$ | Radius the ocean/core interface | 194.1 | km |
| $e$ | Eccentricity | 0.0047 | |
| $\omega$ | Angular velocity | $5.31 \times 10^{-5}$ | $\mathrm{rad\,s^{-1}}$ |
| $\rho_i$ | Density of the ice shell | 925 | $\mathrm{kg\,m^{-3}}$ |
| $\rho_o$ | Density of the ocean | 1000 | $\mathrm{kg\,m^{-3}}$ |
| $\rho_c$ | Density of the core | $2350 - 2424$ | $\mathrm{kg\,m^{-3}}$ |
| $\eta_o$ | Viscosity of the ocean | $10^2 - 10^6$ | Pa s |
| $\eta_c$ | Viscosity of the core | | |
| | Model A | $\to \infty$ | |
| | Model B | $\to \infty$ | |
| | Model C | $6 \times 10^{11}$ | Pa s |
| $\mu_i$ | Shear modulus of the ice | $3.3 \times 10^9$ | Pa |
| $\mu_c$ | Shear modulus of the core | | |
| | Model A | $\to \infty$ | |
| | Model B | $10^9$ | Pa |
| | Model C | $2 \times 10^7$ | Pa |

Boundary conditions are imposed on the reference spheres of radius $R_t$, $R_{i/o}$, and $R_{o/c}$. Since the deformed surface of the moon is stress-free, the boundary condition at $r = R_t$ can be expressed as follows (Souček et al., 2019):

$$\boldsymbol{\sigma} \cdot \boldsymbol{e}_r = -\rho u_r g \boldsymbol{e}_r = -\rho g \boldsymbol{e}_r \int_0^t v_r dt', \tag{3.6}$$

where $u_r$ is the radial component of the displacement, $v_r$ is the radial component of the velocity, $g$ is the gravitational acceleration, and $\boldsymbol{e}_r$ is the radial unit vector. At the internal interfaces, the velocity and traction vectors are required to be continuous:

$$\begin{aligned} [\boldsymbol{v}]^+_- &= \boldsymbol{0}, \\ [\boldsymbol{\sigma} \cdot \boldsymbol{e}_r]^+_- &= \Delta\rho u_r g \boldsymbol{e}_r = \Delta\rho g \boldsymbol{e}_r \int_0^t v_r dt', \end{aligned} \tag{3.7}$$

where $[\cdot]^+_-$ represents the jump of the enclosed quantity across the interface and $\Delta\rho$ is the density difference ($\rho_o - \rho_i$ or $\rho_c - \rho_o$).

The total heat production of the moon is calculated using the following formula (e.g., Tobie et al., 2008):

$$H = \frac{1}{P} \int_{t_0}^{t_0+P} \int_V \frac{\boldsymbol{\sigma}^d : \boldsymbol{\sigma}^d}{2\eta} dV\, dt = \frac{1}{P} \int_{t_0}^{t_0+P} \int_V 2\eta\, \dot{\boldsymbol{e}} : \dot{\boldsymbol{e}}\, dV\, dt, \tag{3.8}$$

where $P$ is the rotation period ($P = 2\pi/\omega$), $t_0$ is an arbitrary time, and $V$ is the volume of the moon and $\dot{\boldsymbol{e}} = \frac{1}{2}(\nabla \boldsymbol{v} + (\nabla \boldsymbol{v})^T)$. In section 3, the lateral variations of tidal dissipation in the ocean are characterized by the heat production integrated over the radius Souček et al. (2019):

$$q\left(\vartheta,\varphi\right)=\frac{1}{P}\int_{t_0}^{t_0+P}\frac{1}{R_{i/o}^2}\int_{R_{o/c}}^{R_{i/o}}\frac{\boldsymbol{\sigma}^d:\boldsymbol{\sigma}^d}{2\eta}r^2\,dr\,dt. \tag{3.9}$$

Data collected by the Cassini spacecraft suggest that the ocean is at a depth of about 20 km below the surface on average (Thomas et al., 2016; Hoolst et al., 2016) and that the mean ocean thickness is about 40 km (Beuthe et al., 2016; Čadek et al., 2016, 2019a). It is likely, however, that the thickness of the ocean has changed in the past and will change in the future. In order to understand the role of ocean tidal dissipation in Enceladus' evolution, we vary the thickness of the ocean from 10 m to 50 km. The lower bound of the interval corresponds to the case where the ocean is almost completely frozen but it is mechanically decoupled from the core by a thin layer of liquid water or partially molten ice. In all simulations, we assume that the radius of the core is 194.1 km Čadek et al. (2019a) and we change the thickness of the ocean by changing the radius of the ice/ocean interface.

We assume that the ice shell behaves as an elastic solid. As shown by Souček et al. (2019) and Berne et al. (2023), the effect of viscosity on tidal deformation of Enceladus' ice shell is minor and can be neglected in the first approximation. Unfortunately, there are presently no observations to constrain the material parameters of Enceladus' core. In most of the previous studies on the ocean tides, the core was assumed to be rigid and its effect on the flow in the ocean was neglected. However, if the core has never been exposed to high temperatures and pressures, the core material may still be in an unconsolidated, fragmented state and may effectively behave as a low rigidity, low viscosity viscoelastic body (Travis and Schubert, 2015; Roberts, 2015; Choblet et al., 2017; Rovira-Navarro et al., 2022). If this is the case, the tidal deformation of the core may affect the flow in the ocean in a similar way as the tidal deformation of the ice shell. Here we consider three models of the core: A - the rigid core, B - the elastic core with $\mu_c = 10^9$ Pa (cf. Roberts, 2015), and C - the viscoelastic core with $\mu_c = 2 \times 10^7$ Pa and $\eta_c = 6 \times 10^{11}$ Pa s. The parameters of model C are chosen so that the total heat production of the core is roughly 25 GW (cf. Figure 1a in Choblet et al., 2017). The parameters of models A–C are summarized in Table 3.1.

Equations (3.1)–(3.7) are solved in the time domain using a pseudo-spectral method similar to that used by Kvorka and Čadek (2022). The unknown functions $\boldsymbol{v}$ and $\boldsymbol{\sigma}$ are represented in terms of the generalized spherical harmonic expansions (e.g., Golle et al., 2012), truncated at degree $\ell_{\max}$. The cut-off degree $\ell_{\max}$ is chosen so that $V(\ell_{\max})/V(2) < 10^{-4}$, where $V(\ell)$ denotes the $L_2$ norm of the velocity field at degree $\ell$, and ranges from 10 to 220 depending on the thickness and viscosity of the ocean. The coefficients in the harmonic series are discretized in the radial direction on an uneven grid consisting of 800 Chebyshev nodes (for an example of the radial resolution, see Figure B.1 in Appendix B.1). The radial resolution varies from 1 m in the ocean boundary layers to 1.5 km in the ice shell and the core. The time derivatives in Equations (3.2) and (3.5) are discretized using the implicit Euler method, while the explicit second-order Adams-Bashforth method is applied to the Coriolis and non-linear terms. Each simulation is started from the initial condition $\boldsymbol{v} = \boldsymbol{0}$, and the equations are integrated in time until a periodic solution is reached (cf. Tobie et al., 2008; Běhounková et al., 2010). At each time step, the accuracy of the method is assessed by evaluating the energy

balance (Patočka et al., 2018). The numerical method was coded in Fortran 90 and tested against the results by Beuthe (2016) and Rekier et al. (2019), see section 3.5 and Figure 2.2.

## 3.3 Tidal Dissipation in the Ocean and the Core

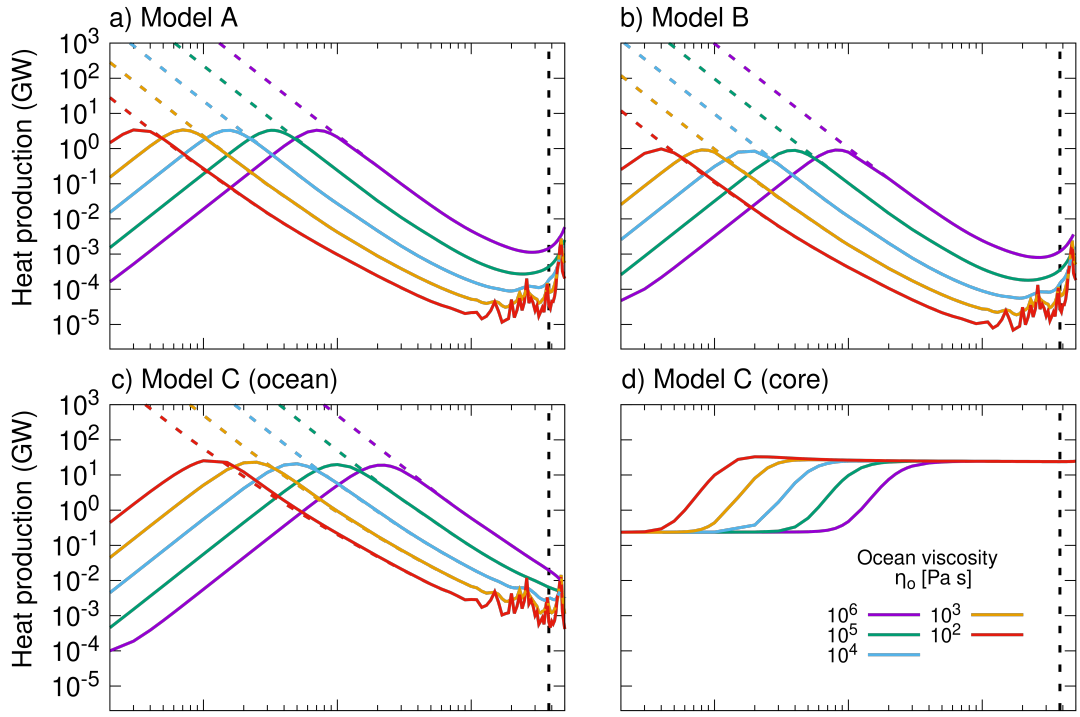



Figure 3.2: Heat production in Enceladus' ocean (a–c) and core (d) as a function of ocean thickness evaluated for different values of viscosity $\eta_o$. Heat production in the core is shown only for model C since the core in models A and B is treated as non-dissipative ($\eta_c \to \infty$). The solid lines represent models where the deformation equations are solved in the whole domain (including the solid parts, see section 2), while the colored dashed lines correspond to models where the flow is solved only in the ocean and the deformation of the ice shell the core is implemented through boundary conditions Rekier et al. (2019). The vertical black dashed lines indicate the current thickness of Enceladus' ocean.

Figure 3.2 shows the tidal dissipation in the ocean (panels a–c) and the core (d) as a function of ocean thickness for different values of ocean viscosity. Comparison of panels a–c reveals two general trends: (i) The maximum heat production in the ocean is independent of the viscosity of the ocean but depends on the material properties of the core ($H = 4$ GW for model A but 20 GW for model C). The value of $D$ at which the maximum is reached in less than 2 km and decreases with decreasing viscosity. (ii) When the ocean thickness is larger than 5 km, the curves are similar in shape to those obtained by Rekier et al. (2019) and Rovira-Navarro et al. (2019). The curves are characterized by several resonance peaks whose amplitudes increase with decreasing viscosity. The dissipation in the ocean is less than 0.1 GW and thus insufficient to explain the heat output ($> 10$ GW) of present-day Enceladus ($D = 38$ km).

The maximum heat production obtained for model A (stiff core) is twice as high as for model B (elastic core). This somewhat counterintuitive result is due to the fact that, in the elastic case, the upper and lower boundaries move in phase, and consequently, the radial deformation of the fluid layer is smaller than in the case of the rigid core. The parameters of model C are chosen such that the deformation of the ocean/core boundary is significantly larger than that of the elastic shell. The Deborah number of the core ($\tau_M/P$ where $\tau_M = \eta_c/\mu_c$ is the Maxwell time and $P$ is the rotation period) is about 0.25, implying that the tidal response of the core is dominated by viscous flow. This, together with the fact that the response of the core to the tidal force is delayed, results in an enhancement of the heat production in the ocean (Figure 3.2c). The maximum heat production is about 20 GW and is attained for a slightly larger value of $D$ than in models A and B (70 m to 2.5 km, depending on $\eta_o$). This suggests that tidal dissipation in a thin ocean may be sufficiently high to prevent the ocean from freezing. The thickness of the ocean influences not only the dissipation in

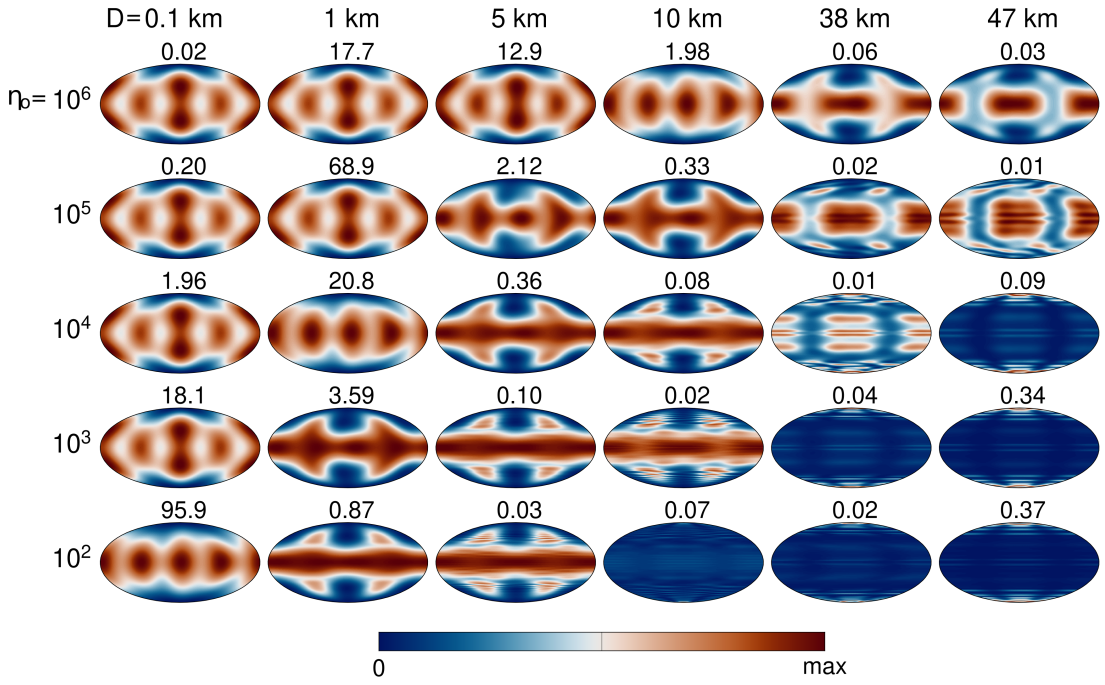



Figure 3.3: Surface distribution of ocean tidal heating averaged over the tidal cycle, Equation (3.9), for different thicknesses (columns) and viscosities (rows) of the ocean. All heat flux maps are computed for model C and shown in the Mollweide projection with the sub-Saturnian point at the center. For the sake of comparison of the heating patterns, each map is scaled to its own maximum (indicated above the map in mW/m$^2$).

the ocean itself but also in the viscoelastic core (Figure 3.2d). When the thickness of the ocean drops below a critical value, $D_{crit}$, the heat production in the core starts to decrease rapidly. The thickness of the ocean at which the drop occurs roughly corresponds to the thickness at which the dissipation in the ocean reaches a maximum value (cf. Figure 3.2c and 3.2d). Note that the heat production in the core for $D > D_{crit}$ is the same as the maximum heat production in the ocean, suggesting that at $D \approx D_{crit}$, the role of the core as the main producer of heat

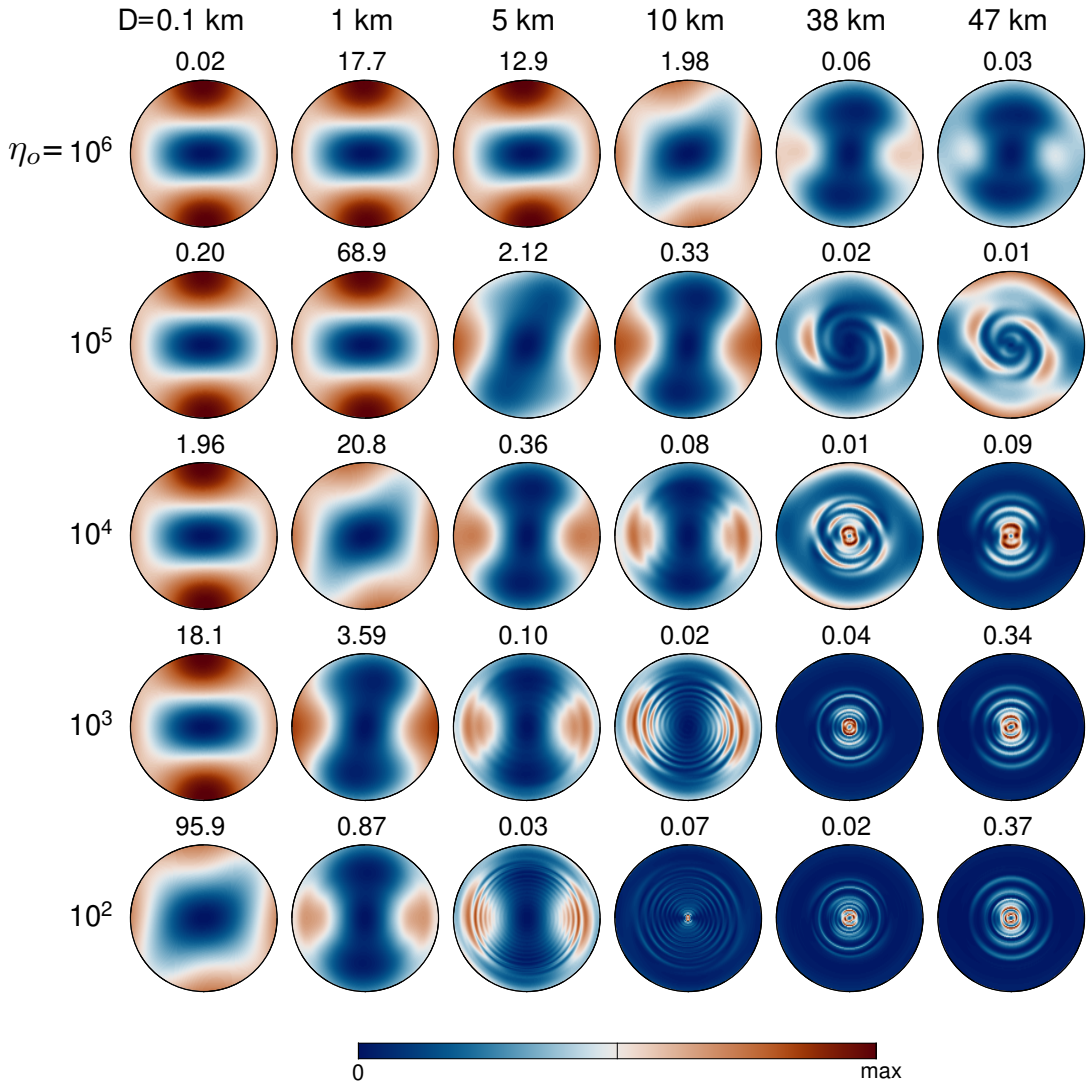



Figure 3.4: As in Figure 3.3 but in North pole stereographic projection.

is taken over by the ocean. When the ocean thickness is further decreased, the heat production in the ocean goes to zero, and the total tidal heat production of the moon approaches a value of 0.25 GW, corresponding to dissipation in a viscoelastic core surrounded by a shell of elastic ice.

As already mentioned in section 2, our approach is different from the one used by Rekier et al. (2019) in that the deformation equations are solved simultaneously in the whole domain (including the solid parts) while Rekier et al. (2019) first calculate the deformation of the ice shell and the core and then use it as a boundary condition to compute the flow in the ocean. Comparison of the solid and dashed lines in Figure 3.2 (panels a–c) shows that the two approaches give the same heating rates for $D > D_{crit}$, implying that the flow in the ocean has little impact on the deformation of the ice shell and the core if the ocean thickness is larger than about 2 km. However, the approach where the deformation of the solid parts is not self-consistently included grossly overestimates the tidal dissipation in the ocean for $D < D_{crit}$. It is likely that Rekier et al. (2019) anticipated this behavior and therefore only considered models where $R_{o/c}/R_{i/o} < 0.98$ (corresponding to $D \approx 4$ km). The large discrepancy between the two solutions

suggests that the assumption that the deformation of the ice shell and the core is independent of the tidal flow in the ocean is not valid for $D < D_{crit}$. This implies that the mechanical coupling between the ocean and the solid parts of the moon must be considered when evaluating dissipation in a thin ocean.

The flow induced by eccentricity tides in Enceladus' ocean yields a wide variety of heating patterns depending on the thickness of the ocean and its viscosity (Figures 3.3 and 3.4). For some combinations of parameters $\eta_o$ and $D$, the heat flux distribution is similar to those obtained using the shallow water approximation (see Figure 4 in Tyler et al. (2015) or Figure 7 in Matsuyama et al. (2018)). In most cases, however, the heat flux distribution is rather complex, indicating that dissipation in the ocean is strongly influenced by three-dimensional flow effects. The heat flux distribution obtained for $D = 47$ km and $\eta_o \leq 10^4$ Pa s, characterized by a system of concentric circular fringes, is compatible with the presence of inertial waves discussed by Rovira-Navarro et al. (2019) and Rekier et al. (2019).

The spatial distribution of the tidal heat produced in the core is independent of the viscosity and thickness of the ocean and only differs by magnitude. Similar to the results of Roberts (2015, Figure 3b) and Choblet et al. (2017, Figure 1c), the maximum heat flux is concentrated over the polar regions, reaching the value of about 70 mW/m$^2$ for $D > D_{crit}$ and 0.66 mW/m$^2$ when $D \to 0$ (see also Figure B.2 in Appendix B.1).

## 3.4 Velocity Field in the Ocean

A number of studies of ocean tides have been based on the assumption that the horizontal scale of flow is much larger than the depth of the ocean. Under this assumption, the trajectories of water parcels are nearly horizontal, the radial velocity is small compared to the horizontal velocity and the Navier-Stokes equations can be reduced to a two-dimensional form, called the Laplace tidal (or shallow water) equations, in which the horizontal velocity is a function of only $\vartheta$ and $\varphi$. The equations do not contain the radial component of velocity and the effect of radial flow on the viscous, inertial, and Coriolis force is neglected (Tyler, 2008). In this section, we will address the limitations of this approach and demonstrate the complex structure of the tidal flow in Enceladus' ocean. We will follow up on the studies by Rovira-Navarro et al. (2019) and Rekier et al. (2019) that have investigated the tidal response of a subsurface ocean by solving the three-dimensional Navier-Stokes equations. However, unlike these studies, we will present the flow field distribution not in the frequency domain but in the time domain, and we will examine the importance of the non-linear term in the momentum equation, which has been neglected in previous research.

In Figure 3.5, we show the velocity field at time $t = 0$ for models with $\eta_o = 100$ Pa s and $D$ ranging from 0.1 to 47 km. Note that for clarity, the thickness of the ocean in the visualization is fixed at $D = 0.25R_{o/c} \approx 50$ km. Inspection of the figure shows that the assumption of shallow water is well satisfied for $D \lesssim 1$ km but breaks down when $D \gtrsim 5$ km. When $D = 38$ km (corresponding to the average ocean thickness at present), the radial and tangential components are the same size, and the horizontal scale of the flow is comparable with the thickness of the ocean, suggesting that the shallow water approach is not suitable

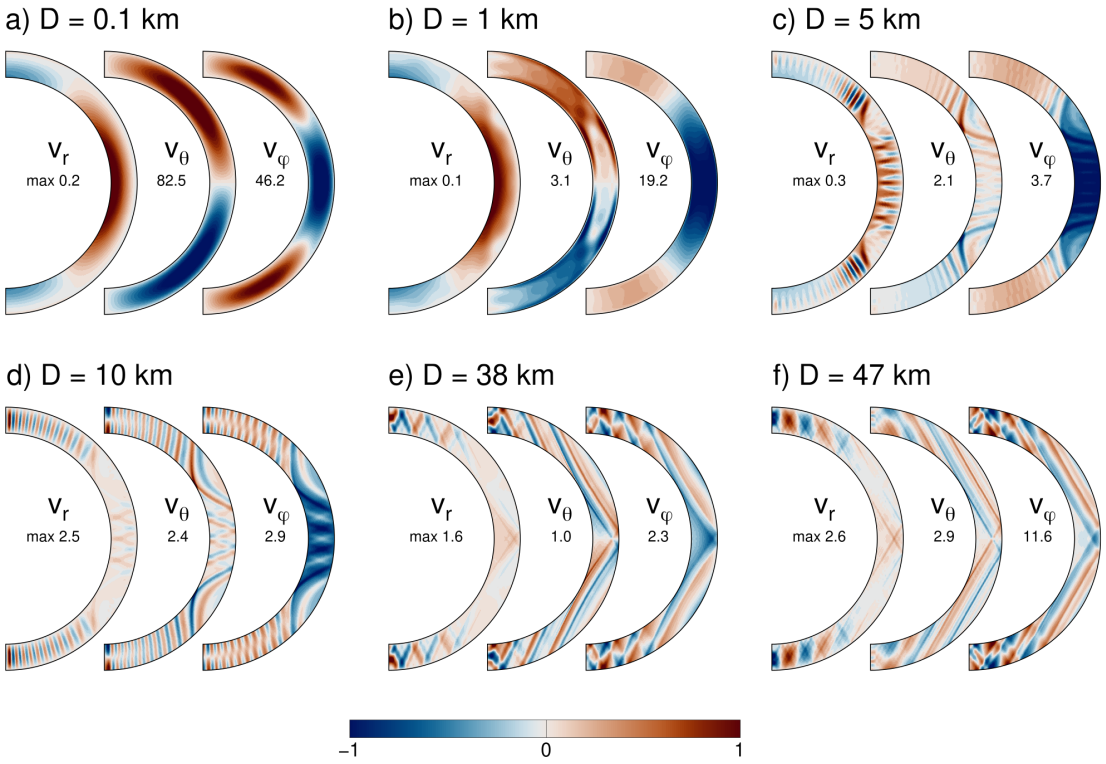



Figure 3.5: Velocity fields (components $r, \vartheta$ and $\varphi$) at time $t = 0$ obtained for $\eta_o = 100$ Pa s and $D$ ranging from 0.1 to 47 km. The fields are normalized to 1 and plotted on a meridional cross-section at longitude $\varphi = 0$. The maximum values in mm/s are given on the left-hand side of each cross-section. While the ratio $D/R_{o/c}$ varies from $5.2 \times 10^{-4}$ in panel a to 0.24 in panel f, the thickness of the ocean in the visualization is fixed at $D/R_{o/c} = 0.25$ for clarity.

for modeling Enceladus' ocean tides.

Figure 3.6 shows the same flow models as Figure 3.5 but in North pole stereographic projection. The velocity fields represented by surface streamlines are shown at a depth of $D/10$ below the ice/ocean boundary. A long-wavelength flow pattern typical of shallow water models is found only for $D \leq 5$ km. For larger values of $D$, the velocity field is dominated by small-scale concentric flow loops rotating in the azimuthal direction that cannot be obtained using the standard shallow water approach.

Previous studies of tidal flow in subsurface oceans have assumed that the non-linear term in the momentum equation ($\rho \boldsymbol{v} \cdot \nabla \boldsymbol{v}$) can be neglected or its effect can be simulated by a global increase in viscosity (i.e., by using the eddy viscosity instead of the molecular viscosity). The problem of tidal flow is then linear in $\boldsymbol{v}$, and its solution shows a marked resonant behavior characterized by a significant increase in the kinetic energy of the flow (e.g., Tyler, 2008). The question arises as to how much this behavior would be affected by the non-linear term and, in general, what role turbulence plays in tidal dissipation. One way to assess whether the flow is turbulent or not is to evaluate the Reynolds number, $Re = \rho_o |\boldsymbol{v}| D/\eta_o$, where $|\boldsymbol{v}|$ is the $L_2$ norm of the velocity field. The Reynolds number is a dimensionless quantity that is used to predict the transition from laminar to turbulent flow. Turbulent flow occurs when $Re > Re_c$ where $Re_c$ is the critical Reynolds number ($Re_c = 10^3 - 10^4$, depending on the geometry of the

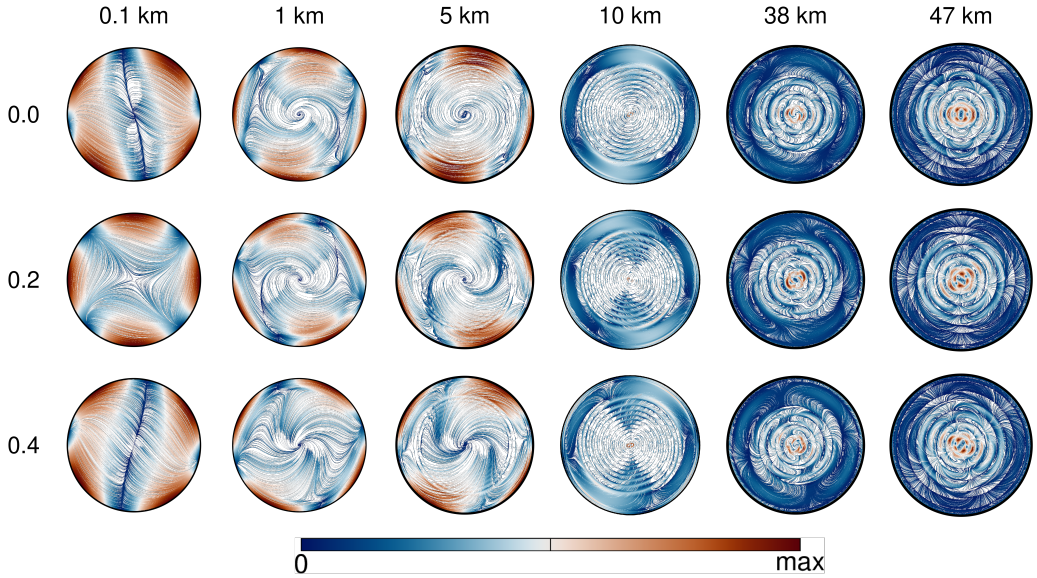



Figure 3.6: Horizontal component of the flow velocity, $\boldsymbol{v} - (\boldsymbol{v} \cdot \boldsymbol{e}_r)\boldsymbol{e}_r$, at a depth of $D/10$ below the ocean surface computed in different orbital phases ($t$ = 0, 0.2 and 0.4 $P$) for the same models as in Figure 3.5. The horizontal velocity is represented by streamlines with colors representing the flow speed. All maps are shown in the Noth pole stereographic projection.

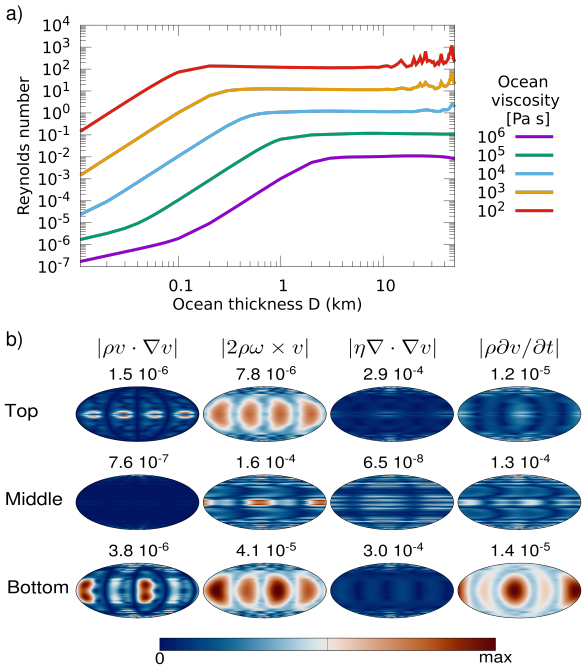



Figure 3.7: a) The Reynolds number as a function of ocean thickness evaluated for different values of viscosity $\eta_o$. b) Comparison of the terms in the Navier-Stokes equation (3.10) near the top and bottom boundaries and in the middle of the ocean for the model with $D = 38$ km and $\eta_o = 100$ Pa s. The numbers above the plots indicate the maximum values in N/m$^3$.

system). As shown in Figure 3.7a, all models presented in this study ($\eta_o \geq 100$

Pa s, $D \leq 50$ km) are characterized by low Reynolds numbers ($Re \lesssim 1000$), suggesting the dominant role of laminar flow. This conclusion is supported by a direct comparison of the terms in the Navier-Stokes equation, which is obtained by substituting $\boldsymbol{\sigma}$ from Equation (3.5) into Equation (3.2) and setting $\mu^{-1} = 0$,

$$\rho\left(\frac{\partial \boldsymbol{v}}{\partial t} + \boldsymbol{v}\cdot\nabla\boldsymbol{v}\right) = -\nabla p + \eta\nabla\cdot\nabla\boldsymbol{v} - 2\rho\boldsymbol{\omega}\times\boldsymbol{v} - \rho\left(\nabla V_t + \nabla V_g\right), \tag{3.10}$$

where $p$ is the pressure. Figure 3.7b shows that the non–linear term ($\rho\boldsymbol{v}\cdot\nabla\boldsymbol{v}$), which is responsible for turbulence, is small compared to other terms in Equation (3.10). Extrapolation of the results shown in Figure 3.7a indicates that the transition from laminar to turbulent flow occurs when the viscosity $\eta_o$ drops to about 10 Pa s, presumably leading to an increase of the Reynolds number to $10^3 - 10^4$. We are currently unable to perform time domain simulations for $\eta_o \ll 100$ Pa s because they place extreme demands on the numerical resolution required to represent the velocity fields. The problem of whether the turbulent flow can influence the resonant states predicted by the linearized model thus remains unresolved and will require further improvements of the numerical method.

## 3.5 Comparison with the LTE approach

In this section, we compare our approach with that of Beuthe (2016). To couple the flow in the ocean with the deformation of the ice shell, Beuthe (2016) formulated the Laplace tidal equations (LTE) as follows:

$$\frac{\partial \boldsymbol{u}}{\partial t} = -\frac{1}{\rho_o}\nabla_s p - 2\boldsymbol{\omega}\times\boldsymbol{u} + \boldsymbol{F}\left(\boldsymbol{u}\right), \tag{3.11}$$

$$\frac{\partial h}{\partial t} + D\nabla_s\cdot\boldsymbol{u} = 0, \tag{3.12}$$

$$p = \Delta\rho g h - \rho_o\left(V_t + V_g\right) - \sigma_{rr}. \tag{3.13}$$

Here, $\boldsymbol{u} = \boldsymbol{u}\left(\vartheta,\varphi\right)$ is the depth-averaged velocity, $\nabla_s$ is the surface gradient, $h$ is the radial displacement at the boundary between the ice shell and the ocean, $\sigma_{rr}$ is the radial component of the traction vector at the base of the ice shell, and $\boldsymbol{F}\left(\boldsymbol{u}\right)$ represents the dissipative stress

$$\boldsymbol{F}\left(\boldsymbol{u}\right) = \frac{\eta_o}{\rho_o}\Delta_s\boldsymbol{u} - \alpha\boldsymbol{u}, \tag{3.14}$$

where $\alpha$ is the linear drag coefficient, and $\Delta_s$ is the horizontal Laplace operator. Unlike the previous studies (e.g., Matsuyama, 2014; Chen et al., 2014; Tyler, 2014), the approach by Beuthe (2016) includes the stabilizing effect of the overlying shell, which damps the ocean tides and reduces the tidal heating in the ocean (see also Matsuyama et al., 2018). In the following, Equations (3.11)–(3.14) are referred to as the modified LTE.

The modified LTE approach differs from our approach, Equations (3.1)–(3.7), in two ways. First, as already mentioned above, the modified LTE approach does not include the radial component of velocity and assumes that the horizontal

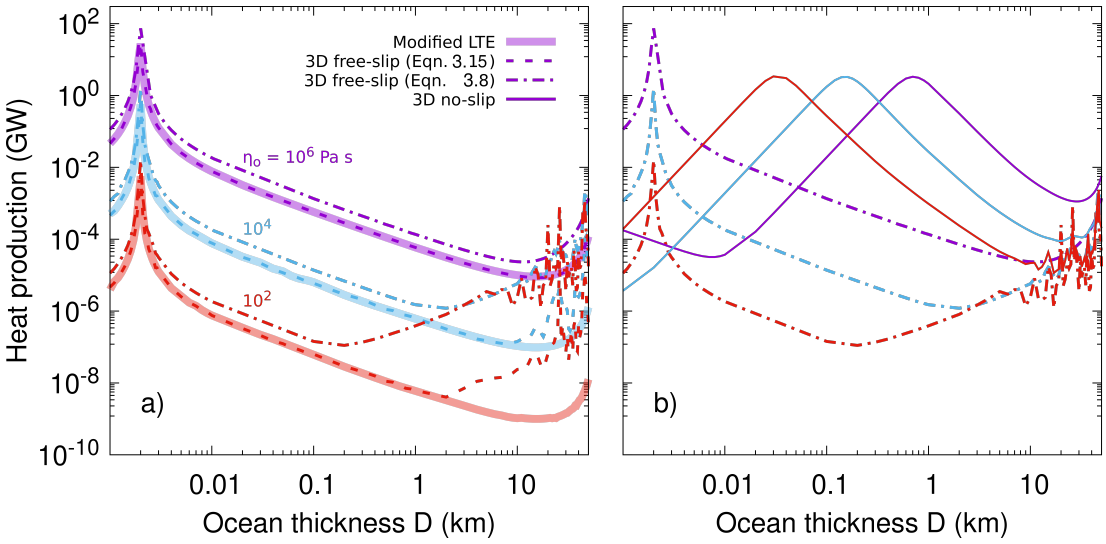



Figure 3.8: a) Dissipation as a function of the ocean thickness computed using the modified LTE approach by Beuthe (2016, thick solid lines) and the 3D approach (this study) in which the no–slip boundary conditions were replaced by the free-slip ones (dashed and dash-dotted lines). Dissipation in the 3D models is obtained using either Equation (3.8) or (3.15). The violet, blue and red colors represent different values of viscosity $\eta_o$. b) Comparison of 3D free-slip (dash-dotted lines) and 3D no-slip solutions (thin solid lines) obtained for model A (see Table 1). Colors are the same as in panel a. All the calculations are performed for model A.

velocity is a function of only $\vartheta$ and $\varphi$ (i.e., $\partial \boldsymbol{u}/\partial r = 0$). Second, the modified LTE approach guarantees that the radial components of the displacement and traction do not change across the ice/ocean boundary (Equation 3.13), but, for understandable reasons, it imposes no restriction on the horizontal components (in other words, the boundary is free-slip). In contrast, in our approach, we assume that the boundary is no-slip and both radial and horizontal components of the displacement and traction are continuous (Equation 3.7).

To facilitate the comparison of the methods, we replace the no-slip boundary condition in our model with the free-slip one and omit the last term in Equation (3.14) because the drag coefficient $\alpha$ is not included in our 3D model. The modified LTE method has been coded in Fortran 90 and tested against the results of Beuthe (2016). Unlike the original method Beuthe (2016) where the layer overlying the ocean is treated as a thin shell, the stress and displacement in the ice are obtained by solving the standard equations for thick shells (cf. Matsuyama et al., 2018). The total heat production of the 3D model can be calculated from Equation (3.8). For the sake of comparison with the modified LTE approach, we replace the velocity $\boldsymbol{v}$ in Equation (3.8) by the depth-averaged velocity, $\overline{\boldsymbol{v}}$:

$$H = \frac{2\eta\, D}{P} \int_{t_0}^{t_0+P} \int_S \dot{\bar{\boldsymbol{e}}} : \dot{\bar{\boldsymbol{e}}}\, dS\, dt, \tag{3.15}$$

where $S$ is the surface of the sphere of radius $R_{i/o}$ and $\dot{\bar{\boldsymbol{e}}} = \frac{1}{2}(\nabla_s \overline{\boldsymbol{v}} + (\nabla_s \overline{\boldsymbol{v}})^T)$. Note that $\overline{\boldsymbol{v}} = \boldsymbol{u}$ in the case of the modified LTE method.

The heat production obtained for the two methods is compared in Figure

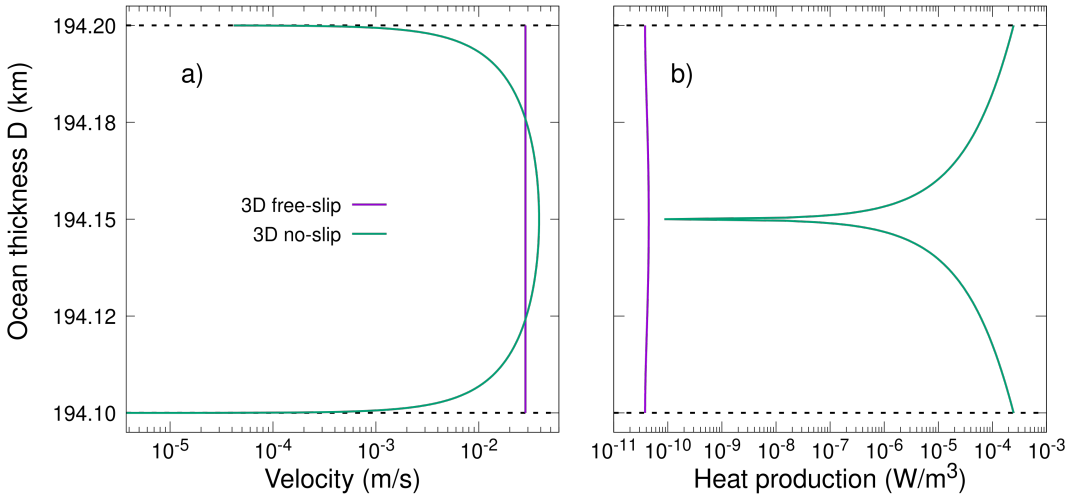



Figure 3.9: Radial variation of the mean flow velocity (a) and heat production (b) in the ocean for $D = 100$, $\eta_o = 100$ Pa s and $t = 0$. The violet and green lines represent the 3D models with the free-slip and no-slip conditions, respectively. The mean velocity is calculated as $\sqrt{\int_S |\boldsymbol{v}\,(r, \vartheta, \varphi)\,|^2\, dS}$ while the mean heat production is given by $2\eta_o S^{-1} \int_S \dot{\boldsymbol{e}} : \dot{\boldsymbol{e}}\, dS$.

3.8*a*. The calculations are performed only for model A (i.e., the model wiht a rigid core). Inspection of the figure shows that the level of agreement between the methods depends not only on the thickness of the ocean but also on the viscosity of water and on how the dissipation rate of the 3D model is calculated. Our results indicate that for the low values of the viscosity ($\eta \lesssim 100$ Pa s), the modified LTE method is only applicable to models with very thin ocean ($D \lesssim 2$ km). On the other hand, when the viscosity is high ($\eta = 10^6$ Pa s), the modified LTE method and the 3D method show good agreement over the whole range of ocean thickness.

The agreement between the LTE and 3D solutions is generally better when the heat production of the 3D model is calculated from Equation (3.15). When depth variations in velocity are included, i.e., when $H$ is calculated from Equation (3.8), the heat production increases and the difference between the modified LTE solution and 3D solution is significant even for ocean thicknesses as small as 10 m. The difference is more pronounced for models with a low viscosity ocean, ranging from a factor of 2 at $D \leq 100$ m to a factor of $10^5$ at $D = 50$ km for $\eta = 100$ Pa s. This indicates that depth variations in velocity play an important role in calculating the tidal heat production even when $D/R_{i/o} \ll 1$ (see Figure B.3 in the Appendix B.1). These variations are inherently absent in the modified LTE solution, casting doubt on the applicability of the LTE method for determining the dissipation rate in the ocean. It is also worth noting that the dissipation curves computed for 3D models where the internal interfaces are treated as free-slip boundaries are significantly different from those computed for 3D models with no-slip boundaries. To allow for a better comparison between the free–slip and no–slip solutions, the two sets of curves are shown together in Figure 3.8b.

No–slip is usually considered to be the appropriate boundary condition for a

viscous fluid in contact with a solid impermeable surface. More generally, the boundary condition can be expressed as a weighted combination of no-slip and free-slip boundary conditions:

$$v_r = 0, \tag{3.16}$$

$$(\boldsymbol{\sigma} \cdot \boldsymbol{e}_r)_\tau = -\alpha \boldsymbol{v}, \tag{3.17}$$

where the subscripts $r$ and $\tau$ denote the radial and tangential components, respectively, and $\alpha$ is the drag coefficient, which may depend on the velocity. The boundary condition (3.17) reduces to no-slip boundary condition for $\alpha \to \infty$ and to the free-slip boundary condition for $\alpha = 0$. No-slip and free-slip can therefore be considered as extreme cases.

Unlike the free-slip model, the no-slip model is characterized by the presence of velocity boundary layers, the thin layers of fluid in the vicinity of the boundaries where the flow velocity monotonically increases with the distance from the boundary (Figure 3.9a). Although the velocity far from the boundary may not be affected by the type of the boundary condition (i.e., by the presence or absence of the boundary layer), the dissipation, which depends on the gradient of velocity, is usually higher for no-slip models compared to free-slip models. Nearly all of the tidal dissipation in the no-slip models is concentrated in the boundary layers (Figure 3.9b) and even though the thickness of the boundary layers is small, the total heat production can be up to six orders of magnitude higher than in the corresponding free-slip models.

## 3.6 Conclusion

In this study, we have presented a novel approach to modeling the tidal response of icy moons with subsurface oceans. The problem of tidal deformation is solved in the time domain and the flow in the ocean is calculated simultaneously with the deformation of the core and the ice shell. The main advantage of this approach is that it makes it possible, at least in principle, to investigate the non-linear effects associated with turbulent flow. However, this advantage is also its biggest limitation: Since the time required to reach a stable periodic or quasi-periodic solution is rather long ($\sim 100 - 1000\, P$), the calculations are time-consuming and at present are only feasible for viscosities that are several orders of magnitude higher than the molecular viscosity of water.

The method developed here is used to study the tidal flow in the ocean of Enceladus. In particular, we focus on the role of a highly deformable and dissipative core in ocean dynamics and investigate the mechanical coupling between the core and the ocean. We show that the amount of tidal heat generated in the core and the ocean strongly depends on the thickness of the ocean layer. If the ocean thickness is significantly greater than 1 km, heat production is dominated by tidal dissipation in the core and the amount of heat produced in the ocean is negligible. In this case, tidal deformation of the core and crust is unaffected by tidal currents in the ocean, implying that tidal flow in the ocean can be investigated using the approach by Rekier et al. (2019) where the deformations of the

crust and core are computed beforehand and imposed as boundary conditions. In contrast, when the ocean thickness is less than about 1 km, tidal heating in the core diminishes and dissipation in the ocean increases, leaving the total heat production unchanged. The maximum heat production in the ocean depends only on the material properties of the core and may exceed 20 GW if the core is highly deformable.

We demonstrate that the flow pattern and the distribution of tidal dissipation strongly depend on the thickness of the ocean. The radial component of the velocity is found to be negligible only if the ocean thickness is less than about 5 km, implying that the shallow water approximation (Tyler, 2009, 2020) is not applicable to present-day Enceladus. The amount of small–scale content in the velocity field increases with decreasing viscosity and increasing ocean thickness, leading to complex patterns of heat flux at the surface of the ocean.

Comparison of our results with those obtained using the LTE approach by Beuthe (2016) suggests that the shallow water equations corrected for the dampening effect of the ice shell give a reasonable estimate of the horizontal flow velocity but they fail to predict the correct values of the dissipation rate. The reason for this is that the solution of these equations cannot, in principle, provide information about the radial changes of the velocity vector. We show that these changes play an important role in calculating the dissipation and may be significant even in the case of a thin ocean.

Extrapolation of our results to realistic (low viscosity) conditions indicates that the heat production in Enceladus' present-day ocean is likely to be less than 0.1 GW, corresponding to 0.25% of Enceladus' total heat loss. This suggests that the tidal dissipation in the ocean plays a minor role in Enceladus' heat budget, which is in agreement with most of the recent studies, except the one by Tyler (2020). It is unclear, however, whether such an extrapolation is justified because the models of ocean tides presented here are characterized by laminar flow (Reynolds number $\lesssim 10^3$) while the flow in the real ocean is likely to be turbulent. Based on our results, we estimate that the onset of turbulence occurs when the model viscosity drops below 10 Pa s, i.e., at a value that is still rather high compared to the molecular viscosity of water. The reader should be aware that the results presented here may be affected by the fact that our model does not include the effect of ocean thickness variations and stratification, which can significantly enhance the dissipative processes in the ocean.

The question of to what extent the non-linear effects and possible resonant interactions can influence tidal dissipation in the ocean has not been addressed in previous studies. Some of these studies (e.g., Tyler, 2014; Matsuyama, 2014; Rovira-Navarro et al., 2019; Rekier et al., 2019) have demonstrated that the solution of the linearized Navier-Stokes equation exhibits strong resonance peaks occurring when the system is able to store the tidal energy and transfer it into kinetic energy. However, the increase in the kinetic energy would likely to result in the onset of turbulence, violating the assumption of linearity, enhancing the damping properties of the system, and possibly reducing the amplitude of flow oscillations. Understanding these effects will require a thorough analysis of tidal flow at small spatial scales. This goal can hardly be achieved without the development of new numerical tools that will make it possible to perform high resolution simulations in the time domain. We believe this study is a first step

towards this goal.

# 4. Tidal heating in a subsurface magma ocean on Io revisited

This chapter was published as Aygün and Čadek (2024) in *Geophysical Research Letters*.

## 4.1 Introduction

Jupiter's moon Io is the most active volcanic body in the Solar System, with more than 400 known volcanoes, 150 of which are erupting at any given time (e.g. Schenk et al., 2001; Radebaugh et al., 2001; Veeder et al., 2012). Io's volcanic activity is driven by the heat generated by tidal friction caused by its orbital resonance with Europa and Ganymede (Peale et al., 1979). The average endogenous heat production is estimated to be of the order of 100 TW (e.g. Veeder et al., 1994; Spencer et al., 2000; Lainey et al., 2009), which is significantly more than the heat output of the Earth.

The dissipative response of the body to tidal forcing is determined by its internal structure, size and the frequency of forcing. Dissipation of tidal energy can occur in different ways, in both the solid and liquid regions of the body. In a solid material, the dissipative properties depend on the elastic moduli, the viscosity and the anelastic response, while the dissipation in a liquid is controlled by a single parameter, viscosity, varying with temperature and composition.

Physical models of solid body tides on Io usually assume that most of the heat is generated in a partially molten layer beneath Io's lithosphere or in a deeper, potentially dissipative mantle (e.g. Ross and Schubert, 1985; Segatz et al., 1988; Bierson and Nimmo, 2016; Hamilton et al., 2013; Renaud and Henning, 2018; Steinke et al., 2020; Kervazo et al., 2021). The presence of a partially molten layer in Io's upper mantle is predicted by the models of magmatic heat transfer (e.g. Moore, 2001, 2003; Steinke et al., 2020; Spencer et al., 2020) and is consistent with the estimates of eruption temperatures indicating that a substantial portion of Io's mantle is partially molten, with porosity between 3%-25% (Keszthelyi et al., 2007).

An alternative model to explain Io's heat output has been proposed by Tyler et al. (2015). The model assumes that the tidal heating is concentrated in a hypothetical magma ocean that is approximated by a fluid layer. The main difference between the solid and fluid tides is that the tidal deformation of a fluid layer is affected by the Coriolis force, an effect that is negligible in solid tide models. Tyler et al. (2015) shows that fluid-tide models predict different patterns of tidal heating than solid-tide models and can explain Io's heat production over a wide range of plausible parameters.

The existence of a magma ocean on Io was predicted by Peale et al. (1979), shortly before the Voyager 1 mission discovered Io's active volcanism (Smith et al., 1979). At the same time, the mission revealed mountains with elevations of $\sim 10$ km, suggesting that Io must have a cold lithosphere (O'Reilly and Davies, 1981) that is significantly thicker than that proposed by Peale et al. (1979). Although the concept of a mushy magma ocean was supported by geological

analysis (Keszthelyi, 1999), some scientists remained skeptical and argued that heat transport by melt segregation would lead to rapid cooling, reducing the melt fraction and preventing the formation of a magma ocean (e.g. Moore, 2001). The question of whether Io has a magma ocean was reopened in 2011 when Khurana and co-workers analyzed the magnetometer data collected by the Galileo spacecraft near Io and showed that the data were consistent with the presence of a global conductive layer. Taking into account the electrical properties of partially molten rocks, Khurana et al. (2011) interpreted this layer as a magma ocean with a thickness exceeding 50 km and a rock melt fraction of a few tens of percent. However, this model was challenged by Roth et al. (2017) and Blöcker et al. (2018) who argued that the interaction of the Jovian magnetosphere with Io's plasma environment is a more likely explanation than a magma ocean. Recently, Miyazaki and Stevenson (2022) have explored the steady state of a solid layer with a high melt fraction ("magmatic sponge" with porosity >0.2). They showed that for a wide range of parameters such a layer would be unstable and it would swiftly separate into two phases, leading to the formation of a subsurface magma ocean. Such an ocean would likely contain some amount of crystals but it would behave rheologically as a liquid. The existence of a magma ocean does not contradict the results of Roth et al. (2017) and Blöcker et al. (2018) because the magma layer may be relatively thin (∼1–10 km) and the magnetic induction signal from Io's interior may be weak compared to the magnetic field perturbations caused by the plasma interaction with Io's asymmetric atmosphere. The presence of a magma ocean on Io has recently been supported by new observations by the Juno spacecraft, which show that Io's hot spots are more or less evenly distributed over the surface, but polar volcanoes emit less energy than volcanoes at lower latitudes (Davies et al., 2024). Such a heat flux distribution cannot be explained by tidal dissipation in the deep interior, but it is consistent with the presence of a global magma ocean and/or shallow asthenospheric heating (Tyler et al., 2015; Matsuyama et al., 2022, e.g.).

In this study, we investigate the tidal dissipation in Io's hypothetical magma ocean using a new approach based on the solution of the three-dimensional Navier-Stokes equations. Unlike the study of Tyler et al. (2015), where the mechanical coupling between the ocean and the solid parts of the moon was neglected, the flow in the ocean is calculated simultaneously with the deformation of the lithosphere and the sub-oceanic mantle. The resulting maps of tidal dissipation are compared with the geological evidence and the possible role of a magma ocean in Io's thermal evolution is discussed.

## 4.2 Method

The models presented in this paper were obtained by solving the following set of equations:

$$\nabla \cdot \boldsymbol{\sigma} - 2\rho\boldsymbol{\omega} \times \boldsymbol{v} - \rho\nabla(V_\mathrm{t} + V_\mathrm{g}) = \rho\frac{d\boldsymbol{v}}{dt}\,, \tag{4.1}$$

$$\nabla \cdot \boldsymbol{v} = 0\,, \tag{4.2}$$

$$\frac{1}{\eta}\boldsymbol{\sigma}^\mathrm{d} - \nabla\boldsymbol{v} - (\nabla\boldsymbol{v})^T + \frac{1}{\mu}\frac{\partial\boldsymbol{\sigma}^\mathrm{d}}{\partial t} = \mathbf{0}\,, \tag{4.3}$$

where $\boldsymbol{\sigma}$ is the incremental stress tensor, $\rho$ is the density, $\boldsymbol{\omega}$ is the angular frequency, $V_t$ is the tidal potential, $V_g$ is the gravitational potential due to the deformation, $t$ is the time, $\boldsymbol{v}$ is the velocity, $\boldsymbol{\sigma}^{\mathrm{d}}$ is the deviatoric part of $\boldsymbol{\sigma}$, $\eta$ is the dynamic viscosity, $\mu$ is the shear modulus and $\bullet^T$ denotes the transpose of a tensor. Equation 4.1 is the momentum equation including the Coriolis force ($-2\rho\boldsymbol{\omega}\times\boldsymbol{v}$) and the time-varying tidal potential (Kaula, 1964),

$$V_t(r,\theta,\phi,t) = V_{t,20}(r,t)P_{20}(\cos\theta)+V^c_{t,22}(r,t)P_{22}(\cos\theta)\cos 2\phi+ V^s_{t,22}(r,t)P_{22}(\cos\theta)\sin 2\phi\,. \tag{4.4}$$

Here, $r$, $\theta$ and $\phi$ are the spherical coordinates, $P_{20}$ and $P_{22}$ are the associated Legendre functions, and

$$V_{t,20} = \frac{3}{2}r^2\omega^2 e\cos\omega t,\quad V^c_{t,22} = -\frac{3}{4}r^2\omega^2 e\cos\omega t,\quad V^s_{t,22} = -r^2\omega^2 e\sin\omega t, \tag{4.5}$$

where $e$ is the eccentricity and $\omega$ is the angular speed. The effect of the obliquity tides has been neglected (Baland et al., 2012). Equation 4.2 is the continuity equation for an incompressible flow. Finally, equation 4.3 is the Maxwell constitutive law for a viscoelastic body expressed in terms of velocity $\boldsymbol{v}$. In the case of $\mu\to\infty$, the equation reduces to a constitutive relation for a Newtonian fluid. We assume that the surface of the moon is free to move, the velocity and traction vectors are continuous at the internal interfaces and the core is in hydrostatic equilibrium.

Equations 4.1–4.3 are solved in the time domain using the semi-spectral method developed by Aygün and Čadek (2023). The spherical harmonic expansions are truncated at degree 20–200 depending on the viscosity of the magma ocean, while the spherical harmonic coefficients are discretized in 800 unevenly spaced radial points. The radial resolution ranges from 1 m to 50 m in the magma ocean and from 100 m to 4 km in the rest of the mantle. Tidal dissipation (heat power per unit volume) is calculated using the formula

$$h(r,\theta,\phi) = \frac{1}{P}\int_{t_0}^{t_0+P}\frac{\boldsymbol{\sigma}^d:\boldsymbol{\sigma}^d}{2\eta}dt\,, \tag{4.6}$$

where $P$ is the rotation period, $t_0$ is an arbitrary time and the symbol : denotes the Frobenius inner product ($\sigma^d_{ij}\sigma^d_{ij}$ in the Cartesian components). Equation 4.6 can be used to calculate tidal dissipation in both liquid and solid phases, provided that the solid is represented by a Maxwell viscoelastic model (Souček et al., 2016, see section 5 in SI). The total dissipation or the total heat production, $H$, is calculated as the integral of $h$ over the volume of the magma ocean. The spatial distribution of dissipation in Io's magma ocean is presented in the form of maps showing the heating $h$ integrated over the thickness of the ocean ("tidal heat flux"),

$$q(\theta,\phi) = \frac{1}{R_m^2}\int_{R_m-d}^{R_m} h(r,\theta,\phi)r^2dr\,. \tag{4.7}$$

where $R_m$ and $d$ are the outer radius and the thickness of the magma ocean, respectively.

The modeling approach used here is different from that used by Tyler et al. (2015) in two main respects. First, the tidal response of the magma ocean is

calculated by solving the three-dimensional (3D) Navier-Stokes equations, while Tyler et al. (2015) used the Laplace tidal equations (LTE) where the tidal flow is described as a barotropic two-dimensional sheet flow. Second, the response of Io to tidal loading is calculated not only in the magma ocean but also in the lithosphere and the sub-oceanic mantle, which allows us to precisely quantify the mechanical and gravitational coupling between the three layers.

Our method is also more general than the methods used in studies investigating the tidal response of water ocean worlds (e.g. Beuthe, 2016; Matsuyama et al., 2018; Rovira-Navarro et al., 2019; Rekier et al., 2019). To couple the flow in the ocean with the deformation of the crust, Beuthe (2016) and Matsuyama et al. (2018) proposed to solve the LTE together with the equations governing the viscoelastic deformation of the overlying shell. Although their method is similar at first glance to our approach, it differs from it in that the boundaries of the ocean are treated as free-slip surfaces and the flow velocity does not change with radius. As recently shown by Aygün and Čadek (2023), the method by Beuthe (2016) correctly predicts the radially averaged flow in a thin ocean layer but can lead to biased estimates of tidal heating. Unlike Beuthe (2016), Rovira-Navarro et al. (2019) and Rekier et al. (2019) determine the dissipation rate in the ocean by using the 3D Navier-Stokes equations, but assume that the deformation of the crust is not affected by the flow in the ocean and can therefore be imposed as a boundary condition at the surface of the ocean. However, this assumption is valid only if the thickness of the ocean layer is greater than about $0.01R_m \approx 15$ km, i.e., outside the thickness range considered in the present study (Aygün and Čadek, 2023).

The density structure of Io is chosen to match the total mass ($8.9319{\cdot}10^{22}$ kg) and MoI factor (0.37685, Anderson et al., 2001) and to satisfy constraints on its material composition (Anderson et al., 1996b). The upper boundary of the magma ocean is set to a depth of 30 km and the thickness of the ocean is varied from 100 m to 10 km. We assume that the magma behaves as a Newtonian liquid and its viscosity is constant throughout the ocean. The viscosity of the magma ranges from 100 Pa s (hot mafic magma) to $10^7$ Pa s (low-temperature magma with solid crystals suspended in the liquid phase, see, e.g., Philpotts and Ague (2009)). For simplicity, we assume that the density of the magma is the same as the density of the mantle (for details, see Table B.1 in the Appendix B.2).

The lithosphere and the mantle below the ocean are assumed to behave as a Maxwell viscoelastic solid. Since the main focus of this study is to examine tidal heating in a hypothetical magma ocean, the material parameters of the lithosphere and the sub-ocean mantle are chosen so that the tidal heat production outside the magma ocean is much smaller than Io's current heat output.

## 4.3 Results

As illustrated in Figure 4.1, the tidal flow in the magma ocean produces a wide variety of heating patterns and even small changes in ocean thickness can lead to order of magnitude changes in the total heat production. The heat flux distributions are symmetric about the equator and most of them, but not all, also about the tidal axis. The heat flux patterns are dominated by dissipation at low latitudes, typical of fluid models. The highest heat production ($> 10^4$ TW) is found

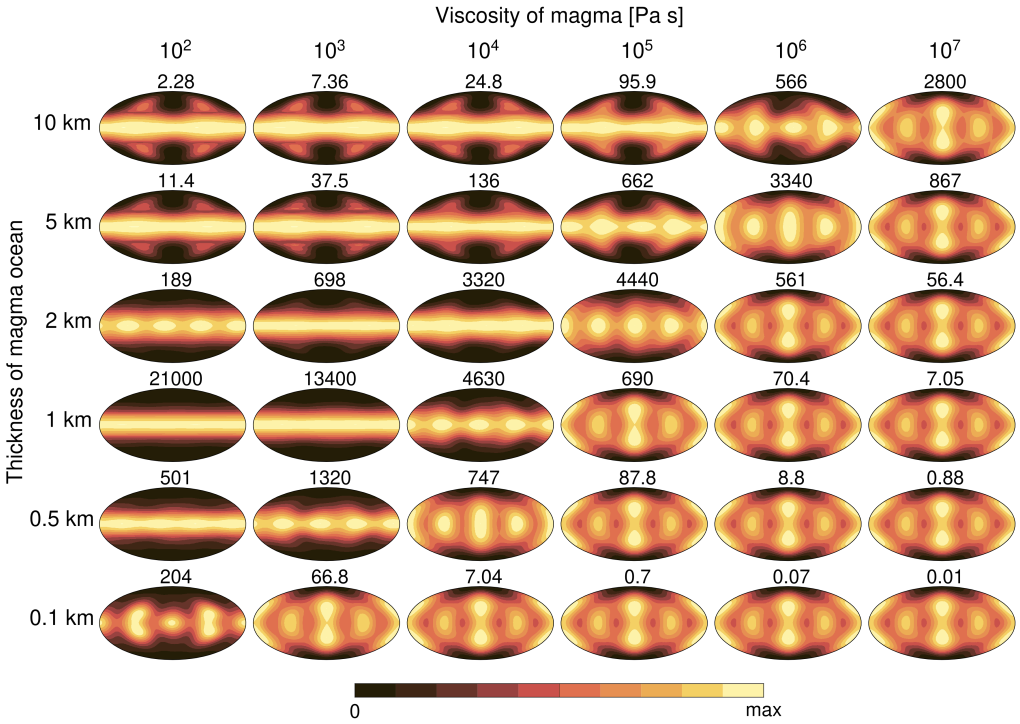



Figure 4.1: Distribution of tidal dissipation in the magma ocean, equation 4.7, evaluated for different thicknesses and viscosities of the ocean (Mollweide equal-area projection centered on 180° W longitude). The numbers above each map represent the total heat production of the magma ocean in TW.

in the case where tidal heating is concentrated in an equatorial zone at latitudes below 30°. This equatorial zone is clearly separated from the low-dissipation regions at higher latitudes and its position shows a remarkable correspondence with Io's yellow bright plains (see Figure 4.2 below Williams et al., 2011). The purely zonal character of dissipation (i.e., independent of the longitude) is unusual in the context of eccentricity tides and, to our knowledge, has not been reported in previous studies of tidal flow in subsurface (water or magma) oceans (e.g. Chen et al., 2014; Tyler et al., 2015; Matsuyama et al., 2018, 2022; Hay and Matsuyama, 2019a), except for a study including the moon-moon tidal interaction (Hay et al., 2020, based on the communication with Hamish Hay). Although the zonal distribution of dissipation is obtained for models with a thin ocean ($d \approx 1$ km), the velocity field has a strong radial component ($v_r/v_\theta \approx v_r/v_\phi \approx 0.2$) that cannot be found by solving the LTE. The dependence of tidal heating on the thickness of the ocean and the viscosity of magma is shown in Figure 4.2a. Inspection of the figure shows that the heat power of $\sim 100$ TW (Io's observed heat output) is exceeded over a wide range of magma viscosities and ocean thicknesses, with maximum values achieved for $d \approx 1$ km and $\eta$ between $10^2$ and $10^4$ Pa s. When $d$ is significantly larger than 1 km, the 100 TW limit can only be achieved for $\eta > 10^4$ Pa s. The results in Figure 4.2a are qualitatively similar to those obtained from the solution of the Laplace tidal equations (Figure 4a in Tyler et al., 2015) but they differ in three minor respects: First, the ocean thickness for which the maximum dissipation is reached is about twice the value predicted by Tyler et al. (2015), second, no dissipation maxima are found for $d < 1$ km and third, the dissipation in the ocean vanishes when $d \to 0$. As illustrated in Figures 4.2b and

c, the models of magma ocean tides cannot explain the observed distribution of Io's hot spots. Most of the models satisfactorily explain the hot spots at latitudes below 50° but do not account for hot spots in the polar regions.

The tidal heating models discussed above were obtained under the assumption that Io's solid layers are only weakly dissipative. In the Appendix B.2, we also show the results obtained for the case where the magma ocean is underlain by a 100-km thick, low viscosity "magmatic sponge" layer. Comparison of Figure 4.1 with Figure B.4 in Appendix B.2 indicates that the total dissipation in the ocean is only weakly sensitive to the viscosity of the sub-oceanic mantle.

The origin and the distribution of tidal heating within Io's interior remain a subject of debate. The question could, in principle, be answered by a dedicated mission making close flybys of Io and providing new information about Io's gravity signature. Bierson and Nimmo (2016) have demonstrated that the tidal Love number $k_2$ of Io is highly sensitive to the presence of a fluid layer beneath the surface. The value of $k_2$ should be about 0.5 for Io with a fluid magma ocean and 0.1 if Io's mantle behaves as a solid (see also Kervazo et al., 2022). The first value should be regarded as a rough estimate because it was obtained under the assumption that the dynamic effect of the tidal flow in the ocean can be neglected.

In the absence of a fluid magma ocean, the gravitational response of Io to tidal forcing can be expressed as $V_g(a, \theta, \phi, t) = k_2 V_t(a, \theta, \phi, t - \Delta t_2)$, where $a$ is Io's radius, $V_t$ is the tidal potential (equation 5.4) and $\Delta t_2$ is the time lag. The response is described by only two parameters, $k_2$ and $\Delta t_2$. If Io has a fluid magma ocean, the tidal deformation generates a degree-2 flow in the ocean, which is further modulated by the Coriolis effect. Depending on the parameters of the model, the resulting flow can deform the surface and internal density interfaces, generating a gravitational signal that is much more complex than in the case of a solid body. The gravitational response at degree 2 varies with the harmonic order and is described by six parameters, $k_{20}$, $k^c_{22}$, $k^s_{22}$, $\Delta t_{20}$, $\Delta t^c_{22}$ and $\Delta t^s_{22}$, which can be determined from the following equations (cf. equation 5.4):

$$V_{g,20}(a,t) = k_{20} V_{t,20}(a, t - \Delta t_{20}), \tag{4.8}$$

$$V^c_{g,22}(a,t) = k^c_{22} V^c_{t,22}(a, t - \Delta t^c_{22}), \tag{4.9}$$

$$V^s_{g,22}(a,t) = k^s_{22} V^s_{t,22}(a, t - \Delta t^s_{22}), \tag{4.10}$$

where $V_{g,20}$, $V^c_{g,22}$ and $V^s_{g,22}$ are the coefficients of the gravitational potential induced by tidal potential coefficients $V_{t,20}$, $V^c_{t,22}$ and $V^s_{t,22}$, respectively.

In the case of solid-body tides, $k_{20} = k^c_{22} = k^s_{22} = k_2$ and $\Delta t_{20} = \Delta t^c_{22} = \Delta t^s_{22} = \Delta t_2$. On the other hand, if Io has a magma ocean, the degree-2 Love numbers and time delays can significantly vary with the order ($m = 0, 2$). While $k_{20}$ increases with the increasing ocean thickness, reaching a maximum of 0.85 for $d = 10$ km and $\eta = 3 \cdot 10^6$ Pa s (Figure 4.3a), $k^c_{22}$ and $k^s_{22}$ (Figure 4.3b,c) are strongly affected by the Coriolis effect and correlate with the total heat production (cf. Figure 4.2a). The maximum values of $k^c_{22}$ and $k^s_{22}$ are about ten times greater than the maximum value of $k_{20}$. Large differences are also found between $\Delta t_{20}$ on one side and $\Delta t^c_{22}$ and $\Delta t^s_{22}$ on the other. The values of the tidal Love numbers and time lags corresponding to Io's current dissipative power ($\approx 100$ TW) are shown by the red lines. If the ocean thickness is small and/or the magma viscosity is high, $k_{20} \approx k^c_{22} \approx k^s_{22} < 0.1$ and $\Delta t_{20} \approx \Delta t^c_{22} \approx \Delta t^s_{22} < 2$ h, suggesting that,

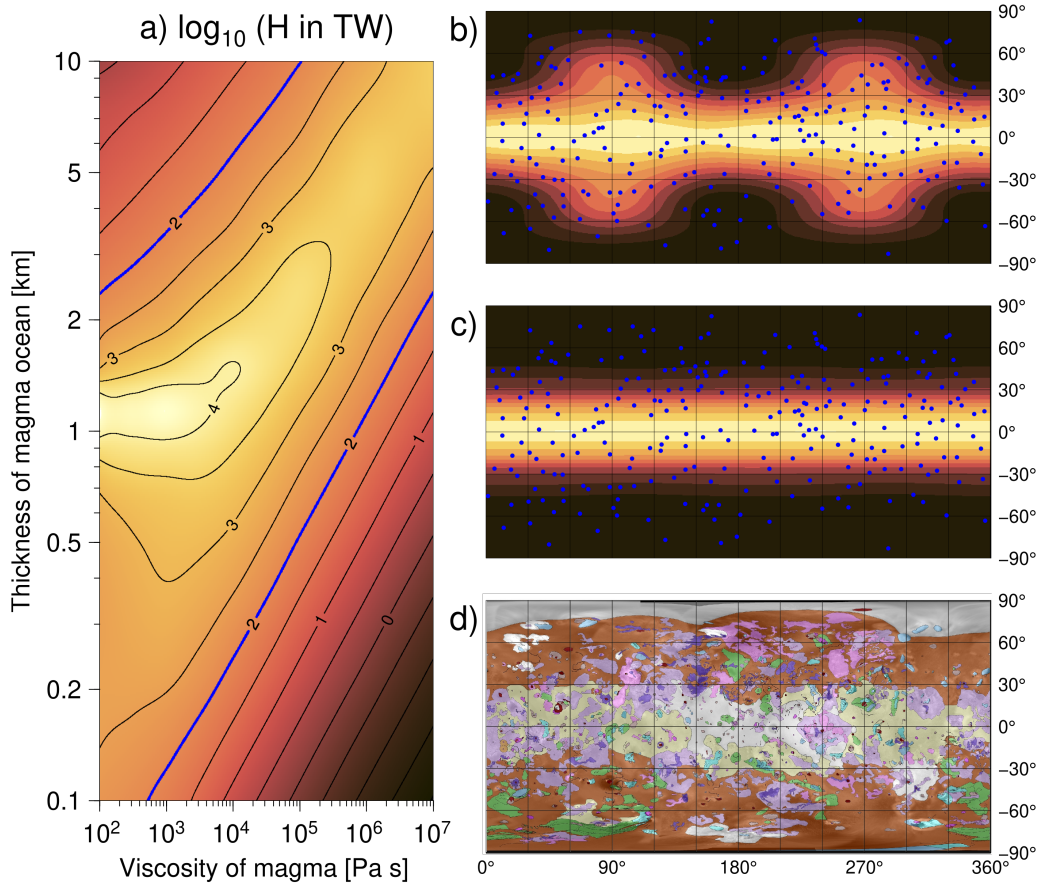



Figure 4.2: a) Total heat production in the magma ocean as a function of ocean thickness and magma viscosity. The contours plotted in blue correspond to Io's present-day heat production (100 TW). b) Heat flux map calculated for $\eta = 10^5$ Pa s and $d = 10$ km. While the total heat production (96 TW) is compatible with the observation, the dissipation pattern shows no relationship with the current distribution of hot spots (blue circles), as only a half of the hot spots are located in a region of higher-then-average heat flux. c) Heat flux map corresponding to the model with the highest dissipation ($2.1 \cdot 10^4$ TW). In this case, only about 35% of hot spots are located in high dissipation regions. d) Geological map of Io (Williams et al., 2011). For the sake of comparison with the geological map, the tidal heat flux in panels b and c is shown in the equidistant cylindrical projection. The color scale is the same as in Figure 4.1. The locations of hot spots are taken from table S1 in Davies et al. (2024).

in this case, the presence of a magma ocean has little effect on the large-scale deformation of the lithosphere.

## 4.4 Discussion and conclusions

Our results confirm the conclusion of Tyler et al. (2015) that the tidal heating in a fluid magma ocean can explain Io's observed heat production over a broad range of magma viscosities and ocean thicknesses. Compared to the studies using the LTE method (Tyler et al., 2015; Matsuyama et al., 2022), the solution of the Navier-Stokes equations is characterized by a greater variety of heat flux patterns, which vary depending on the parameters of the ocean. The highest heat production is found for models with a thin (∼1 km thick) fluid layer and low ($< 10^4$ Pa s) viscosity. The total heat production decreases with the ocean thickness (Figure 4.2a) suggesting that the thickness of the ocean (if it exists) is likely to be less than ∼10 km. An extrapolation of the results indicates that a thick (∼50 km) magma ocean is only weakly dissipative unless the viscosity of magma is higher than $10^8$ Pa s.

It is tempting to speculate that the formation of a magma ocean may have been triggered by a temporary increase in Io's eccentricity (Hussmann and Spohn, 2004), resulting in the enhancement of tidal heating and an increase of porosity in a magmatic sponge. The subsequent formation of a shallow ($\sim 0.1 - 1$ km thick) magma ocean (Miyazaki and Stevenson, 2022) led to a sharp increase of the tidal dissipation rate in Io's interior, especially at low ($< 30°$) latitudes (Figure 4.2c). Due to a positive feedback between temperature and tidal dissipation, the magma production rate was faster than the rate of magma extraction, leading to an increase in the magma ocean thickness and a gradual change in the dissipation pattern (Figure 4.1). Since dissipation in the ocean decreases with the ocean thickness (Figure 2a), the total heat production gradually stabilized at the present level. A subsequent decrease in eccentricity did not necessarily lead to the disappearance of the ocean because once the ocean is formed, the heat production in the magma layer is high enough to maintain it in a liquid state.

The question of whether present-day Io has a magma ocean or not is difficult to answer. It is usually assumed that the Io's volcanic activity should be correlated with the distribution of tidal heating. Magma ocean models (Figure 4.1) predict enhanced tidal heating at low latitudes and low tidal heating in the polar regions. However, new data from the Juno mission indicate that the density of hot spots does not decrease towards the poles (Zambon et al., 2023; Davies et al., 2024), in contrast to previous data sets where most of the hot spots were located at low latitudes (e.g. Davies et al., 2015). The low correlation between the hot spots and the predicted tidal heating at high latitudes does not necessarily mean that there is no magma ocean on Io. If the ocean is global (i.e., if the magma is stored in a global continuous reservoir), the melt is present everywhere beneath the lithosphere, and the amount of magma that gets to the surface then depends on the local conditions, rather than on the distribution of tidal heating. In other words, volcanic eruptions can occur at any location where conditions in the lithosphere are favorable for the ascent of magma (Crisp, 1984; Jaeger et al., 2003; de Kleer et al., 2019). New observations of Io's thermal emission by the Juno spacecraft Jovian Infrared Auroral Mapper suggest that polar hot spots emit less

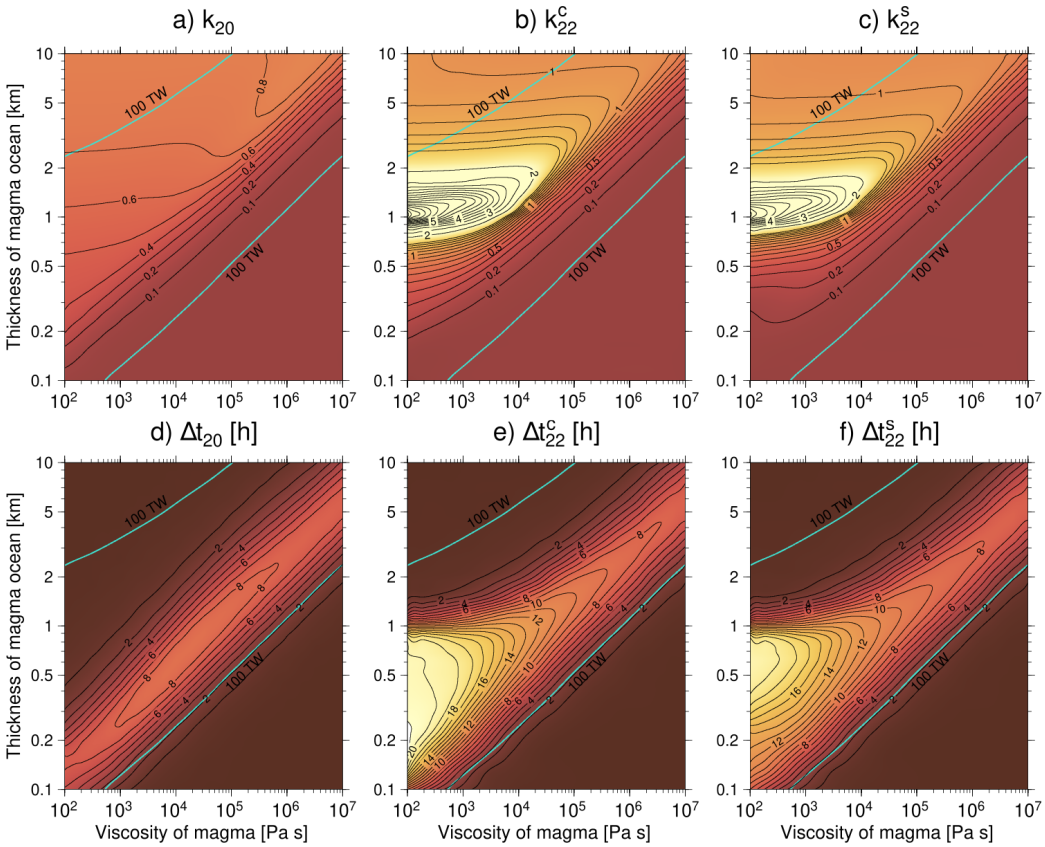



Figure 4.3: Tidal Love numbers (a–c) and time lags (d–f) as functions of the ocean thickness and magma viscosity. The blue lines correspond to models with a heat output of 100 TW. The contour interval in panels a–c is 0.1 if the Love number is less than 1.5 and 0.5 if the Love number is greater than or equal to 1.5. The contour interval in panels d–f is 2 hours.

energy than hot spots at lower latitudes (Davies et al., 2024). This finding is consistent with the presence of a magma ocean, although enhanced tidal heating at low latitudes can also be predicted by models with a dissipative asthenosphere (e.g. Tyler et al., 2015; Kervazo et al., 2021; Matsuyama et al., 2022).

Another possible explanation for hot spots in polar regions is the tidal heating in the solid sub-oceanic mantle (Tyler et al., 2015). Unlike dissipation in a liquid ocean, which is concentrated at low latitudes, dissipation in the deep mantle mainly occurs near the poles (e.g. Beuthe, 2013) and, therefore, it can compensate for the decrease in ocean tidal heating at high latitudes. If this is the case, the current distribution of hot spots on Io results from the combined effect of solid and fluid tidal dissipation (see also Figure B.5 in Appendix B.2). However, the question is whether the heat flux obtained in this way is physically meaningful because the temperature field in Io's deep mantle is likely to be affected by convection (Tackley, 2001b,a) and the heat transfer between the solid mantle and the liquid magma ocean can be modulated by the solid-liquid phase transition (e.g. Labrosse et al., 2018). As shown by Steinke et al. (2020), mantle convection tends to significantly reduce the lateral temperature signal, depending on the thickness of the convective layer, the viscosity and the mode of heat transfer. Finally, it is possible that the magma ocean has a variable thickness

and may even be absent in some areas. Dissipative behavior of such an ocean is difficult to predict but it is likely that tidal heating would strongly vary laterally and would be affected by regional resonance effects.

Bierson and Nimmo (2016) suggested that the presence of a fluid magma ocean on Io could be detected by measuring the tidal Love numbers. Our results indicate that if tidal heating preferentially occurs in a magma ocean and the total heat production is about 100 TW, then the degree-2 Love numbers are either less than 0.1 if $d < 2$ km (i.e., about the same as in the case of solid tides) or greater than 0.7 if $d > 2$ km. While in the former case, $k_{22}^c \approx k_{22}^s \approx k_{20}$, in the latter case, $k_{22}^c$ and $k_{22}^s$ are twice as big as $k_{20}$. In both cases the time lag is less than 2 hours. The fact that the tidal Love numbers are not sensitive to the presence of a liquid magma ocean if the ocean thickness is small needs to be taken into account in future analyses of Io's gravity signature.

# 5. Love numbers for Io with a magma ocean

This chapter was published as Aygün and Čadek (2025) in *Icarus*.

## 5.1 Introduction

The heat power produced by tidal dissipation in Io's interior is estimated to be about 100 TW (Moore et al., 2007; Lainey et al., 2009). Dissipation can occur in the whole silicate mantle or it can be concentrated either in a partially molten layer beneath the lithosphere (hereinafter referred to as "the asthenosphere"), or in a liquid "magma ocean". New data from the Juno mission show that Io's hotspots are more or less evenly distributed over the surface but volcanoes at low latitudes emit more heat than volcanoes in polar regions (Davies et al., 2024; Pettine et al., 2024). As shown by numerical models, such a heat flux pattern is typical of tidal dissipation in a shallow liquid or solid layer, while the dissipation in the deep interior is characterized by the increase of the heat flux towards the poles (Tyler et al., 2015; Hay et al., 2020; Kervazo et al., 2021; Matsuyama et al., 2022).

The asthenosphere can contain a significant fraction of melt but it acts as a solid on the macroscopic scale and its tidal deformation is usually modeled in the framework of the linear viscoelastic theory. In contrast to the asthenosphere, the magma ocean acts as a viscous liquid although it can contain some amount of crystals. The flow of the magma can be affected by the Coriolis effect and may exhibit resonances characterized by a significant increase of the kinetic energy and dissipation (Tyler et al., 2015; Hay et al., 2020, 2022; Aygün and Čadek, 2024). Resonance occurs when the ocean is able to absorb the tidal energy and transfer it into the kinetic energy of tidally-induced inertial and gravity waves (for a detailed discussion of this effect, see, e.g., Rovira-Navarro et al., 2019). The evaluation of tidal dissipation in the magma ocean requires the solution of the Navier-Stokes equations (NSE) or the Laplace tidal equations (LTE) if the horizontal length scale is much greater than the vertical length scale (for a comparison of the two approaches in terms of energy dissipation, see, e.g., Aygün and Čadek (2023)). It is worth noting that, in the last two decades, the tidal flow in subsurface liquid oceans has been intensely studied in the context of icy satellites. The LTE approach was used, e.g., by Tyler (2008), Chen et al. (2014), Beuthe (2016), Matsuyama et al. (2018), Hay and Matsuyama (2019a) and Hay et al. (2020), while three-dimensional models of tidal flow based on the NSE approach were presented by Rovira-Navarro et al. (2019), Rekier et al. (2019) and Aygün and Čadek (2023).

Numerical simulations of tidal dissipation provide important constraints on the thickness and the material parameters of the dissipative layer, but they do not tell us which hypothesis is correct, as both models can explain Io's observed heat output (Tyler et al., 2015; Kervazo et al., 2021; Aygün and Čadek, 2024). The presence of a global partially or fully molten layer can, in principle, be detected by satellite magnetic measurements because the electrical conductivity

of the melt is significantly higher than that of the solid rock. Based on the analysis of the magnetometer data collected by the Galileo spacecraft near Io, Khurana et al. (2011) suggested that there exists a global conductive layer with a thickness over 50 km and a rock melt fraction of a few tens of percent (for an alternative interpretation of the data, see Roth et al. (2017) and Blöcker et al. (2018)). However, the model of Khurana et al. (2011) does not tell us whether this layer is a partially molten solid (a "magmatic sponge"), or a liquid magma ocean, or a combination of both, for example, a thin layer of liquid magma above a partially molten asthenosphere (Miyazaki and Stevenson, 2022). The concept of a thin (<10 km) magma ocean has recently been supported by the numerical simulations of the flow in Io's magma ocean, which indicate that a 50 km thick magma ocean with realistic viscosity cannot explain the observed heat power of ∼100 TW (Aygün and Čadek, 2024). On the other hand, if the thickness of the liquid layer is less than about 2 km and the viscosity of the magma is less than $10^4$ Pa s, the tidal dissipation in the ocean can be strongly enhanced by a resonance phenomenon, leading to a much larger heat power ($10^3$–$10^4$ TW) than the present one

The degree of melting in Io's interior can be estimated from the temperature of the erupted magma. The interpretation of Galileo data suggested eruption temperatures up to 1450 °C (Keszthelyi et al., 2007), indicating either very high degrees of melting, refractory source regions, or intensive viscous heating on ascent (Spencer et al., 2020). High eruption temperatures are compatible with the concept of a mafic ocean (Breuer et al., 2022) but they can also be explained by a model that assumes that the hot magma originates in a refractory lower mantle (Spencer et al., 2020).

A promising way to address the ambiguity outlined above is to measure the response of Io to the external forces and torques. The main difference between the solid and liquid tides is that the flow in a fluid layer is affected by the Coriolis force, an effect that is negligible in a solid layer. The presence of a liquid magma ocean can weaken the mechanical coupling between the lithosphere and the sub-oceanic mantle, leading to a stronger gravitational response of the lithosphere to tidal forcing and a larger libration amplitude compared to the case without an ocean (Bierson and Nimmo, 2016; Hoolst et al., 2020). The variations of the gravitational potential due to diurnal tides can be measured by radio science instruments during a spacecraft flyby and are usually expressed in terms of the tidal Love number $k_2$. Previous modeling studies have suggested that $k_2 \lesssim 0.1$ if the silicate mantle is solid (Bierson and Nimmo, 2016; Kervazo et al., 2022) and greater than about 0.5 if Io has a magma ocean (Bierson and Nimmo, 2016; Hoolst et al., 2020; Kervazo et al., 2022). However, the latter value should be taken with caution because it was obtained under the assumption that the dynamic effect of the tidal flow in the magma ocean is negligible.

Aygün and Čadek (2024) have recently used the NSE approach to study the tidal deformation of Io with a thin (0.1–10 km) magma ocean located at a depth of 30 km. Varying the thickness of the ocean, $d$, and the viscosity of the magma, $\eta$, they found that the observed heat power of 100 TW can be explained either by models with $d < 2$ km and $\eta > 10^3$ Pa s (satisfying the relationship $d = 0.014\eta^{0.32}$, where $d$ is in km) or by models with $d > 2$ km and $\eta < 10^5$ Pa s ($d = 0.72\eta^{0.23}$). The models of the first group predict $k_2 < 0.1$ and therefore

cannot be distinguished from models with a solid asthenosphere. The models of the second group predict $k_2 > 0.7$ and the gravitational signal is affected by the Coriolis effect, which is negligible in solid tide models. The Coriolis effect is manifested by the dependence of $k_2$ on the harmonic order and by the nonzero spherical harmonic coefficients of the gravitational potential at degrees higher than 2 (see also Hay et al., 2022). The ratio $k_{22}/k_{20}$, where the second subscript denotes the harmonic order, ranges from 1 to 1.5 for the models predicting the observed heat power of 100 TW but can exceed 5 if the amplitudes of the tidally-induced waves are amplified by resonance and the total power is greater than $10^3$ TW.

The data collected by the Juno spacecraft during two recent flybys of Io has allowed, for the first time, to quantify Io's tidal deformation. The analysis of the data by Park et al. (2024a) reveals that $k_2$ is about 0.125, suggesting that Io does not possess a shallow global magma ocean and has a mostly solid mantle. Although the observed $k_2$ can also be explained by a thin ($< 2$ km) magma ocean, as suggested by Aygün and Čadek (2024), this possibility is viewed as unlikely because it would contradict the existence of Io's long-wavelength surface topography (White et al., 2014). While the existence of a shallow magma ocean is unlikely, Park et al. (2024a) demonstrate that the observations do not exclude the possibility that a magma ocean exists in the deep mantle, at a depth of $\gtrsim 320$ km. Such an ocean might resemble the magma ocean formed at the base of the mantle early in the Earth's history, but it is unlikely that it could be the source of Io's volcanic activity.

In this study, we build on our previous work to examine how Io's gravitational response to tidal forcing depends on the thickness of the solid layer above the ocean and how much it is affected by the Coriolis force, an effect that was not included in the study of Park et al. (2024a). Unlike the study of Aygün and Čadek (2024), which focused on a shallow magma ocean, we compute the $k_2$ Love numbers and phase lags for models with a magma ocean located at a depth of up to 400 km and demonstrate that the presence of a deep magma ocean can be constrained by comparing degree 2 zonal and sectorial Love numbers.

## 5.2 Method

We investigate the deformation of a moon subjected to diurnal eccentricity tides. The moon consists of four layers: a lithosphere, a liquid magma ocean, a solid sub-oceanic mantle, and a liquid core. For simplicity, we assume that the material forming the moon is incompressible, the interfaces between the layers are spherical and the effect of viscous flow in the core on the tidal deformation is negligible. The deformation of the moon is obtained by simultaneously solving the Navier-Stokes equations in the magma ocean, the equations governing the viscoelastic response in the lithosphere and the sub-oceanic mantle, and the Poisson equation for the gravitational potential in the whole computational domain (for details, see Aygün and Čadek, 2023). The surface of the moon is free to move and the boundary conditions at the internal boundaries are formulated to ensure the continuity of the traction and velocity vectors. The problem is solved in the time domain by the semi-spectral method developed by Aygün and Čadek (2023). Depending on

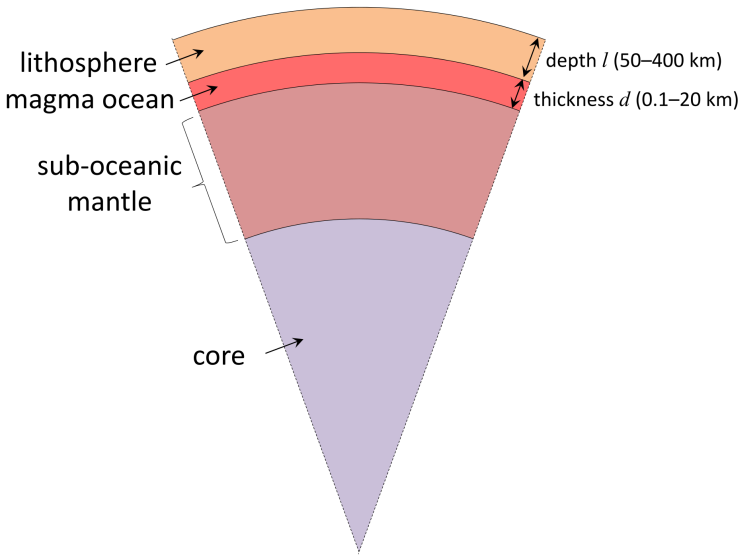



Figure 5.1: Sketch of Io's structure. The magma ocean is described by three parameters: the depth to the ocean, $l$, the thickness, $d$, and the viscosity of the magma, $\eta$.

the thickness and viscosity of the magma ocean, the spherical harmonic series are truncated at degree and order 20–200. The coefficients in the harmonic series are discretized in the radial direction on an uneven grid consisting of 800 Chebyshev nodes. The radial resolution ranges from 1 m to 50 m in the magma ocean and from 100 m to 4 km in the lithosphere and the sub-oceanic mantle.

The lithosphere and the sub-oceanic mantle are treated as a Maxwell viscoelastic material. The viscosities of these two layers are set to $10^{23}$ Pa s and $10^{20}$ Pa s, respectively, while the shear modulus is fixed at 60 GPa. The density profile is similar to that used by Kervazo et al. (2021). We assume that the crust is 30 km thick and has a density of 3000 kg/m$^3$. The density of the core is set to 5165 kg/m$^3$, in agreement with the Fe-FeS composition (Anderson et al., 1996b). The density of the mantle (3272 kg/m$^3$) and the radius of the core (950 km) are determined to match the total mass and the MOI factor (Anderson et al., 2001).

The magma ocean is characterized by three parameters: the thickness, $d$, the viscosity of the magma, $\eta$, and the thickness of the solid layer above the ocean, $l$ (Fig. 5.1).

We assume that the viscosity is not affected by the uneven distribution of tidal heating and is constant throughout the ocean (for the effect of laterally variable parameters, see Rovira-Navarro et al. (2024)). To understand how the tidal response of the moon depends on the above parameters, we vary $d$, $\eta$ and $l$ in the range $0.1 - 20$ km, $10^2 - 10^7$ Pa s and $50 - 400$ km, respectively, and for each combination of parameters, we calculate the distribution of tidal heating (see Eqs. (6) and (7) in Aygün and Čadek (2024)) and the gravitational potential induced by tidal deformation. Following the study by Aygün and Čadek (2024), we describe the degree-2 response of Io by 6 parameters, $k_{20}$, $k_{22}^c$, $k_{22}^s$, $\Delta t_{20}$, $\Delta t_{22}^c$

and $\Delta t^s_{22}$, which can be determined from the following equations:

$$\begin{aligned} V_{g,20}(a,t) &= k_{20} V_{t,20}(a, t - \Delta t_{20}), && (5.1)\\ V^c_{g,22}(a,t) &= k^c_{22} V^c_{t,22}(a, t - \Delta t^c_{22}), && (5.2)\\ V^s_{g,22}(a,t) &= k^s_{22} V^s_{t,22}(a, t - \Delta t^s_{22}), && (5.3) \end{aligned}$$

where $a$ is the radius of Io, and $V_{g,20}$, $V^c_{g,22}$ and $V^s_{g,22}$ are the spherical harmonic coefficients of degree-2 representing the gravitational potential induced by the tidal potential

$$\begin{aligned} V_t(r,\theta,\phi,t) = V_{t,20}(r,t) P_{20}(\cos\theta) + V^c_{t,22}(r,t) P_{22}(\cos\theta)\cos 2\phi \\ + V^s_{t,22}(r,t) P_{22}(\cos\theta)\sin 2\phi\,. \end{aligned} \tag{5.4}$$

In Eq. (5.4), $r$, $\theta$ and $\phi$ denote the spherical coordinates, $t$ is the time, $P_{20}$ and $P_{22}$ are the associated Legendre functions, and

$$V_{t,20} = \frac{3}{2} r^2 \omega^2 e \cos\omega t, \quad V^c_{t,22} = -\frac{3}{4} r^2 \omega^2 e \cos\omega t, \quad V^s_{t,22} = -r^2 \omega^2 e \sin\omega t, \tag{5.5}$$

where $\omega$ is the angular velocity and $e$ is the eccentricity.

In the case of the solid-body tides, $k_{20} = k^c_{22} = k^s_{22} = k_2$ and $\Delta t_{20} = \Delta t^c_{22} = \Delta t^s_{22} = \Delta t_2$, where $k_2$ is the standard degree-2 Love number and $\Delta t_2$ is the time lag. Note that in the study of Park et al. (2024a), the gravitational tidal Love number was determined under the assumption that its value does not depend on the harmonic order, and the tidal response was quantified by a complex number $\tilde{k}_2 = \mathrm{Re}(\tilde{k}_2) + i\mathrm{Im}(\tilde{k}_2)$ related to $k_2$ and $\Delta t_2$ as follows:

$$\begin{aligned} \mathrm{Re}(\tilde{k}_2) = k_2 \cos\omega\Delta t_2\,, \quad \mathrm{Im}(\tilde{k}_2) = k_2 \sin\omega\Delta t_2 = \frac{|\tilde{k}_2|}{Q}\,, \\ \Delta t_2 = \omega^{-1} \arctan\left(\frac{\mathrm{Im}(\tilde{k}_2)}{\mathrm{Re}(\tilde{k}_2)}\right)\,, \end{aligned} \tag{5.6}$$

where $Q$ is the tidal dissipation parameter. For the sake of consistency with our previous work, we represent the observed Love number in terms of $k_2$ and $\Delta t_2$. To compare our results with the values presented by Park et al. (2024a), we use $k_2 \approx \mathrm{Re}(\tilde{k}_2) = 0.125 \pm 0.047$ and $\Delta t_2 = 2129.6 \pm 677$ s.

## 5.3 Results

The results are summarized in Fig. 5.2 where we show the tidal heat production and the Love numbers plotted as a function of viscosity $\eta$ and ocean thickness $d$ for different values of depth $l$. Inspection of the plots in the left column suggests that, for a fixed viscosity and depth, there are two ocean thicknesses that predict Io's current heat production. For instance, if the ocean is at a depth of 100 km below the surface and the magma viscosity is $10^4$ Pa s, the 100 TW power is obtained for an ocean thickness of either 0.28 km or 3 km. This means that for each $l$, we can identify two branches of the solution, represented by 100 TW contours, that predict the observed heat production. The 100 TW contours are parallel to each

other and approximately straight, implying that the solutions follow a power-law form (i.e., can be expressed as $d = a\eta^b$ where $a$ and $b$ are functions of $l$). The bottom branch (or branch I) corresponds to ocean thicknesses ranging from a few hundred meters to 2.5 km and is almost independent of the choice of parameter $l$. In contrast, the position of the upper branch (or branch II) varies with $l$ and shifts to smaller ocean thicknesses as $l$ increases. The maximum ocean thickness in the models represented by the upper branch is greater than 20 km if $l = 50$ km, and 8 km if $l = 400$ km.

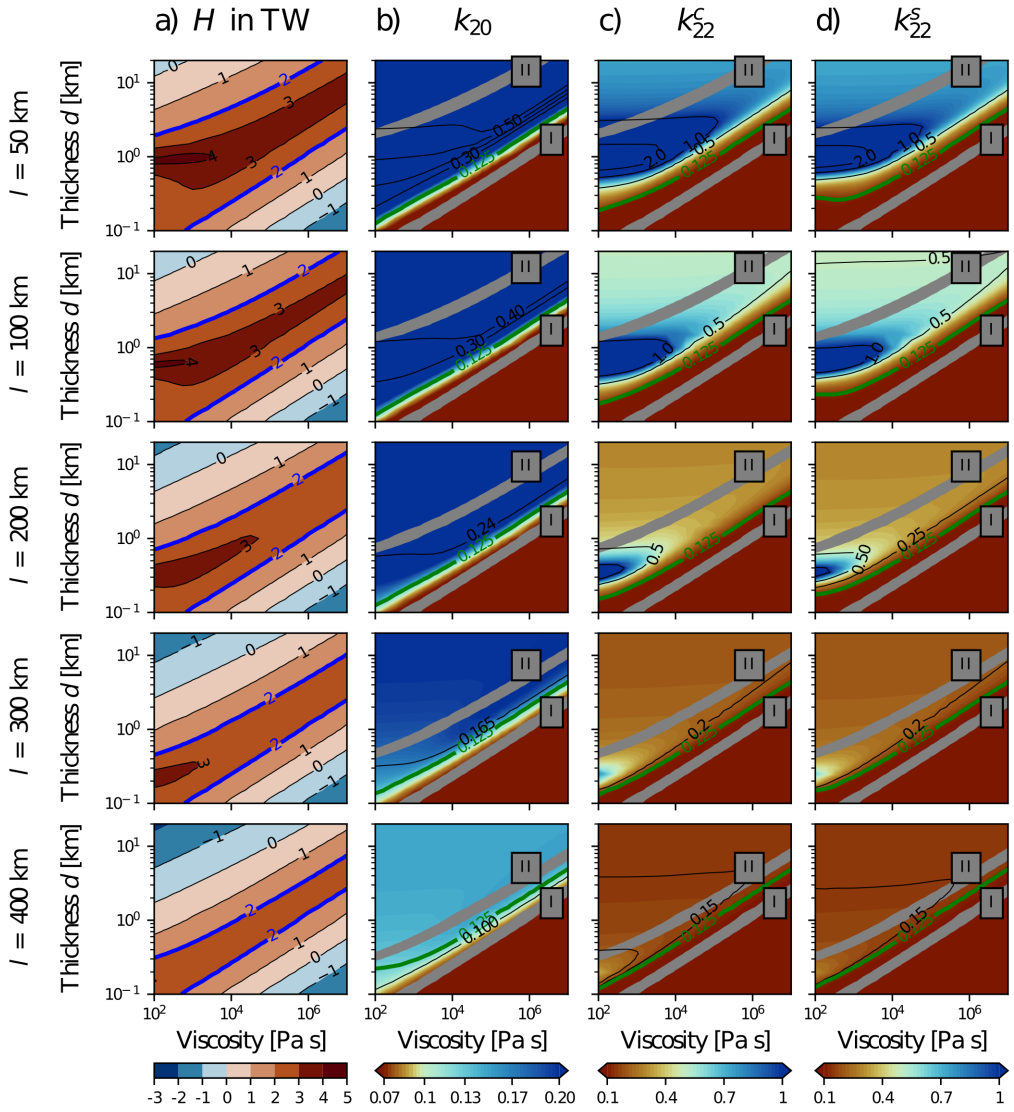



Figure 5.2: Total heat production, $H$, in the magma ocean (column a) and the tidal Love numbers (columns b–d). The heat production and the Love numbers are plotted as a function of the magma viscosity and the ocean thickness for $l = 50$, 100, 200, 300 and 400 km. The blue contours in column a correspond to the heat production of 100 TW. The shaded areas in columns b–d indicate the models with heat production between 50 and 150 TW while the green contours correspond to $k_2 = 0.125$. Labels I and II denote the models predicting $k_{20} \approx k_{22}^{c,s} < 0.1$ (branch I) and $k_{22}^{c,s} > k_{20} \gtrsim 0.1$ (branch II), respectively.

Inspection of columns b–d of Fig. 5.2 shows that the Love numbers predicted

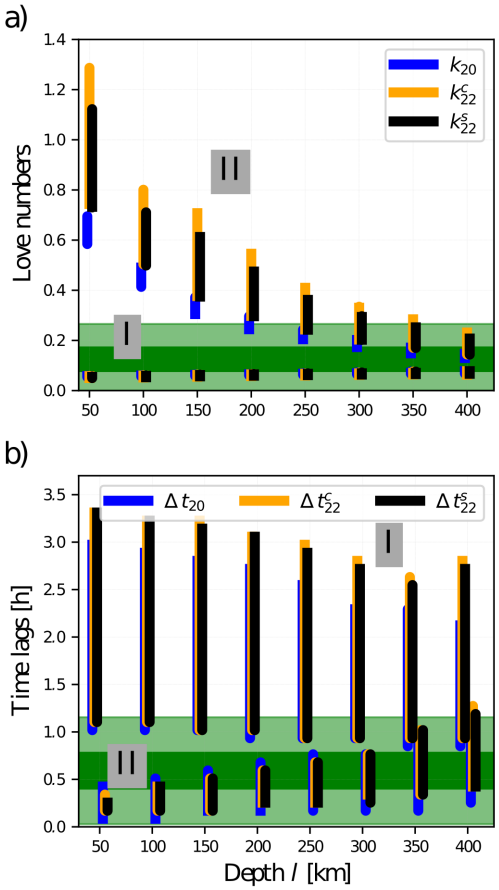



Figure 5.3: a) Tidal Love numbers and b) time lags as a function of depth $l$ for models with the heat production between 50 and 150 TW. The blue, orange, and black lines correspond to $\bullet_{20}$, $\bullet_{22}^c$, and $\bullet_{22}^s$, respectively. The shaded green boxes represent $1\sigma$ and $3\sigma$ Juno results (Park et al., 2024a).

for branch I are independent of the parameters characterizing the ocean and their values are about the same as those obtained for Io without a magma ocean (i.e., $k_{20} = k_{22}^c = k_{22}^s \lesssim 0.1$ for all $l$, $\eta$ and $d$). The Love numbers predicted for branch II vary from 0.1 to 1.3, with $k_{20}$ being usually smaller than $k_{22}^c$ and $k_{22}^s$. The Love numbers in branch II generally decrease with the increasing ocean thickness and magma viscosity, while the depth $l$ determines the range of the admissible values (Fig. 5.3a). If the magma ocean is located near the surface ($l = 50$ km), the Love numbers are either less than 0.1 (branch I) or greater than 0.55 (branch II). Depending on the viscosity and ocean thickness, $k_{20}$ can range from 0.55 to 0.7 while $k_{22}^c$ and $k_{22}^s$ can vary from 0.7 to 1.3. As $l$ is increased, the Love numbers decrease. If the ocean is located at a depth of 300 km, $k_{20}$ corresponding to branch II is about 0.2, and $k_{22}^c$ ($\approx k_{22}^s$) ranges from 0.2 to 0.3.

The time lags ($\Delta t_{20}$, $\Delta t_{22}^c$ and $\Delta t_{22}^s$, Eq. (5.3)) are shown in Figs 5.3b and 5.4. The models in the branch I (i.e., those with $k_{20} \approx k_{22}^{c,s} \lesssim 0.1$) are characterized by time lags ranging from 0.8 to 3.4 h and $\Delta t_{20} < \Delta t_{22}^{c,s}$. In contrast, the models in branch II (i.e., those with $k_{22}^{c,s} > k_{20} \geq 0.1$) predict $\Delta t_{20} \approx \Delta t_{22}^{c,s} \lesssim 1$ h.

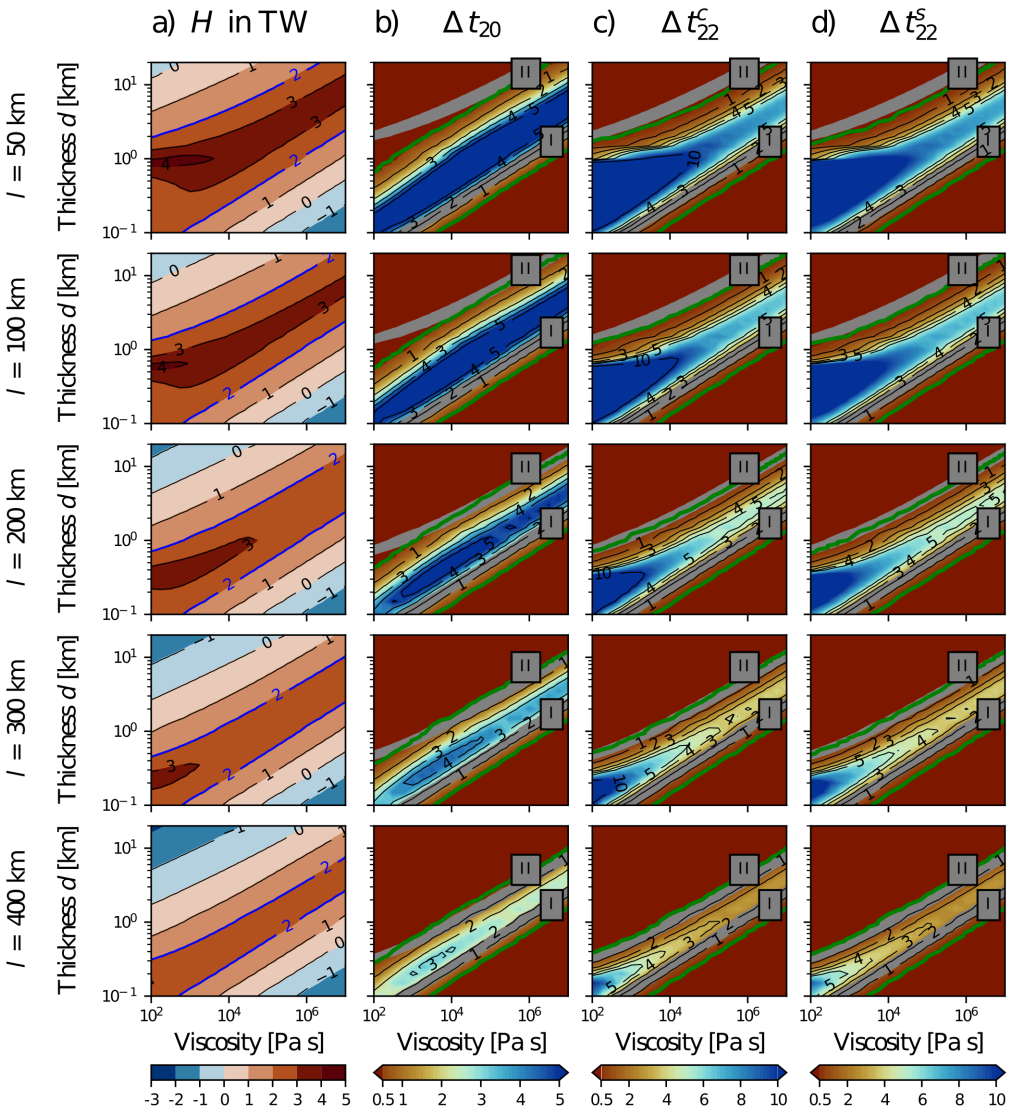



Figure 5.4: Total heat production in the magma ocean (column a) and the time lags in hours (columns b–d). The heat production and the time lags are plotted as a function of the magma viscosity and the ocean thickness for $l = 50$, 100, 200, 300 and 400 km. The blue contours in column a correspond to the heat production of 100 TW. The shaded areas in columns b–d correspond to the heat production between 50 and 150 TW while the green contours correspond to $\Delta t_2 = 2129.6$ s.

## 5.4 Conclusions

In this study, we investigated the tidal response of Io assuming that the observed heat power (∼100 TW) is generated by tidal dissipation in a liquid magma ocean. We showed that the Love number $k_2$ can be strongly affected by the Coriolis effect, resulting in different values of $k_2$ for harmonic orders 0 and 2. By systematically exploring the model space $(l, d, \eta)$ where $l$ is the depth to the ocean, $d$ is the thickness of the ocean, and $\eta$ is the viscosity of the magma, we found that for each value of depth $l$, there are two groups of models which generate the observed power. The $k_2$ Love numbers obtained for models of the first group (or branch I) are independent of the harmonic order and are similar in magnitude to those

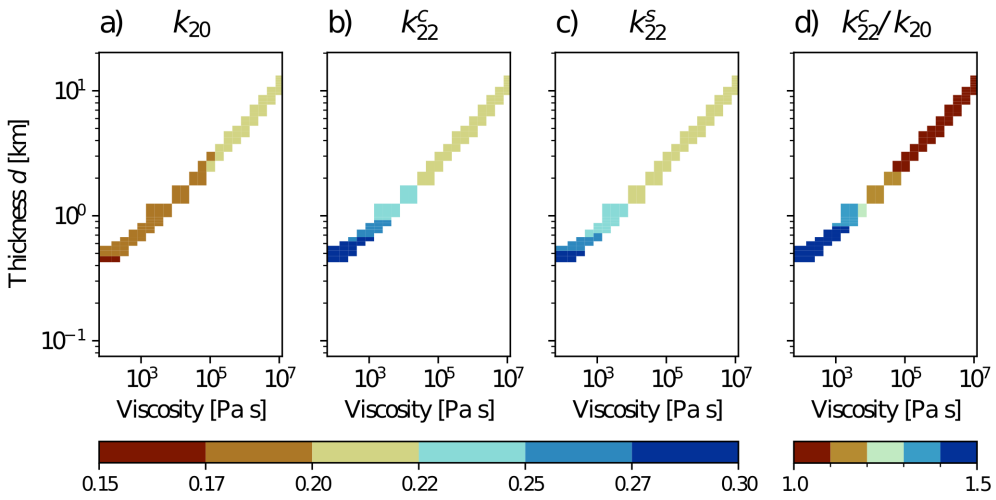



Figure 5.5: Tidal Love numbers (columns a–c) and ratio $k_{22}^c/k_{20}$ (column d) as a function of ocean thickness and viscosity for depth $l = 300$ km. The values correspond to ocean dissipation in the range of 50–150 TW and $k_{20} > 0.1$ (branch II).

predicted for solid tides ($k_{20} \approx k_{22}^{c,s} \lesssim 0.1$). However, compared to the solid tide models, the tidal response is characterized by a longer time lag (1–3.4 h) and the fact that the time lag may depend on the harmonic order ($\Delta t_{20} \neq \Delta t_{22}^c \approx \Delta t_{22}^s$).

The second group of models (branch II) predicts $k_{22}^c \approx k_{22}^s \geq k_{20} \gtrsim 0.1$ and time lags of less than about 1 h, thus comparable with the time lag expected for Io without a magma ocean. The Love numbers in this group decrease with the increasing depth to the ocean and exhibit the dependence on the harmonic order.

Our results indicate that the existence of a global shallow magma ocean in Io is unlikely. Although the models in the branch I give the values of $k_{20}$ and $k_{22}^{c,s}$ that are compatible with the observation, they predict too long ($\gtrsim 1$ h) time lags. On the other hand, the models in branch II give the correct values of the time lag but predict unrealistically high values of $k_2$ if the thickness of the solid layer above the ocean is less than 200 km. In contrast, all models in branch II below a depth of 250 km are consistent with Io's observed tidal response. A possible way to confirm or reject the deep ocean hypothesis would be to compare the $k_2$ Love numbers of order 0 and 2 and to show that $k_{22}^{c,s}/k_{20} > 1$ (Fig. 5.5). However, this would require the Love numbers $k_{20}$ and $k_{22}^{c,s}$ to be determined with high accuracy because the ratio $k_{22}^{c,s}/k_{20}$ for Io with a deep magma ocean and a heat power of 100 TW is close to 1 if the thickness of the ocean is more than 1 km (Fig. 5.5d).

Although our conclusions are in general agreement with those of Park et al. (2024a), the reader should be aware that their validity depends on the method used to interpret the Juno data. In analyzing the data, Park et al. (2024a) assumed that the tidal response of Io is described by a single Love number, i.e., $k_{20} = k_{22}^c = k_{22}^s$ and $\Delta t_{20} = \Delta t_{22}^c = \Delta t_{22}^s$, an assumption that is strictly valid only for a solid mantle. As we have demonstrated, the tidal response of Io with a magma ocean can be affected by the Coriolis force resulting in a dependence of $k_2$ on the harmonic order. This suggests that the conclusions of Park et al. (2024a) cannot be definitely confirmed until the effect of fluid tides is included in the analysis of the Juno dataset.

# 6. Compressible Love numbers of Ganymede[1]

## 6.1 Introduction

Ganymede, the largest moon in our Solar System, is likely to harbor a global subsurface ocean. One of the main goals of the Juice mission is to improve our understanding of the internal structure of Ganymede and the ongoing processes in its interior. The mission is expected to provide data that is critical for assessing Ganymede's formation, evolution, and the potential habitability of its subsurface ocean. Although the induced magnetic field (Kivelson et al., 2002) and the measurements made by the Hubble Space Telescope by monitoring the oscillations of auroral ovals confirm the existence of an electrically-conductive salty ocean inside Ganymede (Saur et al., 2015), the structure of the hydrosphere, namely the thickness of the ice Ih layer, the ocean and high-pressure ice layers, is a subject of debate (e.g., Vance et al., 2018).

The Juice mission will provide important new constraints on Ganymede's internal structure by measuring its tidal response, or more specifically, by determining the tidal potential Love number, $k_2$. The $k_2$ characterizes the gravitational potential induced by the tides (e.g., Hay et al., 2022; Kamata et al., 2016; Jara-Orué and Vermeersen, 2016), and it is sensitive to the thickness and mechanical properties of the ice shell, as well as the density structure and the dynamics of the ocean (e.g., Matsuyama et al., 2018). The Juice spacecraft will provide unique constraints on the internal structure of Ganymede, as it will allow the Love numbers to be determined with unprecedented accuracy (Cappuccio et al., 2020). In order to take full advantage of these measurements, we require numerical tools that can incorporate physical effects such as compressibility, the Coriolis force, and moon-moon tidal potential.

While the incompressible models have been widely used in determining the tidal response of a planetary body (e.g., Spada, 2008; Melini et al., 2022; Matsuyama et al., 2018; Briaud et al., 2023; Saliby et al., 2023), the compressible models are scarce (e.g., Kamata et al., 2016; Rovira-Navarro et al., 2024). The incompressible models are computationally more flexible, but they are limited in their ability to represent realistic internal structures, as the material parameters depend on pressure. In the case of Ganymede, the compressibility of its ice shell can lead to a measurable difference in Ganymede's tidal response. In a recent study, it has been shown that the tidal response of a compressible ice shell with laterally varying material parameters enhances the tidal response compared to an incompressible shell (Rovira-Navarro et al., 2025), such that the difference falls well within the expected sensitivity range of the Juice spacecraft.

While the tidal deformations and dissipation of the satellites of the outer Solar System are dominated by the eccentricity tides, they are not the only contributor to the gravitational perturbations. It has been shown that in a closely packed planetary system, such as TRAPPIST-1, the gravitational interactions due to the

[1]This chapter is supported by the Barrande fellowship programme and developed in collaboration with Gabriel Tobie and Gaël Choblet.

planets in the system might also be important (e.g., Hay and Matsuyama, 2019b). In a recent study, Hay et al. (2020) has shown that due to their orbital configuration, the Galilean satellites can also have an impact on one another. It has been shown that the gravitational perturbations due to neighboring moons can lead to additional dissipation peaks and an enhanced tidal response of Ganymede at higher frequencies (Hay et al., 2022). Here, we revisit the moon-moon tide concept, but in a time-domain framework where 3D ocean dynamics are included. We investigate the gravitational perturbations due to Io and Europa on Ganymede.

In this chapter, we use Oceanus to compute Ganymede's tidal response. Our aim is to predict the Love numbers of Ganymede that Juice is expected to measure. We first investigate the effects of compressibility and the dynamical flow in the ocean due to eccentricity tides. Following that, we include the tidal perturbations due to moon-moon interactions, namely due to Io and Europa, and study the tidal response of the ocean. Before proceeding further, we note that this chapter presents the first step in a broader investigation of Ganymede's tidal response. The results presented here are limited, but they lay a solid foundation for more comprehensive analyses.

## 6.2 Method

To compute the tidal response of Ganymede, we use Oceanus, as described in Chapter 2.

Although the internal structure of Ganymede is described in Benchmarks 2 and 3, we briefly review it here. We describe the internal structure of Ganymede with five layers: a solid ice I shell, a viscous liquid ocean, a solid high-pressure ice, a solid silicate mantle, and an inviscid liquid core. The set of internal profiles is then defined by the ice shell thickness, which varies from 40 to 150 km. For each ice shell thickness, we compute the reference density, bulk modulus, and shear modulus of the hydrosphere from the pressure-temperature conditions by using the SeaFreeze thermodynamic representation (Journaux et al., 2020). We fix the mantle and core densities to 3500 and 8000 $\mathrm{kg\,m^{-3}}$, respectively, and their radii are set to match the observed mass and MoI factor of Ganymede. The rheology of the solid parts is chosen to be Maxwell. The viscosity profile of the ice shell is determined by the temperature using the Arrhenius equation. The viscosities of the high-pressure ice and the mantle are set to $10^{15}$ and $10^{20}$ Pa s, respectively. Both the silicate mantle and the liquid core are assumed to be incompressible, and the tidal flow in the liquid core is neglected. In the simulations of the dynamics of tidal flow in the ocean, the ocean viscosity is set to $10^2$ Pa s.

The latest improvement to Oceanus is the implementation of the moon-moon tides. We follow the formalism of Hay and Matsuyama (2019b). We assume that the satellites have co-planar and circular orbits. The moon-moon tidal potential is given by (e.g., Kaula, 1964; Murray and Dermott, 2000; Hay and Matsuyama, 2019b)

$$V_t^m = \frac{1}{2}\frac{GMm}{r_{ij}^3} r^2 \Bigg[ P_{20}(\cos\vartheta) - \frac{1}{2} P_{22}(\cos\vartheta \left(\cos 2\varphi \cos 2\varphi_{ij} + \sin 2\varphi \sin 2\varphi_{ij}\right) \Bigg], \tag{6.1}$$

where $m$ is the mass of Ganymede, $M$ is the mass of the tide-raising body (either Io or Europa), $r_{ij}$ is the distance between Ganymede and the tide-raising body, $\varphi_{ij}$ is the angle between the line connecting the two moons and the unit vector in the direction of Jupiter.

The traditional way to investigate the tidal response to the moon-moon tides (Equation 6.1) is to take a Fourier transform of the tidal potential and the governing equations, and compute the tidal response for each frequency (Hay et al., 2020). However, in this study, we take a different approach by defining the Love numbers in the time domain. In contrast to the eccentricity tides, in the case of the moon-moon tides, Love numbers vary in time during a tidal cycle and are expressed as

$$\begin{aligned} V_{g,20} &= k_{20}\left(t\right)\left(V_{t,20}^{e}+V_{t,20}^{m}\right)=k_{20}\left(t\right)V_{t,20}^{T},\\ V_{g,22}^{c} &= k_{22}^{c}\left(t\right)\left(V_{t,22}^{e,c}+V_{t,22}^{m,c}\right)=k_{22}^{c}\left(t\right)V_{t,22}^{T,c},\\ V_{g,22}^{s} &= k_{22}^{s}\left(t\right)\left(V_{t,22}^{e,s}+V_{t,22}^{m,s}\right)=k_{22}^{s}\left(t\right)V_{t,22}^{T,s}, \end{aligned} \tag{6.2}$$

where $V_{t,\bullet}^{e,\bullet}$ is the eccentricity tides (Equation 2.9), and $V_{t,\bullet}^{T,\bullet}$ is the total potential defined as the sum of the tidal potentials for the eccentricity and moon-moon tides. Moreover, each Love number defined above is also separated into a time-averaged part and an oscillatory part as

$$k_{2\bullet}^{\bullet}\left(t\right)=\bar{k}_{2\bullet}^{\bullet}+\delta k_{2\bullet}^{\bullet}\left(t\right). \tag{6.3}$$

We only consider the effects due to Io and Europa, and compute the tidal response of Ganymede for two scenarios: (i) tidal response of an ocean with a thickness of $d = 5$ km, and (ii) $d = 150$ km. The internal structure of Ganymede is described above, with only the difference being that the solid layers are treated as an elastic body for the investigation of the moon-moon tides.

## 6.3 Results

In Figure 6.1, we show the compressible Love numbers of Ganymede for two cases: without and with the ocean dynamics. Our results show that the Love numbers of Ganymede are in the range from 0.42 to 0.53, depending on the ice shell thickness (Figure 6.1a). The value of $k_2$ decreases with increasing ice shell thickness. Within the ice shell thickness range of 40 to 145 km (corresponding to an ocean thickness between 300 and 20 km), the decoupling between order 0 and 2 Love numbers remains rather small, while decoupling increases for the thicker ice shell (Figure 6.1b).

Oceanus allows us to directly compare the incompressible and compressible Love numbers. For two models, we compare the Love numbers without including the ocean dynamics. Between the compressible and incompressible models, the Love numbers change between 2% to 6% (Figure 6.2). Moreover, Figure 6.2 shows that based on a given Love number, the estimated ice shell thickness can differ by 20 to 30 km between compressible and incompressible models.

In Figure 6.3, we examine the time-dependent behavior of Ganymede's tidal response over a tidal cycle. The tidal response for both thin and thick oceans

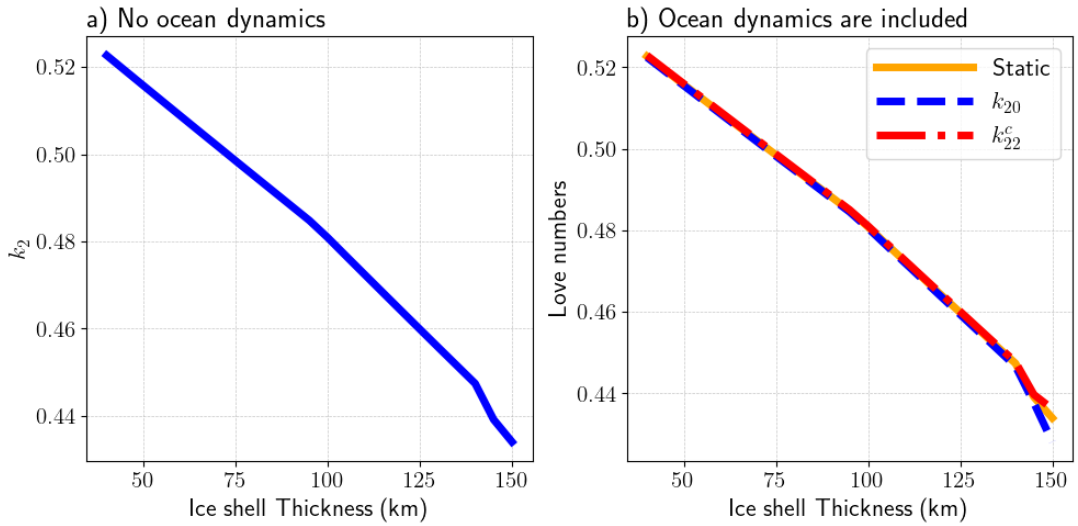



Figure 6.1: Compressible Love numbers of Ganymede for (a) a model without the ocean dynamics, and (b) a model with the ocean dynamics, where the orange line shows the Love numbers in the case without ocean dynamics.

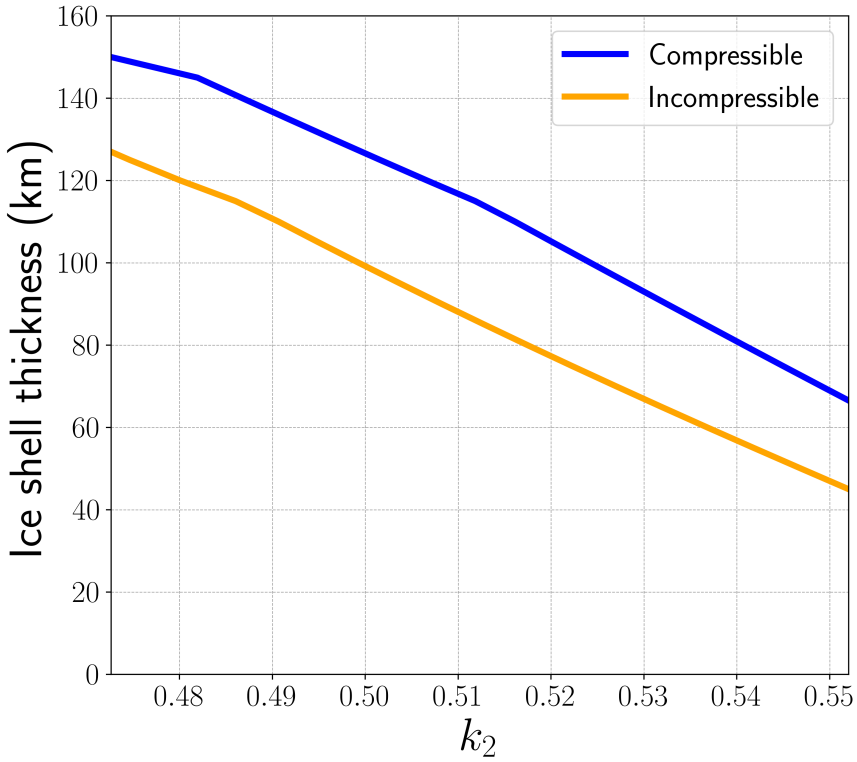



Figure 6.2: Ice shell thickness estimate based on the incompressible and compressible Love numbers without the dynamics of the ocean. Blue line is the compressible model, whereas the orange line is the incompressible model.

is similar to that from computed purely eccentricity forcing (Figure 6.3b). Figure 6.3a shows that the thicker oceans exhibit less oscillatory behavior compared

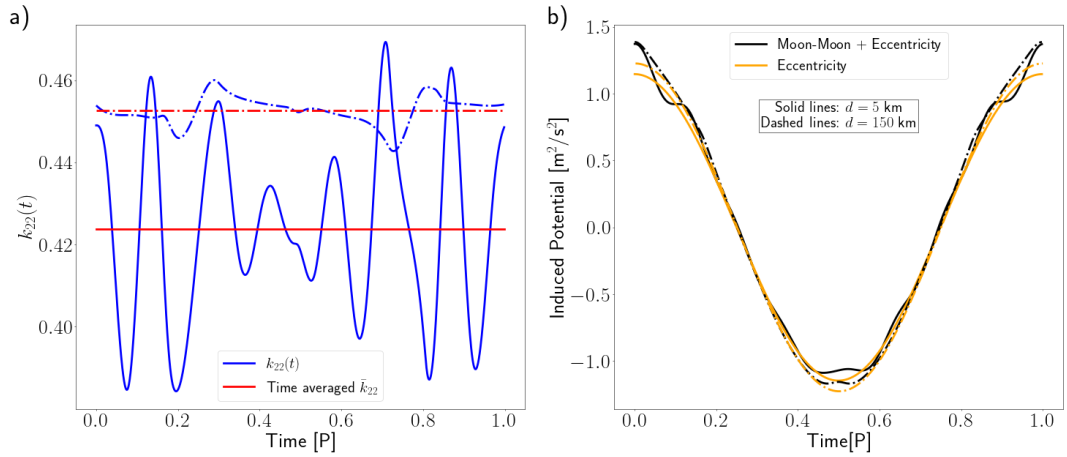



Figure 6.3: Love numbers of Ganymede in response to the moon-moon tides. a) The tidal Love number as a function of time plotted over a period for an ocean thickness of 5 km (solid lines) and 150 km (dashed-dotted lines). The red line represents the time-averaged Love number. b) Induced gravitational potential in the presence of a thin (5 km) and thick (150 km) ocean. The orange lines are the response to purely eccentricity tides, and the black lines also include the moon-moon tides.

to the thin oceans. The Love number for thick oceans can vary by 2% for thick oceans, and up to 10% for thin oceans over a tidal cycle.

## 6.4 Discussion and Conclusion

Our results show that the compressible Love numbers of Ganymede vary between 0.41 and 0.53, depending on the thickness of the outer ice shell (Figure 6.1a). This range is consistent with theoretical expectations for icy satellites and reflects the sensitivity of the tidal response to the mechanical structure of the outer layers (Jara-Orué and Vermeersen, 2016; Kamata et al., 2016). The tidal response increases as the ice shell thickness decreases.

Figure 6.1b further shows the effects of the ocean dynamics on the Love numbers. Within the ice shell thickness range of 40 to 145 km (corresponding to ocean thicknesses from approximately 300 km to 20 km), the tidal flow in the ocean plays only a minor role, resulting in small decoupling between spherical harmonic orders 0 and 2. However, for thicker ice shells (and thus shallower oceans), this decoupling becomes more pronounced. This suggests that the tidal response of Ganymede is more sensitive to ocean dynamics when the ocean is thin (similar to the results presented for Io in Chapters 4 and 5).

Our analysis of the compressible and incompressible models shows that the compressible model results in a higher value of $k_2$. More importantly, compressible models estimate thicker ice shells for a given value of $k_2$ compared to the incompressible case. Although the incompressible models have been widely used (e.g., Spada, 2008; Melini et al., 2022; Briaud et al., 2023), this result shows the im-

portance of including compressibility in tidal modeling, as neglecting it can lead to underestimation of the ice shell thickness.

The averaged tidal response to the moon-moon tides is close to the response to the eccentricity tides. Similar to the eccentricity tides, the thin ocean affects the signal more pronouncedly than the thick oceans. The time dependency of the Love numbers varies between the thick and thin ocean cases, where the thick ocean case exhibits less oscillatory behavior (up to 2% of variation from the averaged value), while the thin ocean case can differ by almost 10% from the averaged value. AS these variations can be captured by the Juice/3GM experiment, the moon-moon tides can introduce further constraints on the structure of the hydrosphere.

In this chapter, we presented the first results that analyze Ganymede's tidal response using a compressible, dynamically coupled model. Our results demonstrate that the Love number $k_2$ is highly sensitive to the thickness of the ice shell and the dynamical behavior of the subsurface ocean. By comparing compressible and incompressible models, we showed that compressibility plays a critical role in accurately constraining the ice shell thickness, with implications for interpreting future observational data. Furthermore, although the dynamics of the ocean have a subtle effect on the tidal response, the signal still can be detectable by the Juice/3GM experiment (Cappuccio et al., 2020).

Our first findings on Ganymede's tidal response highlight the importance of employing physically comprehensive models. While these results are preliminary, they lay the groundwork for several future research directions. One of the extensions involves including a salty ocean to assess the effects of composition. Additionally, we aim to extend the study of the moon-moon tides to explore whether certain combinations of ocean thickness and composition could lead to resonant tidal responses (Hay et al., 2022).

Another important aspect is the temporal evolution of Ganymede's eccentricity (Van Hoolst et al., 2024), which may have amplified tidal forcing during the lifetime of the Juice mission. These short-term variations of the eccentricity can enhance the tidal response within the subsurface ocean.

To further constrain the internal structure, we will expand our analysis to include the Love number $h_2$, which characterizes radial surface displacement. A combined interpretation of $k_2$ and $h_2$ will provide a more comprehensive understanding of Ganymede's interior, since $h_2$ is expected to be measured by the Juice/GALA experiment (Hussmann et al., 2019, 2025).

Finally, in order to capture the complexity tidal response, the tidal response in the presence of a dynamic ocean should be analyzed together with the tidal response obtained when the variations of the material parameters are considered (Rovira-Navarro et al., 2025).

# Conclusion

This thesis is devoted to enhancing our understanding of the link between the internal structure and tidal response of planetary bodies. It particularly focuses on the tidal response of outer Solar system moons with subsurface oceans (magma or water). It qualitatively and quantitatively investigates the tidal response of the body to the eccentricity tides. Tidal response of the planetary body is strongly dependent on the body's internal structure, and it can be generalized by the degree 2 Love numbers, the tidal dissipation, the phase lag, or the quality factor $Q$. Based on the tidal response models, we can gain insight into whether the reservoir can exist and understand its physical characteristics, such as its thickness, composition, and depth beneath the surface. Moreover, as a secondary effect, tidal currents in the liquid layer can contribute to the global heating, generate an induced magnetic field, and can be used when assessing the potential habitability of a water subsurface ocean, like the one in Ganymede or Enceladus.

In this work, we present a novel approach to modeling the tidal response of planetary bodies. While the solid body tide models are well established and widely used in the literature for various planetary bodies, like the Earth, Moon, Mars, and the outer Solar System moons, they lack incorporation of dynamic liquid layers (e.g., Takeuchi and Saito, 1972; Spada, 2008). It was shown that the dynamics of a liquid layer that undergoes periodic tidal forcing can generate significant dissipation (e.g., Tyler, 2008, 2014; Matsuyama, 2014; Beuthe, 2016; Matsuyama et al., 2018). These early models are based on the two-dimensional approach called the Laplace tidal equations. This approach neglects the effects of the radial (vertical) flow within the ocean and obtains the tidal flow only in the lateral directions. More recently, there were more general approaches that solved the tidal flow problem in a subsurface ocean in 3D geometry (Rovira-Navarro et al., 2019; Rekier et al., 2019). In the context of the Laplace tidal equations, these methods were more general, but they lacked the simultaneous coupling between the liquid and solid layers. Based on these recent studies, we took the problem one step further and introduced a new model where we calculate the tidal response considering the tidal deformation in the solid layers coupled with the viscous flow in the liquid layers. We introduced this coupling through the continuity of the velocity and traction at the interfaces between the layers. As its actual version, we also introduced the compressibility into our model. Our novel approach was compared with the already existing models like the one by Rekier et al. (2019), Spada (2008), and Takeuchi and Saito (1972).

Oceanus is first used to investigate the tidal flow in Enceladus' ocean and tidal dissipation in its viscoelastic core. We assume a model of Enceladus that consists of three layers: the viscoelastic core, the viscous liquid ocean, and a solid ice shell. We assume that all layers are incompressible and compute the tidal response for different core parameters. In the first part of the study, we show that the dissipation in both the core and the ocean depends on the ocean thickness and viscosity. If the ocean is thin enough ($\lesssim 1$ km), the dissipation in Enceladus is dominated by the tidal flow in the ocean. The thin ocean affects the deformation of the ice shell and core, resulting in their synchronized deformation. In contrast, the tidal flow in the thick oceans ($> 1$ km) has no effect on the deformation of the

crust and the core, and the tidal dissipation is dominated by the highly deformable core as the heating in the ocean becomes negligible. Moving from the thin oceans to the thick oceans, the location of dominant dissipation moves from the ocean to the core, while keeping the total heat production constant, around 20 GW. In the second part of the study, we focus on the tidal flow patterns in the subsurface ocean and the distribution of the tidal dissipation. We show that the patterns of the flow and the tidal heating depend on the ocean viscosity and thickness. From the investigation of the velocity components of the tidal flow, we show that the radial flow in the ocean is negligible only if the ocean is thinner than 5 km. The fact that the radial flow has a non-negligible contribution to the velocity field for relatively thick oceans ($> 5$ km) shows that one of the key assumptions of the LTE is violated. We also emphasize that the LTE and Oceanus tidal dissipation exhibit different behavior due to the underlying assumption of the boundary conditions. If the ocean thickness is less than 10 km, the tidal dissipation can differ by several orders of magnitude between the free-slip and no-slip models. Finally, based on our results, we conclude that the tidal dissipation in Enceladus' subsurface ocean is negligible.

In the second part of the thesis, we used Oceanus to investigate the tidal dissipation and Love numbers in the presence of a hypothetical magma ocean on Io. Our results are aligned with the results of Tyler et al. (2015) such that Io's observed heat output can be the result of a magma ocean. In addition, we showed that tidal heating patterns computed by Oceanus come in a much greater variety depending on the ocean viscosity and thickness. The highest heat production in a hypothetical magma ocean is observed for an ocean thickness of around 1 km and viscosity less than $10^4$ Pa s, in which the tidal dissipation can reach up to $10^4$ TW. While this amount of heating is unrealistic for present-day conditions, it opens a speculative scenario where the magma ocean has been formed by a temporary increase in Io's eccentricity (Hussmann and Spohn, 2004). The tidal heating due to high eccentricity could lead to extreme melting and form the magma ocean, which, when formed, can maintain itself. The subsequent tidal heating pattern due to a magma ocean would be concentrated at lower latitudes ($< 30°$). This particular heating pattern is consistent with the observed heat output, which was observed by the Juno mission, and it was shown that the hot spots at lower latitudes emit more heat compared to polar regions (Davies et al., 2024). Although a magma ocean is consistent with the heat output observed through hot spots, the models with dissipative asthenosphere can also explain the equatorial heating (e.g., Kervazo et al., 2021; Matsuyama et al., 2022). Hence the confirming the presence of a magma ocean is difficult by the analysis of the hot spots. A stronger constraint on the presence of the magma ocean can be obtained by the interpretation of the Love numbers. It was suggested that the value of $k_2$ should be larger than 0.5 in the presence of a magma ocean, and should be around 0.1 if Io is a fully solid body (e.g., Bierson and Nimmo, 2016; Kervazo et al., 2021). While our results confirm the previous studies by showing that in the presence of a thick ocean, the Love numbers are larger than 0.7, we also show that, even for a small Love number ($< 0.1$), there can be a thin magma ocean. The recent flybys by the Juno spacecraft have allowed us to quantify the tidal response of Io. The Love number, as the results of Juno's observations, is around 0.125 with a time lag of about 30 minutes (Park et al., 2024a). The low value of

the Love number and the time lag suggest that the presence of a thin liquid layer near the surface (at a depth around $\sim 30$ km) is unlikely. In a subsequent study, we demonstrated that a thin magma ocean is indeed absent, but we also showed that the presence of a magma ocean cannot be discarded since the observed values still can be explained if there is a liquid layer at depths greater than 200 km.

In the last part of the thesis, we investigate the tidal response of Ganymede. We focus on the effects of the compressibility, dynamics of the ocean, and the moon-moon tides. Our results show that the Love numbers can vary from 0.42 to 0.53, depending on the ice shell thickness. We demonstrate that using an incompressible model can lead to errors of up to 30 km in the estimated ice shell thickness. Similar to the results for Io, the dynamics of a thin ocean ($d < 10$ km) strongly affects the Love numbers, resulting in the Love numbers being split between orders 0 and 2. In contrast, the tidal flow in the thick oceans has weaker effects on the gravitational response. Although the tidal flow in the thick oceans may appear to be insignificant, the gravitational response due to an ocean flow is still detectable by the Juice/3GM experiment (Cappuccio et al., 2020). The flow in the thick oceans leads to a difference between orders 0 and 2 of only a few percent, whereas this difference can reach up to 5% if the ocean is thin. Since the expected accuracy of the 3GM experiment is 0.01%, it can provide constraints both for thin and thick ocean cases.

Moreover, we also investigate the tidal response of Ganymede with respect to gravitational perturbations due to Io and Europa (e.g., Hay et al., 2020). In our time-domain approach, while the time-averaged Love numbers for moon-moon tides and Love numbers just in response to eccentricity tides remain similar to each other, in the moon-moon tides case, the Love number can vary over a tidal cycle. The Love numbers can vary by up to 10% if the ocean is thin, and only by 2% if the ocean is thick. The results presented in this work for Ganymede are the first steps of what the tidal response should be like. To establish future incorporation of the results of the 3GM experiment, we require future simulations of different internal structures of Ganymede. In addition to including more complex interiors of Ganymede, we also note that in future calculations, the eccentricity changes of Ganymede should be considered, since the eccentricity can increase (or decrease) by a factor of 2 during the Juice mission's lifetime in the orbit of Ganymede (Van Hoolst et al., 2024). The short-term variations of the eccentricity can lead to strong inertial effects within the subsurface ocean and alter the gravitational response.

Finally, we note that this study omitted the two other main targets of the planetary sciences: Europa and Titan. While the eccentricity tides may have no major consequences on Europa, the tides on Titan could play a crucial role in assessing its internal structure. From the initial observations of the Cassini spacecraft, the Love number for Titan is estimated to be 0.616 (Durante et al., 2019). The large value of $k_2$ was explained by the presence of a dense subsurface ocean at a depth of 50 to 100 km (Mitri et al., 2014). It was also suggested that this value could be explained by a resonant, stably stratified ocean (Idini and Nimmo, 2024). However, a recent investigation of the data acquired by the Cassini spacecraft presented a lower value of the Love number, 0.375, which implies that potentially the ocean is deeper and less dense than originally expected (Goossens et al., 2024). In addition, the $Q$ factor of Titan was estimated to be as low as

5, indicating a large time delay and very high dissipation (Downey and Nimmo, 2025) (for comparison, Io's $Q$ factor is estimated to be 11.4 (Park et al., 2024a)). Together with the lower value of the Love number and a low value of the $Q$ factor, the Titan's case appears to be similar to Io with a magma ocean (see the branch I in Figure 5.3). By investigating the tidal response of Titan, we could potentially determine whether there can be a thin liquid layer rich in organics.

# Bibliography


J. Anderson, E. Lau, W. Sjogren, G. Schubert, and W. Moore. Gravitational constraints on the internal structure of Ganymede. *Nature*, 384(6609):541–543, 1996a. doi:10.1038/384541a0.

J. D. Anderson, W. L. Sjogren, and G. Schubert. Galileo gravity results and the internal structure of Io. *Science*, 272:709–712, 1996b. doi:10.1126/science.272.5262.709.

J. D. Anderson, R. A. Jacobson, E. L. Lau, W. B. Moore, and G. Schubert. Io's gravity field and interior structure. *Journal of Geophysical Research: Planets*, 106:32963–32969, 2001. doi:10.1029/2000JE001367.

B. Aygün and O. Čadek. Impact of the core deformation on the tidal heating and flow in Enceladus' subsurface ocean. *Journal of Geophysical Research: Planets*, 128:e2023JE007907, 2023. doi:10.1029/2023JE007907.

B. Aygün and O. Čadek. Tidal heating in a subsurface magma ocean on Io revisited. *Geophyical Research Letters*, 51:e2023GL107869, 2024. doi:10.1029/2023GL107869.

B. Aygün and O. Čadek. Love numbers for Io with a magma ocean. *Icarus*, 436: 116567, 2025. doi:10.1016/j.icarus.2025.116567.

R.-M. Baland, M. Yseboodt, and T. V. Hoolst. Obliquity of the Galilean satellites: The influence of a global internal liquid layer. *Icarus*, 220:435–448, 8 2012. doi:10.1016/j.icarus.2012.05.020.

R.-M. Baland, M. Yseboodt, and T. V. Hoolst. The obliquity of Enceladus. *Icarus*, 268:12–31, 4 2016. doi:10.1016/j.icarus.2015.11.039.

M. Běhounková, G. Tobie, O. Čadek, G. Choblet, C. Porco, and F. Nimmo. Timing of water plume eruptions on Enceladus explained by interior viscosity structure. *Nature Geoscience*, 8(8):601–604, 2015. doi:10.1038/ngeo2475.

M. Běhounková, G. Tobie, G. Choblet, and O. Čadek. Coupling mantle convection and tidal dissipation: Applications to Enceladus and Earth-like planets. *Journal of Geophysical Research: Planets*, 115, 2010. doi:10.1029/2009JE003564.

A. Berne, M. Simons, J. T. Keane, and R. S. Park. Inferring the Mean Thickness of the Outer Ice Shell of Enceladus From Diurnal Crustal Deformation. *Journal of Geophysical Research: Planets*, 128, 6 2023. doi:10.1029/2022JE007712.

M. Beuthe. Spatial patterns of tidal heating. *Icarus*, 223:308–329, 3 2013. doi:10.1016/j.icarus.2012.11.020.

M. Beuthe. Crustal control of dissipative ocean tides in Enceladus and other icy moons. *Icarus*, 280:278–299, 12 2016. doi:10.1016/j.icarus.2016.08.009.

M. Beuthe, A. Rivoldini, and A. Trinh. Enceladus's and Dione's floating ice shells supported by minimum stress isostasy. *Geophysical Research Letters*, 43, 10 2016. doi:10.1002/2016GL070650.

C. J. Bierson. The impact of rheology model choices on tidal heating studies. *Icarus*, 414:116026, 2024. ISSN 0019-1035. doi:10.1016/j.icarus.2024.116026.

C. J. Bierson and F. Nimmo. A test for Io's magma ocean: Modeling tidal dissipation with a partially molten mantle. *Journal of Geophysical Research: Planets*, 121:2211–2224, 2016. doi:10.1002/2016JE005005.

A. Blöcker, J. Saur, L. Roth, and D. F. Strobel. MHD modeling of the plasma interaction with Io's asymmetric atmosphere. *Journal of Geophysical Research: Space Physics*, 123:9286–9311, 2018. doi:10.1029/2018JA025747.

F. P. Bretherton. Low frequency oscillations trapped near the equator. *Tellus*, 16(2):181–185, 1964. doi:10.1111/j.2153-3490.1964.tb00159.x.

D. Breuer, C. W. Hamilton, and K. Khurana. The internal structure of Io. *Elements*, 18:385–390, 2022. doi:10.2138/gselements.18.6.385.

A. Briaud, A. Fienga, D. Melini, N. Rambaux, A. Mémin, G. Spada, C. Saliby, H. Hussmann, A. Stark, V. Viswanathan, and D. Baguet. Constraints on the lunar core viscosity from tidal deformation. *Icarus*, 394:115426, 2023. ISSN 0019-1035. doi:10.1016/j.icarus.2023.115426.

M. Běhounková, G. Tobie, G. Choblet, and O. Čadek. Impact of tidal heating on the onset of convection in Enceladus's ice shell. *Icarus*, 226(1):898–904, 2013. ISSN 0019-1035. doi:10.1016/j.icarus.2013.06.033.

M. Běhounková, O. Souček, J. Hron, and O. Čadek. Plume Activity and Tidal Deformation on Enceladus Influenced by Faults and Variable Ice Shell Thickness. *Astrobiology*, 17:941–954, 9 2017. doi:10.1089/ast.2016.1629.

O. Čadek, G. Tobie, T. Van Hoolst, M. Massé, G. Choblet, A. Lefèvre, G. Mitri, R. Baland, M. Běhounková, O. Bourgeois, and A. Trinh. Enceladus's internal ocean and ice shell constrained from Cassini gravity, shape, and libration data. *Geophysical Research Letters*, 43:5653–5660, 6 2016. doi:10.1002/2016GL068634.

O. Čadek, M. Běhounková, G. Tobie, and G. Choblet. Viscoelastic relaxation of Enceladus's ice shell. *Icarus*, 291:31–35, 7 2017. doi:10.1016/j.icarus.2017.03.011.

O. Čadek, O. Souček, and M. Běhounková. Is Airy Isostasy Applicable to Icy Moons? *Geophysical Research Letters*, 46:14299–14306, 12 2019a. doi:10.1029/2019GL085903.

O. Čadek, O. Souček, M. Běhounková, G. Choblet, G. Tobie, and J. Hron. Long-term stability of Enceladus' uneven ice shell. *Icarus*, 319:476–484, 2 2019b. doi:10.1016/j.icarus.2018.10.003.

O. Čadek, K. Kalousová, J. Kvorka, and C. Sotin. The density structure of Titan's outer ice shell. *Icarus*, 364:114466, 8 2021. doi:10.1016/j.icarus.2021.114466.

P. Cappuccio, A. Hickey, D. Durante, M. Di Benedetto, L. Iess, F. De Marchi, C. Plainaki, A. Milillo, and A. Mura. Ganymede's gravity, tides and rotational state from JUICE's 3GM experiment simulation. *Planetary and Space Science*, 187:104902, 2020. ISSN 0032-0633. doi:10.1016/j.pss.2020.104902.

J. C. Castillo-Rogez, M. Efroimsky, and V. Lainey. The tidal history of Iapetus: Spin dynamics in the light of a refined dissipation model. *Journal of Geophysical Research: Planets*, 116(E9), 2011. doi:https://doi.org/10.1029/2010JE003664.

E. Chen, F. Nimmo, and G. Glatzmaier. Tidal heating in icy satellite oceans. *Icarus*, 229:11–30, 2 2014. doi:10.1016/j.icarus.2013.10.024.

G. Choblet, G. Tobie, C. Sotin, M. Běhounková, O. Čadek, F. Postberg, and O. Souček. Powering prolonged hydrothermal activity inside Enceladus. *Nature Astronomy*, 1:841–847, 11 2017. doi:10.1038/s41550-017-0289-8.

J. A. Crisp. Rates of magma emplacement and volcanic output. *Journal of Volcanology and Geothermal Research*, 20:177–211, 4 1984. doi:10.1016/0377-0273(84)90039-8.

F. A. Dahlen. On the static deformation of an earth model with a fluid core. *Geophysical Journal International*, 36(2):461–485, 1974. doi:10.1111/j.1365-246X.1974.tb03649.x.

A. G. Davies, G. J. Veeder, D. L. Matson, and T. V. Johnson. Map of Io's volcanic heat flow. *Icarus*, 262:67–78, 12 2015. doi:10.1016/j.icarus.2015.08.003.

A. G. Davies, J. E. Perry, D. A. Williams, and D. M. Nelson. Io's polar volcanic thermal emission indicative of magma ocean and shallow tidal heating models. *Nature Astronomy*, 8:94–100, 2024. doi:10.1038/s41550-023-02123-5.

K. de Kleer, A. S. McEwen, and R. S. Park. Tidal heating: Lessons from Io and the Jovian system. Technical report, Keck Institute for Space Studies, Caltech, Pasadena, 2019.

B. G. Downey and F. Nimmo. Titan's spin state as a constraint on tidal dissipation. *Science Advances*, 11(6):eadl4741, 2025. doi:10.1126/sciadv.adl4741.

D. Durante, D. Hemingway, P. Racioppa, L. Iess, and D. Stevenson. Titan's gravity field and interior structure after Cassini. *Icarus*, 326:123–132, 2019. ISSN 0019-1035. doi:10.1016/j.icarus.2019.03.003.

M. Efroimsky. Tidal dissipation compared to seismic dissipation: In small bodies, Earths, and Super-Earths. *The Astrophysical Journal*, 746(2):150, feb 2012. doi:10.1088/0004-637X/746/2/150.

M. Efroimsky and V. Lainey. Physics of bodily tides in terrestrial planets and the appropriate scales of dynamical evolution. *Journal of Geophysical Research: Planets*, 112(E12), 2007. doi:10.1029/2007JE002908.

O. Golle, C. Dumoulin, G. Choblet, and O. Čadek. Topography and geoid induced by a convecting mantle beneath an elastic lithosphere. *Geophysical Journal International*, 189:55–72, 4 2012. doi:10.1111/j.1365-246X.2012.05364.x.

L. Gomez Casajus, A. I. Ermakov, M. Zannoni, J. T. Keane, D. Stevenson, D. R. Buccino, D. Durante, M. Parisi, R. S. Park, P. Tortora, and S. J. Bolton. Gravity field of Ganymede after the Juno extended mission. *Geophysical Research Letters*, 49(24):e2022GL099475, 2022. doi:10.1029/2022GL099475.

S. Goossens, B. van Noort, A. Mateo, E. Mazarico, and W. van der Wal. A low-density ocean inside Titan inferred from cassini data. *Nature Astronomy*, 8(7):846–855, 2024. doi:10.1038/s41550-024-02253-4.

O. Grasset, M. Dougherty, A. Coustenis, E. Bunce, C. Erd, D. Titov, M. Blanc, A. Coates, P. Drossart, L. Fletcher, H. Hussmann, R. Jaumann, N. Krupp, J.-P. Lebreton, O. Prieto-Ballesteros, P. Tortora, F. Tosi, and T. Van Hoolst. JUpiter ICy moons Explorer (JUICE): An ESA mission to orbit Ganymede and to characterise the Jupiter system. *Planetary and Space Science*, 78:1–21, 2013. ISSN 0032-0633. doi:10.1016/j.pss.2012.12.002.

C. W. Hamilton, C. D. Beggan, S. Still, M. Beuthe, R. M. Lopes, D. A. Williams, J. Radebaugh, and W. Wright. Spatial distribution of volcanoes on Io: Implications for tidal heating and magma ascent. *Earth and Planetary Science Letters*, 361:272–286, 1 2013. doi:10.1016/j.epsl.2012.10.032.

C. J. Hansen, D. E. Shemansky, L. W. Esposito, A. I. F. Stewart, B. R. Lewis, J. E. Colwell, A. R. Hendrix, R. A. West, J. H. Waite Jr., B. Teolis, and B. A. Magee. The composition and structure of the Enceladus plume. *Geophysical Research Letters*, 38(11), 2011. doi:10.1029/2011GL047415.

H. C. Hay and I. Matsuyama. Numerically modelling tidal dissipation with bottom drag in the oceans of Titan and Enceladus. *Icarus*, 281:342–356, 1 2017. doi:10.1016/j.icarus.2016.09.022.

H. C. Hay and I. Matsuyama. Nonlinear tidal dissipation in the subsurface oceans of Enceladus and other icy satellites. *Icarus*, 319:68–85, 2 2019a. doi:10.1016/j.icarus.2018.09.019.

H. C. Hay, I. Matsuyama, and R. T. Pappalardo. The high-frequency tidal response of ocean worlds: Application to Europa and Ganymede. *Journal of Geophysical Research: Planets*, 127:e2021JE007064, 2022. doi:10.1029/2021JE007064.

H. C. F. C. Hay and I. Matsuyama. Tides between the TRAPPIST-1 planets. *The Astrophysical Journal*, 875(1):22, apr 2019b. doi:10.3847/1538-4357/ab0c21.

H. C. F. C. Hay, A. Trinh, and I. Matsuyama. Powering the Galilean Satellites with Moon-Moon Tides. *Geophysical Research Letters*, 47, 8 2020. doi:10.1029/2020GL088317.

D. J. Hemingway and T. Mittal. Enceladus's ice shell structure as a window on internal heat production. *Icarus*, 332:111–131, 11 2019. doi:10.1016/j.icarus.2019.03.011.

T. V. Hoolst, R.-M. Baland, and A. Trinh. The diurnal libration and interior structure of Enceladus. *Icarus*, 277:311–318, 10 2016. doi:10.1016/j.icarus.2016.05.025.

T. V. Hoolst, R. M. Baland, A. Trinh, M. Yseboodt, and F. Nimmo. The librations, tides, and interior structure of Io. *Journal of Geophysical Research: Planets*, 125:e2020JE006473, 2020. doi:10.1029/2020JE006473.

S. M. Howell and R. T. Pappalardo. Can Earth-like plate tectonics occur in ocean world ice shells? *Icarus*, 322:69–79, 2019. ISSN 0019-1035. doi:10.1016/j.icarus.2019.01.011.

H. Hussmann and T. Spohn. Thermal-orbital evolution of Io and Europa. *Icarus*, 171:391–410, 10 2004. doi:10.1016/j.icarus.2004.05.020.

H. Hussmann, C. Sotin, and J. Lunine. 10.18 - Interiors and evolution of icy satellites. In G. Schubert, editor, *Treatise on Geophysics (Second Edition)*, pages 605–635. Elsevier, Oxford, second edition edition, 2015. ISBN 978-0-444-53803-1. doi:10.1016/B978-0-444-53802-4.00178-0.

H. Hussmann, K. Lingenauber, R. Kallenbach, K. Enya, N. Thomas, L. M. Lara, C. Althaus, H. Araki, T. Behnke, J. M. Castro-Marin, et al. The Ganymede laser altimeter (GALA): Key objectives, instrument design, and performance. *CEAS space journal*, 11:381–390, 2019. doi:10.1007/s12567-019-00282-8.

H. Hussmann, K. Lingenauber, A. Stark, K. Enya, N. Thomas, L. M. Lara, C. Althaus, H. Araki, T. Behnke, J. Binger, et al. The Ganymede Laser Altimeter (GALA) on the Jupiter Icy Moons Explorer (JUICE) mission. *Space Science Reviews*, 221(3):33, 2025.

B. Idini and F. Nimmo. Resonant stratification in Titan's global ocean. *The Planetary Science Journal*, 5(1):15, jan 2024. doi:10.3847/PSJ/ad11ef.

L. Iess, N. J. Rappaport, R. A. Jacobson, P. Racioppa, D. J. Stevenson, P. Tortora, J. W. Armstrong, and S. W. Asmar. Gravity field, shape, and moment of inertia of Titan. *Science*, 327(5971):1367–1369, 2010. doi:10.1126/science.1182583.

L. Iess, R. A. Jacobson, M. Ducci, D. J. Stevenson, J. I. Lunine, J. W. Armstrong, S. W. Asmar, P. Racioppa, N. J. Rappaport, and P. Tortora. The tides of Titan. *Science*, 337(6093):457–459, 2012. doi:10.1126/science.1219631.

L. Iess, D. J. Stevenson, M. Parisi, D. Hemingway, R. A. Jacobson, J. I. Lunine, F. Nimmo, J. W. Armstrong, S. W. Asmar, M. Ducci, and P. Tortora. The gravity field and interior structure of Enceladus. *Science*, 344(6179):78–80, 2014. doi:10.1126/science.1250551.

W. L. Jaeger, E. P. Turtle, L. P. Keszthelyi, J. Radebaugh, A. S. McEwen, and R. T. Pappalardo. Orogenic tectonism on Io. *Journal of Geophysical Research: Planets*, 108, 8 2003. doi:10.1029/2002JE001946.

H. Jara-Orué and B. Vermeersen. Tides on Jupiter's moon Ganymede and their relation to its internal structure. *Netherlands Journal of Geosciences - Geologie en Mijnbouw*, 95(2):191–201, 2016. doi:10.1017/njg.2015.23.

X. Jia, M. G. Kivelson, K. K. Khurana, and R. J. Walker. Improved models of Ganymede's permanent and induced magnetic fields based on Galileo and Juno data. *Journal of Geophysical Research: Planets*, 130(1):e2024JE008309, 2025. doi:10.1029/2024JE008309. e2024JE008309 2024JE008309.

B. Journaux, J. M. Brown, A. Pakhomova, I. E. Collings, S. Petitgirard, P. Espinoza, T. Boffa Ballaran, S. D. Vance, J. Ott, F. Cova, G. Garbarino, and M. Hanfland. Holistic Approach for Studying Planetary Hydrospheres: Gibbs Representation of Ices Thermodynamics, Elasticity, and the Water Phase Diagram to 2,300 MPa. *Journal of Geophysical Research: Planets*, 125(1):e2019JE006176, 2020. doi:10.1029/2019JE006176. e2019JE006176 2019JE006176.

S. Kamata, I. Matsuyama, and F. Nimmo. Tidal resonance in icy satellites with subsurface oceans. *Journal of Geophysical Research: Planets*, 120(9):1528–1542, 2015. doi:10.1002/2015JE004821.

S. Kamata, J. Kimura, K. Matsumoto, F. Nimmo, K. Kuramoto, and N. Namiki. Tidal deformation of Ganymede: Sensitivity of love numbers on the interior structure. *Journal of Geophysical Research: Planets*, 121(7):1362–1375, 2016. doi:10.1002/2016JE005071.

W. Kang, T. Mittal, S. Bire, J.-M. Campin, and J. Marshall. How does salinity shape ocean circulation and ice geometry on Enceladus and other icy satellites? *Science Advances*, 8, 7 2022. doi:10.1126/sciadv.abm4665.

J. S. Kargel and S. Pozio. The volcanic and tectonic history of Enceladus. *Icarus*, 119(2):385–404, 1996.

W. M. Kaula. Tidal dissipation by solid friction and the resulting orbital evolution. *Reviews of Geophysics*, 2:661–685, 11 1964. doi:10.1029/RG002i004p00661.

M. Kervazo, G. Tobie, G. Choblet, C. Dumoulin, and M. Běhounková. Solid tides in Io's partially molten interior: Contribution of bulk dissipation. *Astronomy & Astrophysics*, 650, 2021. doi:10.1051/0004-6361/202039433.

M. Kervazo, G. Tobie, G. Choblet, C. Dumoulin, and M. Běhounková. Inferring Io's interior from tidal monitoring. *Icarus*, 373, 2022. doi:10.1016/j.icarus.2021.114737.

L. Keszthelyi. Revisiting the Hypothesis of a Mushy Global Magma Ocean in Io. *Icarus*, 141:415–419, 10 1999. doi:10.1006/icar.1999.6179.

L. Keszthelyi, A. McEwen, C. Phillips, M. Milazzo, P. Geissler, E. Turtle, J. Radebaugh, D. Williams, D. Simonelli, H. Breneman, et al. Imaging of volcanic activity on Jupiter's moon Io by Galileo during the Galileo Europa Mission and the Galileo Millennium Mission. *Journal of Geophysical Research: Planets*, 106 (E12):33025–33052, 2001. doi:10.1029/2000JE001383.

L. Keszthelyi, W. Jaeger, M. Milazzo, J. Radebaugh, A. G. Davies, and K. L. Mitchell. New estimates for Io eruption temperatures: Implications for the interior. *Icarus*, 192:491–502, 2007. doi:10.1016/j.icarus.2007.07.008.

K. K. Khurana, M. G. Kivelson, D. J. Stevenson, G. Shubert, C. T. Russell, and R. J. W. C. Planskey. Induced magnetic fields as evidence for subsurface oceans in Europa and Callisto. *Nature*, 395:777–780, 1998. doi:10.1038/27394.

K. K. Khurana, X. Jia, M. G. Kivelson, F. Nimmo, G. Schubert, and C. T. Russell. Evidence of a global magma ocean in Io's interior. *Science*, 332: 1186–1189, 2011. doi:10.1126/science.1201425.

M. Kihoulou, G. Choblet, G. Tobie, K. Kalousová, and O. Čadek. Subduction-like process in Europa's ice shell triggered by enhanced eccentricity periods. *Science Advances*, 11(23):eadq8719, 2025. doi:10.1126/sciadv.adq8719.

M. Kivelson, K. Khurana, C. Russell, R. Walker, J. Warnecke, F. Coroniti, C. Polanskey, D. Southwood, and G. Schubert. Discovery of Ganymede's magnetic field by the Galileo spacecraft. *Nature*, 384(6609):537–541, 1996. doi:10.1038/384537a0.

M. Kivelson, K. Khurana, and M. Volwerk. The permanent and inductive magnetic moments of Ganymede. *Icarus*, 157(2):507–522, 2002. ISSN 0019-1035. doi:10.1006/icar.2002.6834.

J. Kvorka and O. Čadek. A numerical model of convective heat transfer in Titan's subsurface ocean. *Icarus*, 376:114853, 2022. doi:10.1016/j.icarus.2021.114853.

S. Labrosse, A. Morison, R. Deguen, and T. Alboussière. Rayleigh–bénard convection in a creeping solid with melting and freezing at either or both its horizontal boundaries. *Journal of Fluid Mechanics*, 846:5–36, 7 2018. doi:10.1017/jfm.2018.258.

V. Lainey, J. E. Arlot, O. Karatekin, and T. V. Hoolst. Strong tidal dissipation in Io and Jupiter from astrometric observations. *Nature*, 459:957–959, 2009. doi:10.1038/nature08108.

D. Lemasquerier, A. M. Grannan, J. Vidal, D. Cébron, B. Favier, M. L. Bars, and J. M. Aurnou. Libration-driven flows in ellipsoidal shells. *Journal of Geophysical Research: Planets*, 122:1926–1950, 9 2017. doi:10.1002/2017JE005340.

H. Love. Some problems of geodynamics. *Nature*, 89:471–472, 1912. doi:10.1038/089471a0.

J. Lunine, S. Atreya, and J. Pollack. *Present state and chemical evolution of the atmospheres of Titan, Triton, and Pluto*, pages 605–665. 1989.

L. R. M. Maas. Wave focusing and ensuing mean flow due to symmetry breaking in rotating fluids. *Journal of Fluid Mechanics*, 437:13–28, 2001. doi:10.1017/S0022112001004074.

Z. Martinec. *Principles of Continuum Mechanics: A Basic Course for Physicists*. Springer International Publishing, 2019. ISBN 9783030053901. doi:10.1007/978-3-030-05390-1.

D. L. Matson, G. A. Ransford, and T. V. Johnson. Heat flow from Io (JI). *Journal of Geophysical Research: Solid Earth*, 86(B3):1664–1672, 1981. doi:10.1029/JB086iB03p01664.

I. Matsuyama. Tidal dissipation in the oceans of icy satellites. *Icarus*, 242:11–18, 11 2014. doi:10.1016/j.icarus.2014.07.005.

I. Matsuyama, M. Beuthe, H. C. Hay, F. Nimmo, and S. Kamata. Ocean tidal heating in icy satellites with solid shells. *Icarus*, 312:208–230, 9 2018. doi:10.1016/j.icarus.2018.04.013.

I. Matsuyama, T. Steinke, and F. Nimmo. Tidal heating in Io. *Elements*, 18: 374–378, 2022. doi:10.2138/gselements.18.6.374.

T. B. McCord, G. B. Hansen, and C. A. Hibbitts. Hydrated salt minerals on Ganymede's surface: Evidence of an ocean below. *Science*, 292(5521):1523–1525, 2001. doi:10.1126/science.1059916.

A. S. McEwen, L. Keszthelyi, P. Geissler, D. P. Simonelli, M. H. Carr, T. V. Johnson, K. P. Klaasen, H. H. Breneman, T. J. Jones, J. M. Kaufman, et al. Active volcanism on Io as seen by Galileo SSI. *Icarus*, 135(1):181–219, 1998.

W. B. McKinnon. Effect of Enceladus's rapid synchronous spin on interpretation of Cassini gravity. *Geophysical Research Letters*, 42(7):2137–2143, 2015. doi:10.1002/2015GL063384.

D. Melini, C. Saliby, and G. Spada. On computing viscoelastic love numbers for general planetary models: the ALMA$^3$ code. *Geophysical Journal International*, 231(3):1502–1517, 07 2022. ISSN 0956-540X. doi:10.1093/gji/ggac263.

G. Mitri, R. Meriggiola, A. Hayes, A. Lefevre, G. Tobie, A. Genova, J. I. Lunine, and H. Zebker. Shape, topography, gravity anomalies and tidal deformation of Titan. *Icarus*, 236:169–177, 2014. ISSN 0019-1035. doi:10.1016/j.icarus.2014.03.018.

Y. Miyazaki and D. J. Stevenson. A subsurface magma ocean on io: Exploring the steady-state of partially molten planetary bodies. *Planetary Science Journal*, 11:256, 2022. doi:10.3847/PSJ/ac9cd1.

W. Moore. The Thermal State of Io. *Icarus*, 154:548–550, 12 2001. doi:10.1006/icar.2001.6739.

W. B. Moore. Tidal heating and convection in io. *Journal of Geophysical Research: Planets*, 108, 8 2003. doi:10.1029/2002JE001943.

W. B. Moore, G. Schubert, J. D. Anderson, and J. R. Spencer. *The interior of Io*, pages 89–108. Springer, 2007.

C. D. Murray and S. F. Dermott. *Solar System Dynamics*. Cambridge University Press, 2000. doi:10.1017/CBO9781139174817.

F. Nimmo, A. C. Barr, M. Běhounková, W. B. McKinnon, and R. Dotson. *The Thermal and Orbital Evolution of Enceladus: Observational Constraints and Models*, pages 79–94. University of Arizona Press, 2018. ISBN 9780816537075.

G. I. Ogilvie and D. N. C. Lin. Tidal dissipation in rotating giant planets. *The Astrophysical Journal*, 610(1):477, jul 2004. doi:10.1086/421454.

G. W. Ojakangas and D. J. Stevenson. Thermal state of an ice shell on Europa. *Icarus*, 81(2):220–241, 1989. ISSN 0019-1035. doi:10.1016/0019-1035(89)90052-3.

T. C. O'Reilly and G. F. Davies. Magma transport of heat on Io: A mechanism allowing a thick lithosphere. *Geophysical Research Letters*, 8:313–316, 1981. doi:10.1029/GL008i004p00313.

R. Pappalardo, J. Head, R. Greeley, R. Sullivan, C. Pilcher, G. Schubert, W. Moore, M. Carr, J. Moore, M. Belton, et al. Geological evidence for solid-state convection in Europa's ice shell. *Nature*, 391(6665):365–368, 1998.

R. T. Pappalardo, B. J. Buratti, H. Korth, D. A. Senske, D. L. Blaney, D. D. Blankenship, J. L. Burch, P. R. Christensen, S. Kempf, M. G. Kivelson, et al. Science overview of the Europa clipper mission. *Space Science Reviews*, 220(4): 40, 2024. doi:10.1007/s11214-024-01070-5.

R. S. Park, R. A. Jacobson, L. G. Casajus, F. Nimmo, A. I. Ermakov, J. T. Keane, W. B. McKinnon, D. J. Stevenson, R. Akiba, B. Idini, D. R. Buccino, A. Magnanini, M. Parisi, P. Tortora, M. Zannoni, A. Mura, D. Durante, L. Iess, J. E. P. Connerney, S. M. Levin, and S. J. Bolton. Io's tidal response precludes a shallow magma ocean. *Nature*, 2024a. doi:10.1038/s41586-024-08442-5.

R. S. Park, N. Mastrodemos, R. A. Jacobson, A. Berne, A. T. Vaughan, D. J. Hemingway, E. J. Leonard, J. C. Castillo-Rogez, C. S. Cockell, J. T. Keane, A. S. Konopliv, F. Nimmo, J. E. Riedel, M. Simons, and S. Vance. The global shape, gravity field, and libration of Enceladus. *Journal of Geophysical Research: Planets*, 129(1):e2023JE008054, 2024b. doi:10.1029/2023JE008054.

V. Patočka, O. Čadek, and Z. Martinec. Energy balance of glacial isostatic adjustment: importance of the rotational feedback. *Geophysical Journal International*, 212:955–975, 2 2018. doi:10.1093/gji/ggx469.

S. J. Peale, P. Cassen, and R. T. Reynolds. Melting of Io by tidal dissipation. *Science*, 203:892–894, 1979. doi:10.1126/science.203.4383.892.

F. Petricca, A. Genova, S. Goossens, L. Iess, and G. Spada. Constraining the internal structures of Venus and Mars from the gravity response to atmospheric loading. *The Planetary Science Journal*, 3(7):164, 2022. doi:10.3847/PSJ/ac7878.

M. Pettine, S. Imbeah, J. Rathbun, A. Hayes, R. M. C. Lopes, A. Mura, F. Tosi, F. Zambon, and S. Bertolino. JIRAM observations of volcanic flux on Io: Distribution and comparison to tidal heat flow models. *Geophyical Research Letters*, 51:e2023GL105782, 2024. doi:10.1029/2023GL105782.

A. R. Philpotts and J. J. Ague. *Principles of Igneous and Metamorphic Petrology*. Cambridge University Press, Cambridge, UK, 2nd edition edition, 2009.

S. B. Pope. *Turbulent flows*. Cambridge University Press, 2000. doi:10.1017/CBO9780511840531.

C. C. Porco, P. Helfenstein, P. C. Thomas, A. P. Ingersoll, J. Wisdom, R. West, G. Neukum, T. Denk, R. Wagner, T. Roatsch, S. Kieffer, E. Turtle, A. McEwen, T. V. Johnson, J. Rathbun, J. Veverka, D. Wilson, J. Perry, J. Spitale, A. Brahic, J. A. Burns, A. D. DelGenio, L. Dones, C. D. Murray, and S. Squyres. Cassini observes the active south pole of Enceladus. *Science*, 311(5766):1393–1401, 2006. doi:10.1126/science.1123013.

J. Radebaugh, L. P. Keszthelyi, A. S. McEwen, E. P. Turtle, W. Jaeger, and M. Milazzo. Paterae on Io: A new type of volcanic caldera? *Journal of Geophysical Research: Planets*, 106:33005–33020, 12 2001. doi:10.1029/2000JE001406.

M. A. Ravine, C. J. Hansen, G. C. Collins, P. M. Schenk, M. A. Caplinger, L. Lipkaman Vittling, D. J. Krysak, R. P. Zimdar, J. B. Garvin, and S. J. Bolton. Ganymede observations by JunoCam on Juno perijove 34. *Geophysical Research Letters*, 49(23):e2022GL099211, 2022. doi:10.1029/2022GL099211.

J. Rekier, A. Trinh, S. A. Triana, and V. Dehant. Internal energy dissipation in enceladus's subsurface ocean from tides and libration and the role of inertial waves. *Journal of Geophysical Research: Planets*, 124:2198–2212, 8 2019. doi:10.1029/2019JE005988.

J. P. Renaud and W. G. Henning. Increased tidal dissipation using advanced rheological models: Implications for io and tidally active exoplanets. *The Astrophysical Journal*, 857:98, 4 2018. doi:10.3847/1538-4357/aab784.

M. Rieutord, B. Georgeot, and L. Valdettaro. Inertial waves in a rotating spherical shell: attractors and asymptotic spectrum. *Journal of Fluid Mechanics*, 435: 103–144, 2001. doi:10.1017/S0022112001003718.

J. H. Roberts. The fluffy core of Enceladus. *Icarus*, 258:54–66, 9 2015. doi:10.1016/j.icarus.2015.05.033.

M. Ross and G. Schubert. Tidally forced viscous heating in a partially molten Io. *Icarus*, 64:391–400, 12 1985. doi:10.1016/0019-1035(85)90063-6.

L. Roth, J. Saur, K. D. Retherford, A. Bloecker, D. F. Strobel, and P. D. Feldman. Constraints on io's interior fromauroral spot oscillations. *Journal of Geophysical Research: Space Physics*, 122:1903–1927, 2017. doi:10.1002/2016JA023701.

M. Rovira-Navarro, M. Rieutord, T. Gerkema, L. R. Maas, W. van der Wal, and B. Vermeersen. Do tidally-generated inertial waves heat the subsurface oceans of Europa and Enceladus? *Icarus*, 321:126–140, 3 2019. doi:10.1016/j.icarus.2018.11.010.

M. Rovira-Navarro, T. Gerkema, L. R. Maas, W. van der Wal, R. van Ostayen, and B. Vermeersen. Tides in subsurface oceans with meridional varying thickness. *Icarus*, 343:113711, 6 2020. doi:10.1016/j.icarus.2020.113711.

M. Rovira-Navarro, I. Matsuyama, and H. C. F. C. Hay. Thin-shell tidal dynamics of ocean worlds. *The Planetary Science Journal*, 4:23, 2 2023. doi:10.3847/PSJ/acae9a.

M. Rovira-Navarro, I. Matsuyama, and A. Berne. A spectral method to compute the tides of laterally heterogeneous bodies. *Planetary Science Journal*, 5:129, 2024. doi:10.3847/PSJ/ad381f.

M. Rovira-Navarro, I. Matsuyama, D. Dirkx, A. Berne, D. Calliess, and S. Fayolle. Prospects of using tidal tomography to constrain Ganymede's interior. *Geophysical Research Letters*, 52(11):e2025GL114708, 2025. doi:10.1029/2025GL114708. e2025GL114708 2025GL114708.

M. Rovira-Navarro, R. F. Katz, Y. Liao, W. van der Wal, and F. Nimmo. The Tides of Enceladus' Porous Core. *Journal of Geophysical Research: Planets*, 127, 5 2022. doi:10.1029/2021JE007117.

C. Saliby, A. Fienga, A. Briaud, A. Mémin, and C. Herrera. Viscosity contrasts in the Venus mantle from tidal deformations. *Planetary and Space Science*, 231:105677, 2023. ISSN 0032-0633. doi:10.1016/j.pss.2023.105677.

J. Saur, S. Duling, L. Roth, X. Jia, D. F. Strobel, P. D. Feldman, U. R. Christensen, K. D. Retherford, M. A. McGrath, F. Musacchio, A. Wennmacher, F. M. Neubauer, S. Simon, and O. Hartkorn. The search for a subsurface ocean in Ganymede with Hubble Space Telescope observations of its auroral ovals. *Journal of Geophysical Research: Space Physics*, 120(3):1715–1737, 2015. doi:10.1002/2014JA020778.

P. Schenk, H. Hargitai, R. Wilson, A. McEwen, and P. Thomas. The mountains of Io: Global and geological perspectives from Voyager and Galileo. *Journal of Geophysical Research: Planets*, 106:33201–33222, 12 2001. doi:10.1029/2000JE001408.

G. Schubert, J. Anderson, T. Spohn, and W. B. McKinnon. Interior composition, structure and dynamics of the Galilean satellites. *Jupiter: The planet, satellites and magnetosphere*, 1:281–306, 2004.

G. Schubert, J. D. Anderson, B. J. Travis, and J. Palguta. Enceladus: Present internal structure and differentiation by early and long-term radiogenic heating. *Icarus*, 188(2):345–355, 2007. ISSN 0019-1035. doi:10.1016/j.icarus.2006.12.012.

M. Segatz, T. Spohn, M. Ross, and G. Schubert. Tidal dissipation, surface heat flow, and figure of viscoelastic models of Io. *Icarus*, 75:187–206, 8 1988. doi:10.1016/0019-1035(88)90001-2.

A. P. Showman, D. J. Stevenson, and R. Malhotra. Coupled orbital and thermal evolution of Ganymede. *Icarus*, 129(2):367–383, 1997. ISSN 0019-1035. doi:10.1006/icar.1997.5778.

B. A. Smith, E. M. Shoemaker, S. W. Kieffer, and A. F. Cook. The role of SO2 in volcanism on Io. *Nature*, 280:738–743, 8 1979. doi:10.1038/280738a0.

K. M. Soderlund. Ocean Dynamics of Outer Solar System Satellites. *Geophysical Research Letters*, 46:8700–8710, 8 2019. doi:10.1029/2018GL081880.

K. M. Soderlund, K. Kalousová, J. J. Buffo, C. R. Glein, J. C. Goodman, G. Mitri, G. W. Patterson, F. Postberg, M. Rovira-Navarro, T. Rückriemen, J. Saur, B. E. Schmidt, C. Sotin, T. Spohn, G. Tobie, T. V. Hoolst, S. D. Vance, and B. Vermeersen. Ice-Ocean Exchange Processes in the Jovian and Saturnian Satellites. *Space Science Reviews*, 216:80, 8 2020. doi:10.1007/s11214-020-00706-6.

F. Sohl, T. Spohn, D. Breuer, and K. Nagel. Implications from Galileo observations on the interior structure and chemistry of the Galilean satellites. *Icarus*, 157(1):104–119, 2002. ISSN 0019-1035. doi:10.1006/icar.2002.6828.

O. Souček, J. Hron, M. Běhounková, and O. Čadek. Effect of the tiger stripes on the deformation of Saturn's moon Enceladus. *Geophysical Research Letters*, 43:7417–7423, 7 2016. doi:10.1002/2016GL069415.

O. Souček, M. Běhounková, O. Čadek, J. Hron, G. Tobie, and G. Choblet. Tidal dissipation in Enceladus' uneven, fractured ice shell. *Icarus*, 328:218–231, 8 2019. doi:10.1016/j.icarus.2019.02.012.

G. Spada. ALMA, a Fortran program for computing the viscoelastic Love numbers of a spherically symmetric planet. *Computers & Geosciences*, 34(6):667–687, 2008. ISSN 0098-3004. doi:10.1016/j.cageo.2007.12.001.

D. C. Spencer, R. F. Katz, and I. J. Hewitt. Magmatic intrusions control Io's crustal thickness. *Journal of Geophysical Research: Planets*, 125, 2020. doi:10.1029/2020JE006443.

J. R. Spencer, J. A. Rathbun, L. D. Travis, L. K. Tamppari, L. Barnard, T. Z. Martin, and A. S. McEwen. Io's Thermal Emission from the Galileo Photopolarimeter-Radiometer. *Science*, 288:1198–1201, 5 2000. doi:10.1126/science.288.5469.1198.

J. R. Spencer, J. C. Pearl, M. Segura, F. M. Flasar, A. Mamoutkine, P. Romani, B. J. Buratti, A. R. Hendrix, L. J. Spilker, and R. M. C. Lopes. Cassini encounters Enceladus: Background and the discovery of a south polar hot spot. *Science*, 311(5766):1401–1405, 2006. doi:10.1126/science.1121661.

J. R. Spencer, F. Nimmo, A. P. Ingersoll, T. A. Hurford, E. S. Kite, A. R. Rhoden, J. Schmidt, C. J. A. Howett, and R. Dotson. *Plume Origins and Plumbing: From Ocean to Surface*, pages 163–174. University of Arizona Press, 2018. ISBN 9780816537075.

S. W. Squyres, R. T. Reynolds, P. M. Cassen, and S. J. Peale. Liquid water and active resurfacing on Europa. *Nature*, 301(5897):225–226, 1983.

T. Steinke, H. Hu, D. Höning, W. van der Wal, and B. Vermeersen. Tidally induced lateral variations of Io's interior. *Icarus*, 335:113299, 1 2020. doi:10.1016/j.icarus.2019.05.001.

E. R. Stofan, C. Elachi, J. I. Lunine, R. D. Lorenz, B. Stiles, K. Mitchell, S. Ostro, L. Soderblom, C. Wood, H. Zebker, et al. The lakes of Titan. *Nature*, 445(7123): 61–64, 2007. doi:10.1038/nature05438.

M. Sundberg and R. F. Cooper. A composite viscoelastic model for incorporating grain boundary sliding and transient diffusion creep; correlating creep and attenuation responses for materials with a fine grain size. *Philosophical Magazine*, 90(20):2817–2840, 2010. doi:10.1080/14786431003746656.

P. Tackley. Three-Dimensional Simulations of Mantle Convection in Io. *Icarus*, 149:79–93, 1 2001a. doi:10.1006/icar.2000.6536.

P. J. Tackley. Convection in io's asthenosphere: Redistribution of nonuniform tidal heating by mean flows. *Journal of Geophysical Research: Planets*, 106: 32971–32981, 12 2001b. doi:10.1029/2000JE001411.

R. Tajeddine, N. Rambaux, V. Lainey, S. Charnoz, A. Richard, A. Rivoldini, and B. Noyelles. Constraints on Mimas' interior from Cassini ISS libration measurements. *Science*, 346:322–324, 10 2014. doi:10.1126/science.1255299.

H. Takeuchi and M. Saito. Seismic surface waves. In B. A. Bolt, editor, *Seismology: Surface Waves and Earth Oscillations*, volume 11 of *Methods in Computational Physics: Advances in Research and Applications*, pages 217–295. Elsevier, 1972. doi:10.1016/B978-0-12-460811-5.50010-6.

P. Thomas, R. Tajeddine, M. Tiscareno, J. Burns, J. Joseph, T. Loredo, P. Helfenstein, and C. Porco. Enceladus's measured physical libration requires a global subsurface ocean. *Icarus*, 264:37–47, 1 2016. doi:10.1016/j.icarus.2015.08.037.

G. Tobie, A. Mocquet, and C. Sotin. Tidal dissipation within large icy satellites: Applications to Europa and Titan. *Icarus*, 177(2):534–549, 2005. doi:10.1016/j.icarus.2005.04.006.

G. Tobie, O. Čadek, and C. Sotin. Solid tidal friction above a liquid water reservoir as the origin of the south pole hotspot on Enceladus. *Icarus*, 196: 642–652, 8 2008. doi:10.1016/j.icarus.2008.03.008.

G. Tobie, P. Auclair-Desrotour, M. Běhounková, M. Kervazo, O. Souček, and K. Kalousová. Tidal deformation and dissipation processes in icy worlds. *Space Science Reviews*, 221(1):1–57, 2025. doi:10.1007/s11214-025-01136-y.

B. Travis and G. Schubert. Keeping Enceladus warm. *Icarus*, 250:32–42, 4 2015. doi:10.1016/j.icarus.2014.11.017.

R. Tyler. Comparative estimates of the heat generated by ocean tides on icy satellites in the outer Solar System. *Icarus*, 243:358–385, 11 2014. doi:10.1016/j.icarus.2014.08.037.

R. H. Tyler. Strong ocean tidal flow and heating on moons of the outer planets. *Nature*, 456:770–772, 12 2008. doi:10.1038/nature07571.

R. H. Tyler. Ocean tides heat Enceladus. *Geophysical Research Letters*, 36, 8 2009. doi:10.1029/2009GL038300.

R. H. Tyler. Heating of Enceladus due to the dissipation of ocean tides. *Icarus*, 348:113821, 9 2020. doi:10.1016/j.icarus.2020.113821.

R. H. Tyler, W. G. Henning, and C. W. Hamilton. Tidal heating in a magma ocean within Jupiter's moon Io. *Astrophysical Journal Supplement Series*, 218, 2015. doi:10.1088/0067-0049/218/2/22.

T. Van Hoolst, G. Tobie, C. Vallat, N. Altobelli, L. Bruzzone, H. Cao, D. Dirkx, A. Genova, H. Hussmann, L. Iess, et al. Geophysical characterization of the interiors of Ganymede, Callisto and Europa by ESA's JUpiter ICy moons Explorer. *Space Science Reviews*, 220(5):54, 2024. doi:10.1007/s11214-024-01085-y.

S. Vance, M. Bouffard, M. Choukroun, and C. Sotin. Ganymede's internal structure including thermodynamics of magnesium sulfate oceans in contact with ice. *Planetary and Space Science*, 96:62–70, 2014. ISSN 0032-0633. doi:10.1016/j.pss.2014.03.011.

S. D. Vance, M. P. Panning, S. Stähler, F. Cammarano, B. G. Bills, G. Tobie, S. Kamata, S. Kedar, C. Sotin, W. T. Pike, R. Lorenz, H.-H. Huang, J. M. Jackson, and B. Banerdt. Geophysical investigations of habitability in ice-covered ocean worlds. *Journal of Geophysical Research: Planets*, 123(1):180–205, 2018. doi:10.1002/2017JE005341.

D. A. Varshalovich, A. N. Moskalev, and V. K. Khersonskii. *Quantum theory of angular momentum*. World Scientific, 1988.

G. J. Veeder, D. L. Matson, T. V. Johnson, D. L. Blaney, and J. D. Goguen. Io's heat flow from infrared radiometry: 1983–1993. *Journal of Geophysical Research: Planets*, 99:17095–17162, 8 1994. doi:10.1029/94JE00637.

G. J. Veeder, A. G. Davies, D. L. Matson, T. V. Johnson, D. A. Williams, and J. Radebaugh. Io: Volcanic thermal sources and global heat flow. *Icarus*, 219: 701–722, 6 2012. doi:10.1016/j.icarus.2012.04.004.

M. Walterová and M. Běhounková. Tidal effects in differentiated viscoelastic bodies: a numerical approach. *Celestial Mechanics and Dynamical Astronomy*, 129(1-2):235–256, 2017. doi:10.1007/s10569-017-9772-x.

M. Walterová and M. Běhounková. Thermal and orbital evolution of low-mass exoplanets. *The Astrophysical Journal*, 900(1):24, aug 2020. doi:10.3847/1538-4357/aba8a5.

O. L. White, P. M. Schenk, F. Nimmo, and T. Hoogenboom. A new stereo topographic map of Io: Implications for geology from global to local scales. *Journal of Geophysical Research: Planets*, 119:1276–1301, 2014. doi:10.1002/2013JE004591.

D. A. Williams, L. P. Keszthelyi, D. A. Crown, J. A. Yff, W. L. Jaeger, P. M. Schenk, P. E. Geissler, and T. L. Becker. Geologic map of Io: U.S. Geological Survey Scientific Investigations Map 3168, scale 1:15,000,000. Available at https://pubs.usgs.gov/sim/3168/, 2011.

A. Wilson and R. R. Kerswell. Can libration maintain Enceladus's ocean? *Earth and Planetary Science Letters*, 500:41–46, 10 2018. doi:10.1016/j.epsl.2018.08.012.

F. Zambon, A. Mura, R. M. C. Lopes, J. Rathbun, F. Tosi, R. Sordini, R. Noschese, M. Ciarniello, A. Cicchetti, A. Adriani, L. Agostini, G. Filacchione, D. Grassi, G. Piccioni, C. Plainaki, G. Sindoni, D. Turrini, S. Brooks, C. Hansen-Koharcheck, and S. Bolton. Io Hot Spot Distribution Detected by Juno/JIRAM. *Geophysical Research Letters*, 50, 1 2023. doi:10.1029/2022GL100597.

M. Zannoni, D. Hemingway, L. G. Casajus, and P. Tortora. The gravity field and interior structure of Dione. *Icarus*, 345:113713, 7 2020. doi:10.1016/j.icarus.2020.113713.

# List of publications

1. B. Aygün and O. Čadek. Impact of the core deformation on the tidal heating and flow in Enceladus' subsurface ocean. *Journal of Geophysical Research: Planets*, 128:e2023JE007907, 2023. doi:10.1029/2023JE007907.

2. B. Aygün and O. Čadek. Tidal heating in a subsurface magma ocean on Io revisited. *Geophysical Research Letters*, 51:e2023GL107869, 2024. doi:10.1029/2023GL107869.

3. B. Aygün and O. Čadek. Love numbers for Io with a magma ocean. *Icarus*, 436: 116567, 2025. doi:10.1016/j.icarus.2025.116567.

# A. Appendix

In this appendix, we summarize the various spherical harmonics formulae that are used in the implementation of Oceanus (Varshalovich et al., 1988; Golle et al., 2012).

## A.1 Spherical harmonics

We use the fully normalized spherical harmonics that are defined as

$$Y_{jm}(\vartheta,\varphi) = N_{jm} P_{jm}(\cos\vartheta)\, e^{im\varphi}, \tag{A.1}$$

and expand the unknown variables ($\rho$, $\boldsymbol{v}$, and $\boldsymbol{\sigma}$) in terms of these harmonics

$$\rho(t,r,\vartheta,\varphi) = \sum_{j=0}^{\infty}\sum_{m=-j}^{j} \rho_{jm}(t,r)\, Y_{jm}(\vartheta,\varphi), \tag{A.2}$$

$$\boldsymbol{v}(t,r,\vartheta,\varphi) = \sum_{j=0}^{\infty}\sum_{m=-j}^{j}\sum_{l=|j-1|}^{j+1} v^{l}_{jm}(t,r)\, \boldsymbol{Y}^{l}_{jm}(\vartheta,\varphi), \tag{A.3}$$

$$\boldsymbol{\sigma}(t,r,\vartheta,\varphi) = \sum_{j=0}^{\infty}\sum_{m=-j}^{j}\sum_{l=|j-2|}^{j+2} \sigma^{l0}_{jm}(t,r)\, \boldsymbol{Y}^{l0}_{jm}(\vartheta,\varphi) + \sigma^{l2}_{jm}\boldsymbol{Y}^{l2}_{jm}(\vartheta,\varphi). \tag{A.4}$$

## A.2 Mathematical operations in the spectral domain

Here, we present the various mathematical operations in the spectral domain, such as the divergence ($\nabla\cdot\bullet$) of the velocity and stress tensor, the gradient ($\nabla\bullet$) of the velocity, the scalar product with a radial unit vector ($\boldsymbol{e}_r\cdot\bullet$), and the vector product with a rotation vector ($\boldsymbol{e}_z\times\boldsymbol{v}$).

$$\begin{aligned}[\nabla\cdot\boldsymbol{v}]_{jm} =& \sqrt{\frac{j}{2j+1}}\left(\frac{\mathrm{d}v^{j-1}_{jm}}{\mathrm{d}r} - \frac{j-1}{r}v^{j-1}_{jm}\right)\\ &-\sqrt{\frac{j+1}{2j+1}}\left(\frac{\mathrm{d}v^{j+1}_{jm}}{\mathrm{d}r} + \frac{j+2}{r}v^{j+1}_{jm}\right)\end{aligned} \tag{A.5}$$

$$[\nabla\cdot\boldsymbol{\sigma}]^{j-1}_{jm} = \sqrt{\frac{j-1}{2j-1}}\left(\frac{\mathrm{d}\sigma^{j-2,2}_{jm}}{\mathrm{d}r} - \frac{j-2}{r}\sigma^{j-2,2}_{jm}\right) \tag{A.6}$$

$$-\sqrt{\frac{(j+1)(2j+3)}{6(2j-1)(2j+1)}}\left(\frac{\mathrm{d}\sigma^{j,2}_{jm}}{\mathrm{d}r} + \frac{j+1}{r}\sigma^{j,2}_{jm}\right) \tag{A.7}$$

$$[\nabla \cdot \boldsymbol{\sigma}]^{j}_{jm} = \sqrt{\frac{j-1}{2(2j+1)}} \left( \frac{\mathrm{d}\sigma^{j-1,2}_{jm}}{\mathrm{d}r} - \frac{j-1}{r}\sigma^{j-1,2}_{jm} \right) \tag{A.8}$$

$$-\sqrt{\frac{j+2}{2(2j+1)}} \left( \frac{\mathrm{d}\sigma^{j+1,2}_{jm}}{\mathrm{d}r} + \frac{j+2}{r}\sigma^{j+1,2}_{jm} \right) \tag{A.9}$$

$$\begin{aligned}[\nabla \cdot \boldsymbol{\sigma}]^{j+1}_{jm} = & \sqrt{\frac{j(2j-1)}{6(2j+3)(2j+1)}} \left( \frac{\mathrm{d}\sigma^{j,2}_{jm}}{\mathrm{d}r} - \frac{j}{r}\sigma^{j,2}_{jm} \right) \\ & -\sqrt{\frac{j+2}{2j+3}} \left( \frac{\mathrm{d}\sigma^{j+2,2}_{jm}}{\mathrm{d}r} + \frac{j+3}{r}\sigma^{j+2,2}_{jm} \right)\end{aligned} \tag{A.10}$$

$$[\nabla \boldsymbol{v}]^{j-2,2}_{jm} = \sqrt{\frac{j-1}{2j-1}} \left( \frac{\mathrm{d}v^{j-1}_{jm}}{\mathrm{d}r} + \frac{j}{r}v^{j-1}_{jm} \right) \tag{A.11}$$

$$[\nabla \boldsymbol{v}]^{j-1,2}_{jm} = \sqrt{\frac{j-1}{2(2j+1)}} \left( \frac{\mathrm{d}v^{j}_{jm}}{\mathrm{d}r} + \frac{j+1}{r}v^{j}_{jm} \right) \tag{A.12}$$

$$\begin{aligned}[\nabla \boldsymbol{v}]^{j,2}_{jm} = & -\sqrt{\frac{(j+1)(2j+3)}{6(2j-1)(2j+1)}} \left( \frac{\mathrm{d}v^{j-1}_{jm}}{\mathrm{d}r} - \frac{j-1}{r}v^{j-1}_{jm} \right) + \\ & \sqrt{\frac{j(2j-1)}{6(2j+1)(2j+3)}} \left( \frac{\mathrm{d}v^{j+1}_{jm}}{\mathrm{d}r} + \frac{j+2}{r}v^{j+1}_{jm} \right)\end{aligned} \tag{A.13}$$

$$[\nabla \boldsymbol{v}]^{j+1,2}_{jm} = \sqrt{\frac{j+2}{2(2j+1)}} \left( \frac{\mathrm{d}v^{j}_{jm}}{\mathrm{d}r} - \frac{j}{r}v^{j}_{jm} \right) \tag{A.14}$$

$$[\nabla \boldsymbol{v}]^{j+2,2}_{jm} = \sqrt{\frac{j+2}{2j+3}} \left( \frac{\mathrm{d}v^{j+1}_{jm}}{\mathrm{d}r} - \frac{j+1}{r}v^{j+1}_{jm} \right) \tag{A.15}$$

$$[\rho \cdot \boldsymbol{e}_r]^{j-1}_{jm} = \sqrt{\frac{j}{2j+1}}\rho_{jm} \tag{A.16}$$

$$[\rho \cdot \boldsymbol{e}_r]^{j+1}_{jm} = -\sqrt{\frac{j+1}{2j+1}}\rho_{jm} \tag{A.17}$$

$$[\boldsymbol{v} \cdot \boldsymbol{e}_r]_{jm} = \sqrt{\frac{j}{2j+1}}v^{j-1}_{jm} - \sqrt{\frac{j+1}{2j+1}}v^{j+1}_{jm} \tag{A.18}$$

$$[\boldsymbol{e}_z \times \boldsymbol{v}]^{j-1}_{jm} = \frac{i}{j}\sqrt{\frac{(j-1)(j^2-m^2)}{2j-1}}v^{j-1}_{j-1,m} - \frac{im}{j}v^{j-1}_{jm} \tag{A.19}$$

$$\begin{aligned}[\boldsymbol{e}_z \times \boldsymbol{v}]^{j}_{jm} = & \frac{i}{j}\sqrt{\frac{(j+1)(j^2-m^2)}{2j+1}}v^{j}_{j-1,m} - \frac{im}{j(j+1)}v^{j}_{jm} + \\ & \frac{i}{j+1}\sqrt{\frac{j((j+1)^2-m^2}{2j+1}}v^{j}_{j+1,m}\end{aligned} \tag{A.20}$$

$$[\boldsymbol{e}_z \times \boldsymbol{v}]_{jm}^{j+1} = \frac{im}{j+1} v_{jm}^{j+1} + \frac{i}{j+1}\sqrt{\frac{(j+2)((j+1)^2-m^2)}{2j+3}} v_{j+1,m}^{j+1} \tag{A.21}$$

## A.3 Governing equations in the spectral domain

Finally, we give the governing equations in the spectral domain for spheroidal and toroidal parts. The spheroidal parts consist of one equation of balance of mass as

$$\frac{\partial \rho_{jm}}{\partial t} + \frac{\partial \rho_0}{\partial r}\left(\sqrt{\frac{j}{2j+1}} v_{jm}^{j-1} - \sqrt{\frac{j+1}{2j+1}} v_{jm}^{j+1}\right) + \rho_0 \left[\nabla \cdot \boldsymbol{v}\right]_{jm} = 0, \tag{A.22}$$

two equations for the balance of momentum as

$$\begin{aligned} \rho_0 \frac{\partial v_{jm}^{j-1}}{\partial t} = \left[\nabla \cdot \boldsymbol{\sigma}\right]_{jm}^{j-1} &+ \rho_0 \left[\nabla V_t\right]_{jm}^{j-1} + \rho_0 \left[\nabla V_g\right]_{jm}^{j-1} \\ &+ \left[\rho \cdot \boldsymbol{e}_r\right]_{jm}^{j-1} g_0 - 2\rho_0 \omega \left[\boldsymbol{e}_z \times \boldsymbol{v}\right]_{jm}^{j-1}, \end{aligned} \tag{A.23}$$

$$\begin{aligned} \rho_0 \frac{\partial v_{jm}^{j+1}}{\partial t} = \left[\nabla \cdot \boldsymbol{\sigma}\right]_{jm}^{j+1} &+ \rho_0 \left[\nabla V_t\right]_{jm}^{j+1} + \rho_0 \left[\nabla V_g\right]_{jm}^{j+1} \\ &+ \left[\rho \cdot \boldsymbol{e}_r\right]_{jm}^{j+1} g_0 - 2\rho_0 \omega \left[\boldsymbol{e}_z \times \boldsymbol{v}\right]_{jm}^{j+1}, \end{aligned} \tag{A.24}$$

three equations for the deviatoric part of the constitutive relation

$$\frac{1}{2\eta}\sigma_{jm}^{j-2,2} + \frac{1}{2\mu}\frac{\partial \sigma_{jm}^{j-2,2}}{\partial t} - \left[\nabla \boldsymbol{v}\right]_{jm}^{j-2,2} = 0, \tag{A.25}$$

$$\frac{1}{2\eta}\sigma_{jm}^{j,2} + \frac{1}{2\mu}\frac{\partial \sigma_{jm}^{j,2}}{\partial t} - \left[\nabla \boldsymbol{v}\right]_{jm}^{j,2} = 0, \tag{A.26}$$

$$\frac{1}{2\eta}\sigma_{jm}^{j+2,2} + \frac{1}{2\mu}\frac{\partial \sigma_{jm}^{j+2,2}}{\partial t} - \left[\nabla \boldsymbol{v}\right]_{jm}^{j+2,2} = 0. \tag{A.27}$$

The isotropic part of the constitutive equation for the viscous liquid layer

$$p_{jm} = \frac{K}{\rho_0}\rho_{jm}, \tag{A.28}$$

and for the solid layers

$$\frac{1}{K}\left(\frac{\partial p_{jm}}{\partial t} - \left[v_r\right]_{jm}\rho_0 g_0\right) = -\left[\nabla \cdot \boldsymbol{v}\right]_{jm}. \tag{A.29}$$

The toroidal parts consist of one equation for the balance of momentum

$$\rho_0 \frac{\partial v_{jm}^{j}}{\partial t} = \left[\nabla \cdot \boldsymbol{\sigma}\right]_{jm}^{j} - 2\rho_0 \omega \left[\boldsymbol{e}_z \times \boldsymbol{v}\right]_{jm}^{j}, \tag{A.30}$$

and two equations for the deviatoric part of the constitutive relation

$$\frac{1}{2\eta}\sigma_{jm}^{j-1,2} + \frac{1}{2\mu}\frac{\partial \sigma_{jm}^{j-1,2}}{\partial t} - \left[\nabla \boldsymbol{v}\right]_{jm}^{j-1,2} = 0, \tag{A.31}$$

$$\frac{1}{2\eta}\sigma_{jm}^{j+1,2} + \frac{1}{2\mu}\frac{\partial \sigma_{jm}^{j+1,2}}{\partial t} - \left[\nabla \boldsymbol{v}\right]_{jm}^{j+1,2} = 0. \tag{A.32}$$

# B. Appendix

## B.1 Supporting information for Chapter 3

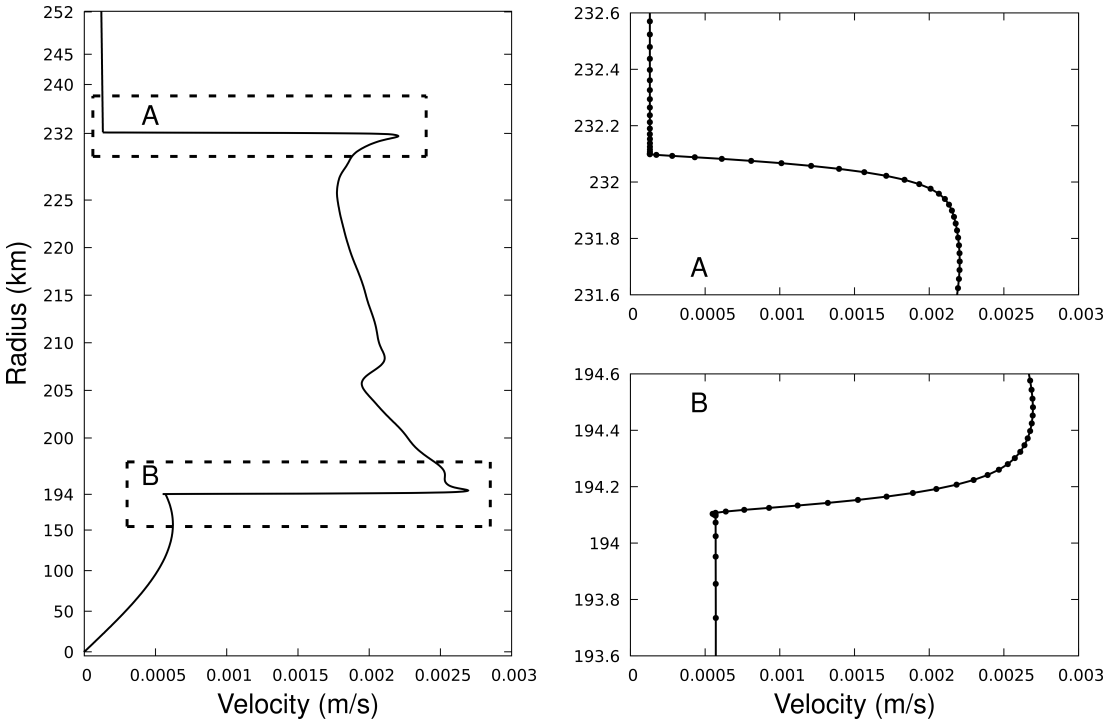



Figure B.1: Radial discretization used for the simulation with $D = 32$ km and $\eta_o = 100$ Pa s. The left panel shows the mean velocity at time $t = 0$ as a function of radius. Panels A and B on the right illustrate the radial discretization in the boundary layers.

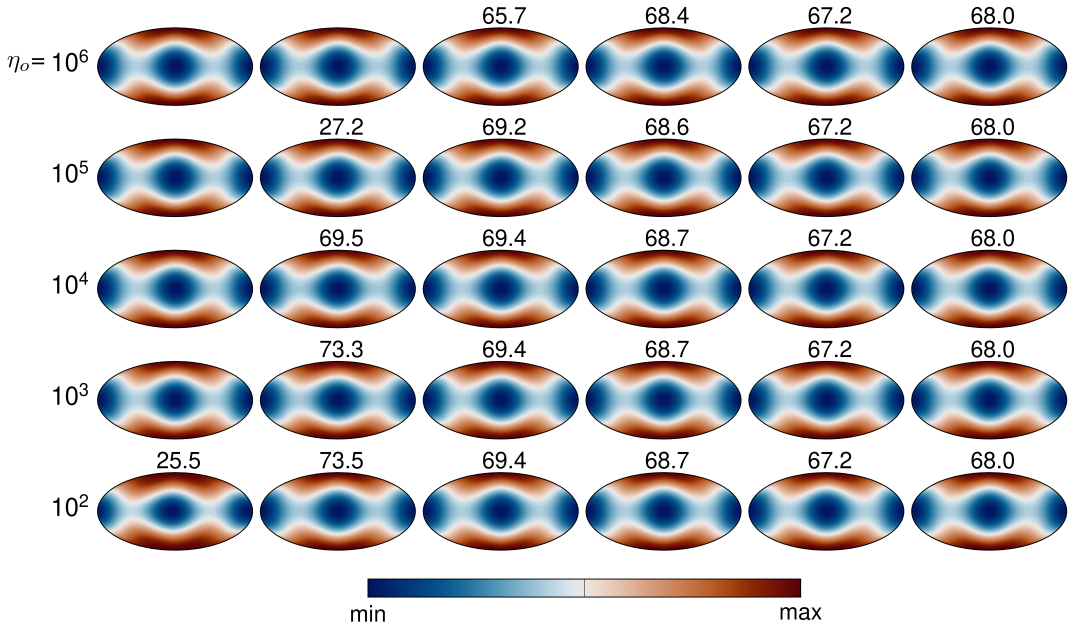



Figure B.2: As in Figure 3.3 in the Chapter 3, but for the core.

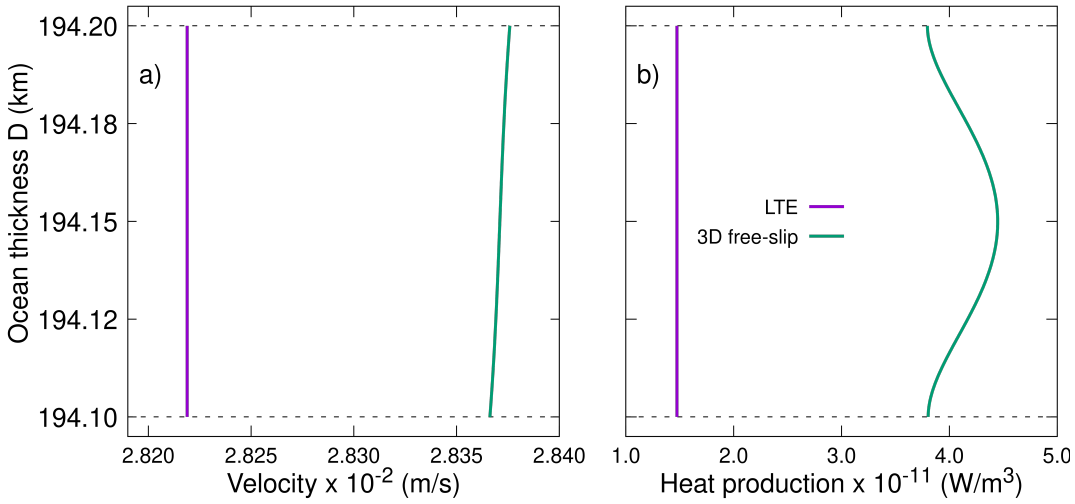



Figure B.3: Radial profile of the mean flow velocity (a) and the heat production in the ocean (b) for $D$ =100 m, $\eta_o = 100$ Pa s and $t = 0$. Note that, unlike the 3D solution (plotted in green), the modified LTE solution (violet) does not change with radius.

## B.2 Supporting information of Chapter 4

| Symbol | Parameter | Value |
|---|---|---|
| $\omega$ | Angular velocity | $4.1\ 10^{-5}\ \mathrm{s}^{-1}$ |
| $e$ | Eccentricity | 0.0041 |
| $R_s$ | Radius of Io | 1821.6 km |
| $R_m$ | Outer radius of magma ocean | 1791.6 km |
| $R_c$ | Radius of core | 927 km |
| $d$ | Thickness of magma ocean | $0.1 - 10$ km |
| $\rho$ | Density | |
| | $r > R_m$ | $3000\ \mathrm{kg\,m}^{-3}$ |
| | $r \in \langle R_c, R_m \rangle$ | $3295\ \mathrm{kg\,m}^{-3}$ |
| | $r < R_c$ | $5167\ \mathrm{kg\,m}^{-3}$ |
| $\mu$ | Shear modulus | |
| | $r > R_m$ | 65 GPa |
| | $r \in (R_c, R_m - d)$ | 60 GPa |
| $\eta$ | Viscosity | |
| | $r > R_m$ | $10^{23}$ Pa s |
| | $r \in \langle R_m - d, R_m \rangle$ | $10^2 - 10^7$ Pa s |
| | $r \in (R_c, R_m - d)$ | $10^{20}$ Pa s |

Table B.1: Parameters of the model presented in Chapter 4.

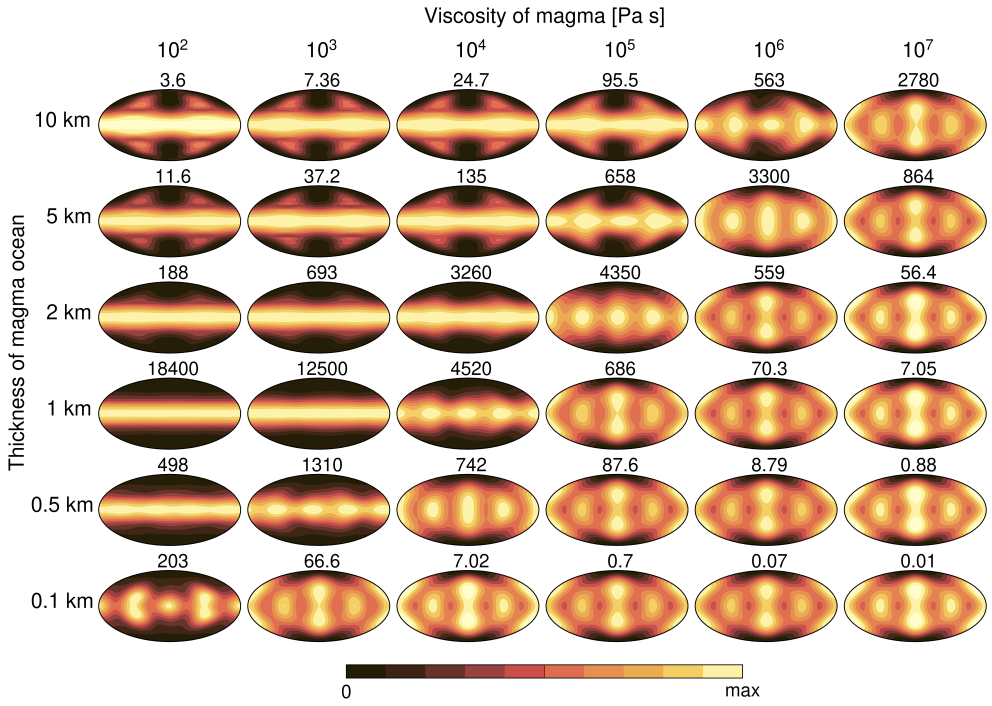



Figure B.4: As in Figure B.4 in the main text but with a 100-km thick low viscosity "magmatic sponge" layer beneath the ocean. Comparison with Figure 4.1 shows that the presence of a weak layer underlying the magma ocean affects the dissipation in the ocean in a minor way. The layer is treated as an incompressible Maxwell viscoelastic solid with $\rho = 3295$ kg/m$^3$, $\mu = 60$ GPa and $\eta = 10^{16}$ Pa s. The distribution of tidal dissipation in this layer is shown in Figure B.5.

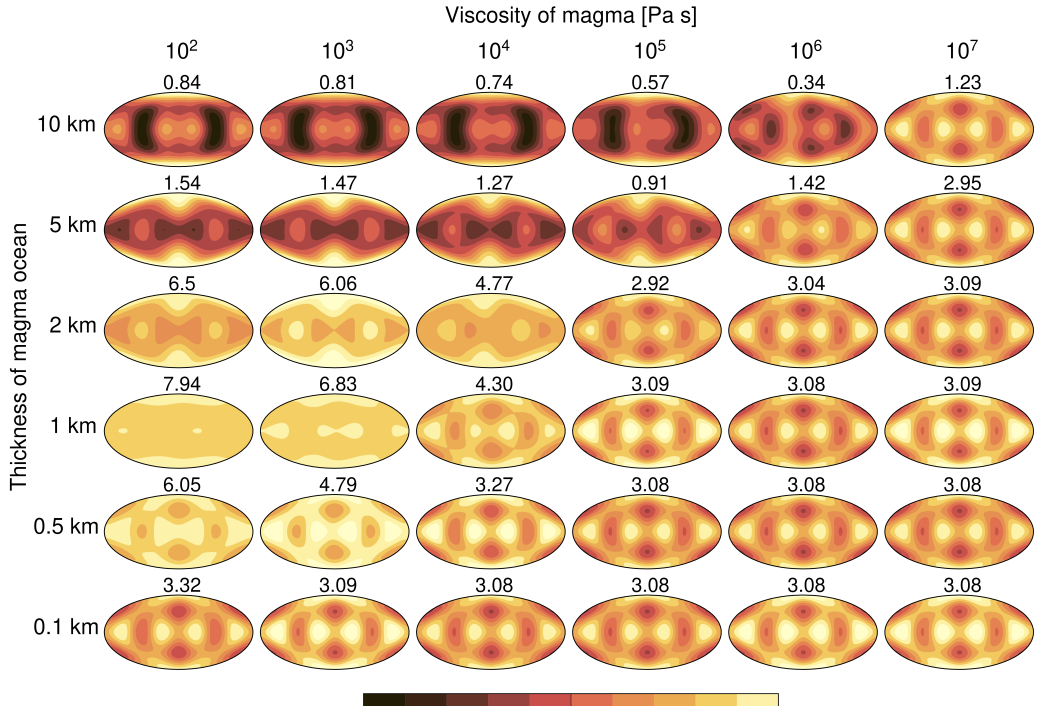



Figure B.5: Distribution of tidal dissipation in the low viscosity sub-ocean layer described in the caption to Figure B.4. The numbers above each map represent the total heat production in the layer. Note that the heating pattern and the total dissipation strongly depend on the thickness and viscosity of the magma ocean.